

**Semiconductor Quantum-Well  
Extended Cavity Lasers And  
Deep-Surface Gratings For  
Distributed Bragg Reflector Lasers**

**Submitted for the degree of  
Doctor of Philosophy  
to the  
Faculty of Engineering,  
University of Glasgow**

**by  
Hoshin Hocking Yee  
November 1995**

**© Hoshin H Yee 1995**

ProQuest Number: 13832099

All rights reserved

INFORMATION TO ALL USERS

The quality of this reproduction is dependent upon the quality of the copy submitted.

In the unlikely event that the author did not send a complete manuscript and there are missing pages, these will be noted. Also, if material had to be removed, a note will indicate the deletion.



ProQuest 13832099

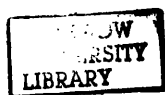
Published by ProQuest LLC (2019). Copyright of the Dissertation is held by the Author.

All rights reserved.

This work is protected against unauthorized copying under Title 17, United States Code  
Microform Edition © ProQuest LLC.

ProQuest LLC.  
789 East Eisenhower Parkway  
P.O. Box 1346  
Ann Arbor, MI 48106 – 1346

Heris  
10392  
Coy 1



## Acknowledgement

First of all, I would like to thank the former and current Heads of Department, Professors Laybourn and Beaumont for providing the departmental facilities without which the work of this thesis could not have been performed.

From the start to the end of my research in Glasgow University, my supervisor-Professor Richard De La Rue, has given me much invaluable encouragement, inspiration and many suggestions on my research. Special thanks again for his persistent help in narrowing cultural gap for me and my family.

I have been fortunate to have support from many members of the academic and technical staff. Thanks to Dr.Steve Ayling for his many constructive suggestions in regular group meetings and technical advice on device fabrication. I am also grateful that B.S.Ooi and Y.P.Song have given me many good ideas on dry etching and Brigitte Vögele has provided good-quality MBE wafers for the QW intermixing and the device fabrication.

Many thanks for help from technical staff, such as Jimmy Young for electron-gun deposition and AR coatings, Douglas McIntyre, Lois Hobbs and their teams in the clean rooms and the Ultrasmall Structure Laboratory, and the dry etching team led by Simon Hicks. I would like to express my gratitude for the extensive support of Joan Carson and Gillian Hopkins.

On the waveguide simulation and calculation for the laser devices in this work, I have to thank Michael Taylor for his design program, F-wave, and for helpful discussions with my friend, W.F.Tsai.

I would like to thank the National Science Council of Taiwan, R.O.C and National Taipei Institute of Technology. Without their financial support, this work would not have been possible.

There is one person I would like to thank the most for her patience, consideration, and encouragement from my wife, Jenny. I would like to dedicate this thesis to my wife and my children, Tiffany and Joe.

## **Publications**

- 1.H.H.Yee, S.G.Ayling, R.M.De La Rue and B.Vögele, 'Characterisation Of Improved Performance Double-Quantum-Well Composite Cavity Lasers Fabricated Using Impurity Free Vacancy Disorderng ', *Semiconductor Integrated Optoelectronics* (SIOE) Conference, Cardiff, Wales, 1995
- 2.H.H.Yee, S.G.Ayling, R.M.De La Rue and B.Vögele, 'Propagation Losses And Wavelength Shifts In Double-Quantum-Well Extended Cavity Lasers Fabricated By Dielectric Cap Disorderng', The Symposium of The Chinese Institute of Engineers in UK, Churchill College, Cambridge, 1995
- 3.H.H.Yee, S.G.Ayling, R.M.De La Rue, B.Vögele, and Y.P.Song, 'Fabrication Of High Performance Extended Cavity Double-Quantum-Well Lasers With Integrated Passive Sections ', accepted for publication in the special issue on *Optoelectronics*, IEE, Part J, 1996.

## Abstract

This thesis is concerned with two different kinds of optoelectronic component. The first of these is an extended-cavity laser diode, with results for both oxide-stripe and ridge waveguide structures. The impurity free vacancy diffusion (IFVD) technique was used to reduce the propagation losses of the passive waveguide section. A low-damage and high-selectivity dry etching technique, magnetically-confined-plasma reactive ion etching (MCP RIE), was used particularly for the ridge waveguide etch. The second focus is on deep surface gratings, fabricated by the two-beam interference technique, for distributed Bragg reflector laser diodes.

The impact of native oxide on the quantum well intermixing was investigated in detail and a model was adopted to interpret the native oxide effects on the impurity-free vacancy diffusion. It was found that a 24-nm blue shift in the disordered region was obtained for the samples annealed at 940 °C for 30 seconds with HCl precleaning, but only a 10.5 nm blue shift if precleaning was not used.

The propagation loss of the passive waveguide section for the disordered extended-cavity ridge waveguide laser was reduced to  $2.4 \pm 0.6 \text{ cm}^{-1}$ , compared to  $13 \pm 0.6 \text{ cm}^{-1}$  for the nondisordered sample, at lasing wavelengths. The lasing wavelength shift of the above lasers, arising from gain-loss competition in the composite structure, was 3 nm for the disordered sample with a 1-mm long passive waveguide section, compared to 7 nm for the nondisordered laser with the same geometry size. On the other hand, the propagation losses in the passive waveguide section of an oxide-stripe composite laser could be reduced by the IFVD process as well, but the lasing wavelength shift for this laser, due to gain-loss competition in the composite structure, is strongly current-sensitive.

Third-order deep surface gratings for the DBR laser have been successfully fabricated directly on a ridge waveguide of 4.5  $\mu\text{m}$  wide and 0.6  $\mu\text{m}$  high. At room temperature (25°C), for the DBR laser with an estimated coupling strength of 1.3, the lasing wavelength is 839.7 nm, compared to 840.6 nm for the normal Fabry-Perot ridge waveguide laser fabricated by the same material and process. A slope efficiency of 0.12 mW/mA at the active end and a threshold current of 45 mA were measured. Additionally, the temperature tuning coefficient is 0.07 nm/°C for the DBR mode and 0.48 nm/°C for the Fabry-Perot mode.

An effective way of estimating the coupling coefficient for the DBR laser has been undertaken. The factors affecting the Bragg reflectivity and the active-passive power coupling are also discussed.

# CONTENTS

ACKNOWLEDGEMENTS

PUBLICATIONS

ABSTRACT

<b>Chapter 1 Introduction.....</b>	<b>1</b>
<b>1-1 Background.....</b>	<b>1</b>
<b>1-2 Impurity free vacancy diffusion.....</b>	<b>2</b>
<b>1-3 Mode selection.....</b>	<b>2</b>
<b>1-4 Outlines of the thesis.....</b>	<b>2</b>
<b>1-5 References.....</b>	<b>3</b>
<b>Chapter 2 Essential properties of a laser diode</b>	
<b>2-1 Introduction.....</b>	<b>5</b>
<b>2-2 Electrical properties.....</b>	<b>5</b>
<b>2-2-1 Current spreading and diffusion.....</b>	<b>5</b>
<b>2-2-2 Transparency and threshold conditions.....</b>	<b>7</b>
<b>2-2-3 Energy band diagrams.....</b>	<b>13</b>
<b>2-2-4 Excitons.....</b>	<b>15</b>
<b>2-3 Optical properties.....</b>	<b>16</b>
<b>2-3-1 Variations of the refractive index of a QW laser diode.....</b>	<b>16</b>
<b>2-3-2 Gain-guiding and index-guiding regimes.....</b>	<b>17</b>
<b>2-3-3 The effective refractive index of a waveguide structure.....</b>	<b>18</b>
<b>2-3-4 Confinement factors of a MQW structure.....</b>	<b>21</b>
<b>2-3-5 Single-mode operations.....</b>	<b>23</b>
<b>2-4 Summary.....</b>	<b>24</b>
<b>2-5 References.....</b>	<b>25</b>
<b>Chapter 3 Theories of extended-cavity and distributed</b>	

## **Bragg reflector laser diodes**

<b>3-1 Introduction.....</b>	<b>26</b>
<b>3-2 Extended cavity laser diodes.....</b>	<b>26</b>
<b>3-2-1 Propagation losses.....</b>	<b>26</b>
<b>3-2-2 Lasing wavelength shifts.....</b>	<b>29</b>
<b>3-3 Distributed Bragg reflector laser diodes.....</b>	<b>30</b>
<b>3-3-1 Introduction.....</b>	<b>30</b>
<b>3-3-2 Comparison between DFB and DBR lasers.....</b>	<b>31</b>
<b>3-3-3 Key parameters of a DBR laser.....</b>	<b>31</b>
<b>3-4 Design considerations of a DBR laser.....</b>	<b>36</b>
<b>3-5 Tunability.....</b>	<b>36</b>
<b>3-6 Summary.....</b>	<b>37</b>
<b>3-7 Appendix.....</b>	<b>39</b>
<b>3-8 References.....</b>	<b>40</b>

## **Chapter 4 Impurity free vacancy diffusion**

<b>4-1 Introduction.....</b>	<b>43</b>
<b>4-2 Disorder mechanism of IFVD.....</b>	<b>43</b>
<b>4-3 Rapid thermal annealing.....</b>	<b>48</b>
<b>4-4 Photoluminescence measurement.....</b>	<b>48</b>
<b>4-5 Photocurrent response measurement.....</b>	<b>51</b>
<b>4-6 Native oxide effects.....</b>	<b>53</b>
<b>4-7 Oxide-on-GaAs systems.....</b>	<b>53</b>
<b>4-8 Summary.....</b>	<b>57</b>
<b>4-9 References.....</b>	<b>57</b>

## **Chapter 5 Extended cavity laser diodes:**

<b>5-1 Introduction.....</b>	<b>60</b>
<b>5-2 Material structure.....</b>	<b>60</b>

<b>5-3 Waveguide structure.....</b>	<b>61</b>
<b>5-4 Magnetically confined plasma RIE.....</b>	<b>64</b>
<b>5-5 Fabrication of extended cavity lasers .....</b>	<b>66</b>
<b>5-6 Experimental results.....</b>	<b>72</b>
<b>5-6-1 Measurements.....</b>	<b>72</b>
<b>5-6-2 Experimental results.....</b>	<b>75</b>
<b>5-7 Discussion.....</b>	<b>81</b>
<b>5-7-1 On extended-cavity ridge waveguide lasers.....</b>	<b>81</b>
<b>5-7-2 On extended-cavity oxide stripe lasers.....</b>	<b>85</b>
<b>5-8 Summary.....</b>	<b>85</b>
<b>5-9 References.....</b>	<b>86</b>

## **Chapter 6 Deep-surface gratings for distributed Bragg reflector lasers**

<b>6-1 Introduction.....</b>	<b>88</b>
<b>6-2 The two-beam interference technique.....</b>	<b>88</b>
<b>6-3 Grating fabrication.....</b>	<b>90</b>
<b>6-4 Grating period measurement.....</b>	<b>93</b>
<b>6-5 Modal analysis of the waveguide structure.....</b>	<b>94</b>
<b>6-6 Fabrication of the DBR lasers.....</b>	<b>96</b>
<b>6-7 Measurements and fabrication results.....</b>	<b>99</b>
<b>6-8 Discussion.....</b>	<b>106</b>
<b>6-9 Summary.....</b>	<b>107</b>
<b>6-10 References.....</b>	<b>108</b>

## **Chapter 7 Conclusions and future work**

<b>7-1 Summary of the thesis.....</b>	<b>110</b>
<b>7-2 Conclusions.....</b>	<b>110</b>
<b>7-3 Future work.....</b>	<b>112</b>

## **Appendix**

# Chapter 1 Introduction

## 1-1 Background

In recent years, optoelectronic integrated circuits (OEICs) have been developed considerably. The availability of good quality single mode waveguides has allowed electrooptic (EO), acoustooptic (AO) and thermooptic (TO) effects to be exploited successfully. Since high-performance laser diodes, semiconductor waveguides, modulators, couplers and photodetectors can be integrated monolithically on a single substrate, OEICs therefore have potential advantages [1], such as: (a) more stable alignment, (b) lower operating voltage, (c) faster operation, (d) larger optical power density, (e) greater compactness and lighter weight, and most importantly, (f) lower cost. OEICs have become increasingly promising and competitive.

## 1-2 Impurity free vacancy diffusion (IFVD)

Although monolithic-type OEICs are good for many applications, effective implementation is still difficult at present. Low-loss waveguide devices and linewidth-narrowed lasers are vitally important for many applications. Since most components in OEICs are sized on the order of a centimeter, 3 dB/cm should be good enough for most cases[2]. For the extended-cavity laser with 2-mm passive waveguide section, a propagation loss of 10 dB/cm implies that the passive waveguide would introduce total propagation loss of merely 2 dB, so 10 dB/cm would be acceptable loose limit for many applications in OEICs. By using IFVD technique, the waveguide loss in the passive section was reduced to  $2.4 \text{ cm}^{-1}$  (10.3 dB/cm), this could sufficiently meet the above criterion.

In order to have low waveguide losses, quantum well (QW) disordering techniques have been well developed during the last decade [3]. Through this bandgap engineering, quantum wells and barriers can be disordered by appropriate techniques, increasing the bandgap in the waveguide section and greatly reducing the propagation losses. In the present work, impurity-free vacancy disordering (IFVD) [4] was used to achieve this goal.

Quantum well intermixing through selective dielectric capping layers, e.g. strontium fluoride and silicon dioxide has been used in the IFVD processing. By applying this technique, GaAs/AlGaAs lasers can be QW intermixed by a rapid thermal annealer (RTA) at elevated temperature, the gallium atoms out-diffuse into the silica capping layer and subsequently may escape from its surface. The process results in a substantial number of vacancies at Ga occupied sites, the introduction of the aluminum atoms to occupy these vacant sites and an increase in the bandgap of the waveguide

section. However, the laser active region under a strontium fluoride capping layer only experiences a negligible amount of atomic Ga out-diffusion, thus providing very good suppression of the bandgap shift in this section. It has been found [5] that a large blue shift can be achieved through promoting and suppressing gallium out-diffusion under the silicon dioxide and strontium fluoride layers respectively.

### **1-3 Mode selection and surface gratings**

For a conventional Fabry-Perot (F-P) laser, although the mode nearest the gain peak is generally most intense and only a few percent of the output power is carried by other longitudinal modes which will be reasonably suppressed under CW operation, the power shared by these longitudinal modes is still significant when a laser is pulse-modulated at high bit rates. On the other hand, due to the chromatic dispersion of a fibre, the unwanted longitudinal modes limit the signal transmission rate by reducing fibre band width.

By using good-quality epitaxial material together with a proper device geometry, a laser having single transverse mode operation can be made without difficulty. However, a conventional Fabry-Perot semiconductor laser usually has a gain spectrum which is much wider than the longitudinal mode spacing and the resulting intrinsic mode discrimination is poor. Reflection gratings in DFB or DBR lasers can provide longitudinal-mode selectivity by making the feedback frequency-dependent, so that the cavity loss is significantly different for different longitudinal modes.

The use of gratings etched into a confining layer affords periodic perturbation of the effective refractive index, providing feedback by means of backward Bragg scattering. According to the Bragg condition, coherent coupling between forward and backward propagating waves occurs only at wavelengths where the grating period is an integer of half a wavelength. By choosing the grating period properly, the grating can provide significant distributed feedback only at selected wavelengths, if the grating length is sufficiently large.

It was already known [6,7,8] that electron-beam (e-beam), X-ray and holographic (also called two-beam interference) lithographies could be used to define gratings for DFB and DBR lasers. Direct-write electron-beam lithography is suitable for making gratings, but has the disadvantage of low through-put [6]. X-ray lithography is potentially a high volume grating production technique and could ultimately become the best solution for printing high-resolution mask patterns.

Because of its ready adjustability and immediate availability in the department, holographic lithography was used in this work. Generally, the formation of buried gratings for Bragg reflection interrupts the epitaxial growth of the layer structure, thereby requiring an overgrowth stage. Such overgrowth certainly increases process

complexity. To simplify grating integration in an OEIC, surface gratings fabricated after a simple growth process for DBR lasers could become a preferred solution to the above problem [7,8]. However, the surface gratings would experience high scattering loss, so the estimate coupling coefficient for third-order gratings, with a height of 0.7  $\mu\text{m}$ , in this work is about  $45 \text{ cm}^{-1}$ , compared to  $83 \text{ cm}^{-1}$  for the shallow buried gratings with a height of 0.15  $\mu\text{m}$  [9].

#### 1-4 Outlines of this thesis

This thesis is concerned with quantum well intermixing in GaAs-AlGaAs multiple-quantum-well (MQW) lasers using the IFVD technique. Particular effort has been put into the investigation of two types of devices, extended-cavity lasers and deep surface gratings for distributed-Bragg-reflector (DBR) lasers.

Chapter 2 provides a background review on the electrical and optical properties of MQW structures. Theoretical work is presented relatively informally as the basis for interpreting and discussing device characterisation in chapter 3. The IFVD quantum-well disordering technique is introduced in chapter 4. These techniques are then applied to fabricate two different types of composite cavity laser. Fabrication and characterisation of the extended-cavity lasers are depicted in chapter 5, focussing on propagation losses and lasing wavelength shifts for both oxide-stripe and ridge waveguide lasers. The fabrication of deep-surface gratings is first described in chapter 6, followed by their application to DBR lasers. Fabrication and computed results for the DBR lasers are demonstrated and followed by discussion of this device. Chapter 7 presents conclusions and discusses possibilities for future work on this subject.

#### 1-5 References

- [1] H. Nishihara, M. Haruna and T. Suhara, '*Optical Integrated Circuits*' chapter 1, McGraw-Hill, New York, 1989.
- [2] R.G.Hunsperger, '*Integrated Optics: Theory and Technology*', 3rd edition, p.75, section 5-2-1, Springer-Verlag, London, 1991.
- [3] R.M.De La Rue and J.H.Marsh, 'Integration technologies for III-V semiconductor optoelectronics based on quantum well waveguides', in *Integrated Optics and Optoelectronics*, Wong K.K. and Razeghi M, Eds. Los Angeles, CA, SPIE (Int.Soc.Opt. Eng.) 1993.
- [4] D.G.Deppe, N. Holonyak, Jr., W.E.Plano, V.M.Robbins, J.M. Dallesasse, K.C.Hsieh, and J.E.Baker, 'Impurity diffusion and layer interdiffusion in  $\text{Al}_x\text{Ga}_{1-x}\text{As}$ -GaAs heterostructures', 64 (4), pp.1838-1844, J.Appl. Phys. 1988.

- [5] J.Beauvais, J.H. Marsh, A.H. Kean, A.C.Bryce and C. Button, 'Suppression of bandgap shifts in GaAs/AlGaAs quantum wells using strontium fluoride caps', V.28, No.17, pp.1671-1672, Electron. Lett., 1992.
- [6] M.Nakao, K.Sato, T.Nishida, T.Tamamura, A.Ozawa, Y.Saito, I.Okada, H.Yoshihara, '1.55  $\mu\text{m}$  DFB laser array with  $\lambda/4$  shifted first-order gratings fabricated by X-ray lithography ', V.25, No.2, pp.148-149, Electron. Lett.,1989
- [7] L.M.Miller, J.T.Verdeyen, J.J.Coleman, R.P.Bryan, J.J.Alwan, K.J.Beernink, J.S.Hughes, and T.M.Cockerill,' A distributed feedback ridge waveguide quantum well heterostructure laser ', V.3, No.1, pp.6-8, Photon. Tech. Lett., 1991
- [8] D.Hofstetter, H.P.Zappe, J.E.Epler and J.Sochtig, 'Single-growth-step GaAs/AlGaAs distributed Bragg reflector lasers with holographically-defined recessed gratings', V.30, No.22, pp.1858-1859, Electron. Lett., 1994
- [9] S.Noda, K. Kojima, K. Mitsunagw, K.Kyuma, K.Hamanaka, and T. Nakayama, 'Ridge waveguide AlGaAs-GaAs distributed feedback lasers', p.188-193, V.23, No.2, IEEE J. Quantum Electron., 1987.

## Chapter 2 Essential properties of a laser diode

### 2-1 Introduction

This chapter is intended to provide a background for, and a basic understanding of, the double heterostructure (DH) laser, particularly for quantum well laser diodes. This fundamental approach is beneficial for an understanding of the optical and the electrical properties of QW laser diodes. Each section has a focus, which will be frequently referred to in subsequent chapters.

### 2-2 Electrical properties

#### 2-2-1 Current spreading and diffusion

To characterize laser performance, current spreading and diffusion have to be taken into account, especially when the stripe width is small and the conductivity of confining layers is high. In general, the thickness of the active layer is much smaller than the stripe width and carrier diffusion lengths, so this problem can be analyzed approximately as a 1-D one. However, if there is high radiative recombination in the centre of the pumping region or little axial diffusion of inverted carriers in a cavity[1], [2], the carrier distribution, resulting from the spatial hole-burning effect, in the longitudinal direction can be very important as well.

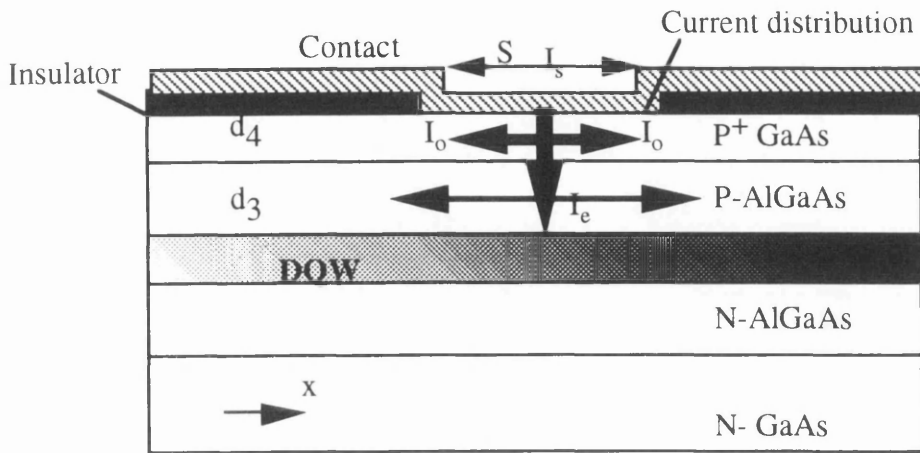
Fig.2-1(a) is a cross-sectional view of an oxide stripe laser. The region uncovered by the contact stripe can be divided into many distributed resistive differential elements and the equipotentials in the thin layer on the P-side, i.e.  $V_1, V_2 \dots V_4$ , are taken to be perpendicular to the PN junction, therefore the spreading and diffusion current may be treated approximately as a 1-D lateral current flow. By using the model proposed by Tsang et al [3], the approximate current density  $J_e$  under the contact stripe can be written as follows:

$$J_s = J_e + [ 8J_e / \beta R_x S^2 ]^{1/2} \quad (2-1)$$

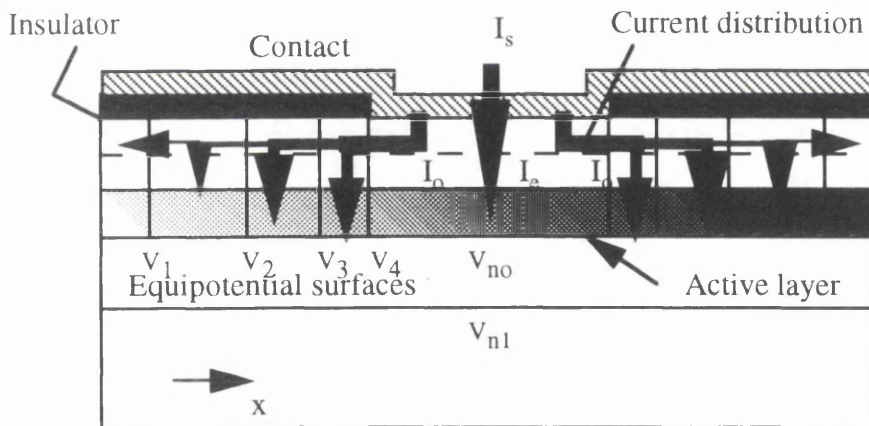
where  $J_s = I_s / SL$  is the total apparent current density;  $S$  is the stripe width and  $\beta = q / nKT$  with  $n=2$  [3].  $R_x^{-1} = (d_3 / \rho_3) + (d_4 / \rho_4)$ , where  $d_3$  (or  $d_4$ ) and  $\rho_3$  (or  $\rho_4$ ) are the thickness and the resistivity of the upper cladding (or P-contact) layer respectively. The solution of (2-1) for  $J_e$  is

$$J_e = \frac{-A - (A^2 - 4J_s^2)^{1/2}}{2} \quad (2-2)$$

$$\text{with } A \equiv -2 [ J_s + 4 / (\beta R_x S^2) ]$$



(a)



(b)

Fig.2-1. Schematic diagrams of (a) current spreading (b) equipotential and current distribution [1] of a laser diode.

Since the N-contact for most lasers is a broad-area one (without stripe), we therefore only consider the combined resistivity of the confining and contact layers as shown in Fig.2-1 (b). From which it can be found that the smallest ( $\rho / d$ ) determines the composite sheet resistivity and will be the layer that dominates the spreading. To quantify this effect, calculated results are shown in Table 2-1 by using  $\rho_4 = 4 \times 10^{-2}$  ohm-cm,  $\rho_3 = 1 \times 10^{-1}$  ohm-cm,  $d_3 = 0.8 \mu\text{m} \gg d_4 = 0.1 \mu\text{m}$ , and  $L = 400 \mu\text{m}$  for the DQW structure B336 (see Appendix).

Table 2-1. Fraction of the spreading / diffusion current to the total applied current ( $I_s$ )

Case	Condition	$2I_o / I_s$ (%)
1	$S = 75 \mu\text{m}$ , $I_s = 300 \text{ mA}$	27.4
2	$S = 12 \mu\text{m}$ , $I_s = 100 \text{ mA}$	72.6
3	$S = 4 \mu\text{m}$ , $I_s = 50 \text{ mA}$	92.5
4	$S = 3 \mu\text{m}$ , $I_s = 30 \text{ mA}$	96.0

( $I_o$ : The lateral current flow as shown in Fig.2-1)

From Table 2-1, it is found that the spreading/diffusion current is only 27.4 of the total apparent current for the  $75 \mu\text{m}$ -wide contact stripe, but is about 96% for the  $3 \mu\text{m}$ -wide stripe. It is obvious that a lateral current spreading is the main contribution to an increase in the apparent threshold current density as the stripe width  $S$  is decreased. When  $S > 75 \mu\text{m}$ , the spreading/diffusion current is relatively negligible. On the contrary, when  $S$  is smaller, the more significant is the lateral current.

It should be noted that the above conclusion and analysis is not only valid for oxide stripe lasers, but also applicable for ridge waveguide lasers, since the width of a ridge waveguide is generally designed to be very small for the sake of single transverse-mode operation and reduction of the threshold current.

### 2-2-2 Transparency and threshold conditions

Fundamental but important concepts relating to diode threshold and transparency are described here for future reference.

#### A. The optical gain of a laser diode

If the detailed and lengthy treatment concerning the basic transitions within a laser diode is not required, the so-called Two-Level Electronic System can then be implemented effectively to analyse the optical gain. The net optical gain  $g(E)$  is given by [4]:

$$\begin{aligned}
 g(E) &= N[f_1(1 - f_2) - f_2(1 - f_1)]\delta(E - \epsilon) \\
 &= N(f_1 - f_2)\delta(E - \epsilon)
 \end{aligned}
 \tag{2-3a}$$

where  $N$  is the number of atoms per unit volume,  $f_1$  and  $f_2$  are the probabilities of finding electrons at energy levels  $E_1$  and  $E_2$  respectively,  $E_{fn}$  and  $E_{fp}$  are the quasi Fermi levels for the conduction and valence bands respectively, and  $\delta(E)$  is a delta function indicating that the optical transitions are allowed only if photon energy  $E$  equals  $\epsilon$ , with  $\epsilon = E_1 - E_2$  (see Fig.2-2).

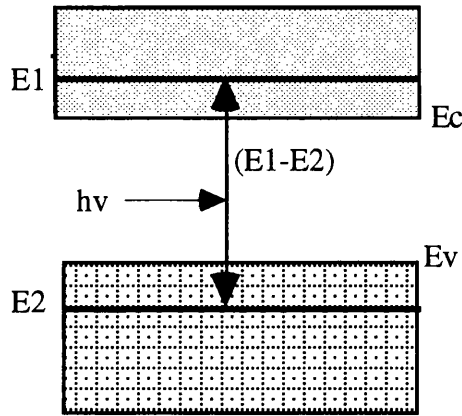


Fig.2-2. The energy band diagram of a Two-Level Electronic System, in which  $E_c$  = conduction band edge, and  $E_v$  = valence band edge.

If the above model is extended to a band system, the optical gain can be written as follows [5]:

$$g(E) = \int B \rho_{red}(E) (f_1 - f_2) \delta(E - \epsilon) dE \quad (2-3b)$$

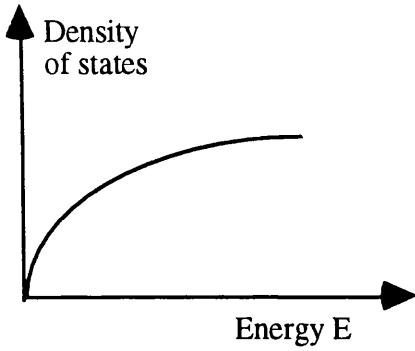
where  $E_1 = \frac{\hbar^2 K^2}{2m_n^*}$ ,  $E_2 = -\frac{\hbar^2 K^2}{2m_p^*} - E_g$ , and  $\rho_{red}$  = Reduced density of states =  $[\rho_c^{-1} + \rho_v^{-1}]^{-1}$ , in which  $\rho_c$  and  $\rho_v$  are densities of states in the conduction and the valence bands respectively.  $m_n^*$  and  $m_p^*$  are the electron and hole effective masses respectively.  $K$  is the electron wavevector and  $E_g$  is the energy bandgap of the material.

### B. Transparency condition

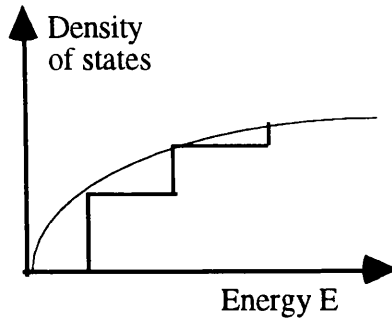
The transparency condition occurs when the optical gain equals the total propagation losses. The first requirement to meet this condition is increasing the gain such that  $g(\epsilon) > 0$ . From the literature, e.g.[4,5], we can obtain:

( 3D case )

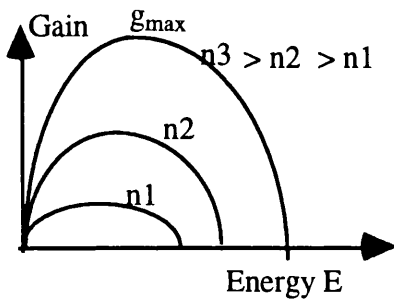
( 2D case )



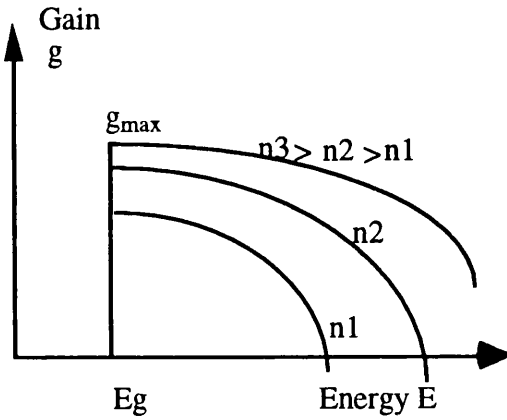
(a1)



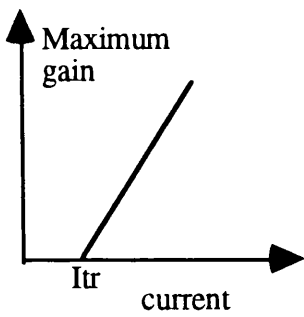
(b1)



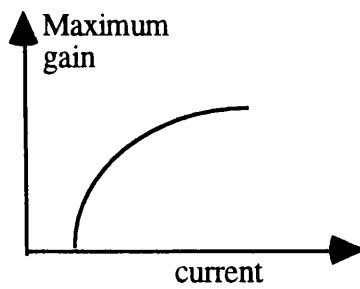
(a2)



(b2)



(a3)



(b3)

Fig.2-3. The density of states, the gain spectra, and the gain-current curves (a) in the 3D and (b) in the 2D spaces respectively.

$$f_1(\epsilon) - f_2(\epsilon) > 0 \quad (2-4)$$

$$\begin{aligned} E_{fn} - E_{fp} &> E_1 - E_2 \\ &= \frac{(\hbar K)^2}{2} \left( \frac{1}{m_n^*} + \frac{1}{m_p^*} \right) + E_g \\ &= h\nu \end{aligned} \quad (2-5)$$

Eq. (2-3) to (2-5) show that the separation of the quasi-Fermi levels must exceed the photon emission energy in order for the downward stimulated emission rate to exceed the upward absorption rate. With more forward bias applied, the effective barrier eventually becomes negligible, the large current and population inversion imply the creation of a large amount of excess carriers near the junction, which makes the quasi-Fermi levels deeper into bands, and also provides much stronger radiative recombination to reach the transparency and then to the threshold conditions.

### C. The carrier-density dependence of gain curves

Fig.2-3(a2) shows the gain responses using carrier densities as parameters for a bulk material. It demonstrates that the photon energy at which the gain peak occurs shifts to higher energy as injection is increased. Conversely, referring to Fig.2-3(b2), carriers in QWs are more "efficient" [7] than in a 3-D space as increased carriers will contribute to gain at its peak, i.e. at the bottom of the 2-D band, whereas in the 3-D case, increased carriers move the gain peak away from the bottom of the band, making all carriers at energies below that of  $g_{\max}$  useless.

### D. Gain-current relationship

It has been found, from many text books, e.g.[4], that a remarkably simple linear approximation for the gain-current relation in the 3D case can be used, i.e.,

$$g_{\max} = A (I - I_{tr}) \quad (2-6a)$$

where A is the differential gain,  $I_{tr}$  is the transparency current representing the injection current needed to reach the transparency condition, and I is the injection current.

In a quantum well laser diode, the relationship between gain per well, g, and the current density per well, J, is according to McIlroy et al [8]:

$$g(J) = g_o \left[ \ln \left( \frac{J}{J_o} \right) + 1 \right] \quad (2-6b)$$

where  $g(J)$  is the gain per well,  $g_o$  is the optimum gain coefficient per well and  $J_o$  is the current density per well at which the ratio of  $(g/J)$  is maximized on the  $g$ - $J$  curve of a QW laser diode[8]. This expression can be rearranged in terms of the transparency current density,  $J_{tr}$ , where the gain per well is zero:

$$g(J) = g_o \ln \left( \frac{J}{J_{tr}} \right) \quad (2-6c)$$

Although the spectral gain curve in the 2D case has a larger slope (Fig.2-3 (b3)) than in the 3D case, the trade-off is that the gain will saturate at a given finite value when the electron and hole states are fully occupied (see note), whereas  $g_{max}$  never saturates in a 3D crystal when carriers are injected.

*(Note): Referring into (2-3b), the allowed density of states, i.e.  $\rho_{red}(f_1 - f_2)$ , will reach its maximum at high injection level. In this case, the quasi Fermi levels will deepen into the conduction and valence bands and the allowed states will be fully occupied, since  $f_1 \sim 1$ , and  $f_2 \sim 0$  with  $f = [1 + \text{EXP}(E - E_f)/KT]^{-1}$ , in which  $E_f$  and  $E$  are quasi Fermi level and electron level respectively. In summary, the optical gain will saturate easily only if the density of states is small ( e.g.  $N=1$ ) and the number of carriers is high, in order to completely invert the allowed quantum states.*

#### E. The threshold current of an MQW laser diode

Considering the confinement factor for an MQW laser diode at threshold, Eq. (2-6c) can be re-arranged as :

$$J_{th} = NJ_{tr} \exp [g_{th} / (N\Gamma_w g_o) ] \quad (2-6d)$$

where  $N$  is the number of the quantum wells and  $\Gamma_w$  is the confinement factor per well. From the above, it is obvious that the threshold current density strongly depends on the confinement factor, the number of QWs, and the optical gain per well, in addition to the transparency current density and the threshold gain.

Fig.2-4 shows the current-density dependence of modal gain, with varying number of QWs, for MQW laser diodes. From the point of view of the threshold current, at low loss ( $< 20 \text{ cm}^{-1}$ ) [6], the single quantum well (SQW) laser is better, since it has lower transparency current density mainly because the allowed quantum

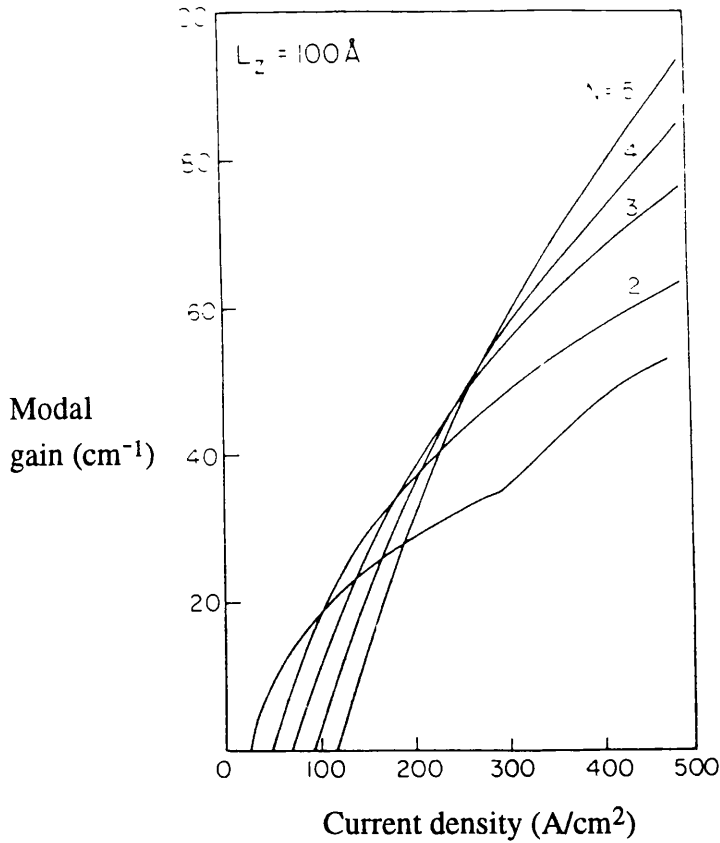


Fig.2-4 The modal gain as a function of the injection current density  $J$  with varying quantum-well numbers  $N$ . The well thickness is denoted as  $L_z$  [6].

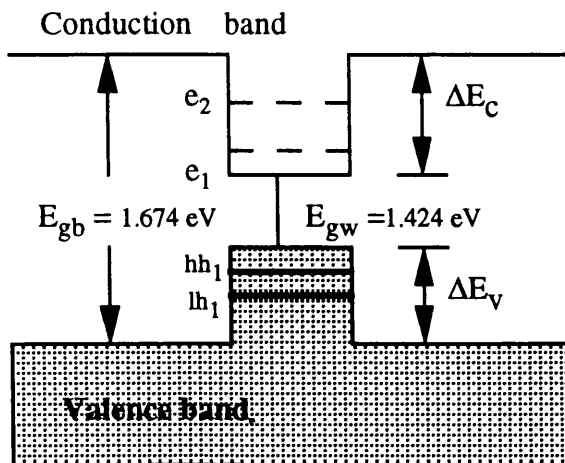


Fig.2-5 Schematic energy band diagram of an AlGaAs-GaAs QW laser diode at 300 °K

states of only one quantum well have to be inverted [9]. At high loss ( $> 20 \text{ cm}^{-1}$ ), the MQW is always better because the gain stems from a high-slope part of the gain-current (g-I) curve, instead of the saturated part of the SQW g-I curve. It is evident that MQW structures have the advantage of higher differential gain, which leads to higher modulation frequencies and narrower linewidths [10].

For an MQW ( $N>1$ ) laser, it should be noted that gain saturation will only occur at very high current injection, because there is a huge number of quantum states to be filled.

### 2.2.3 Energy band diagrams

#### A. Theory

In a double-heterostructure (DH) laser diode, if the thickness of the active layer is comparable to the de Broglie wavelength [11], the carrier motion normal to the active layer in this structure is restricted. Under this circumstance, the carriers moving in this direction, denoted as  $z$ , behave as if in a 1-D quantum well, and hence the kinetic energy of carriers in the  $z$  direction is quantized.

The discrete energy levels in the  $z$ -direction are obtained by solving the Schrödinger equation for a 1-D potential well as given by [11]

$$-\frac{\hbar^2}{2m} \frac{d^2 \psi}{dz^2} = E\psi \quad \text{for } |z| < \frac{a}{2} \quad (2-7)$$

$$-\frac{\hbar^2}{2m} \frac{d^2 \psi}{dz^2} + V\psi = E\psi \quad \text{for } |z| \geq \frac{a}{2} \quad (2-8)$$

where  $\psi$  is the wave function (or eigenfunction),  $a$  is the well thickness and  $V (>E)$  is the depth of the potential well. For a finite well, the energy levels and wave functions can be obtained from (2-7) and (2-8). The general solution is:

$$\begin{aligned} \psi &= A \exp(K_1 z) && (z \leq -\frac{a}{2}) \\ &= B(\sin K_2 z \text{ or } \cos K_2 z) && (-\frac{a}{2} < z < +\frac{a}{2}) \\ &= C \exp(-K_1 z) && (z \geq +\frac{a}{2}) \end{aligned} \quad (2-9)$$

$$\text{where } K_1 = \left[ \frac{2m(V-E)}{\hbar^2} \right]^{1/2}, \quad K_2 = \left( \frac{2mE}{\hbar^2} \right)^{1/2}.$$

At the boundaries  $z=+a/2$  and  $z=-a/2$ , the values of  $\psi$  and  $(m^{-1}d\psi/dz)$  must be continuous. After simplifications, we can obtain a transcendental equation given by (2-10):

$$(\tan U \text{ or } -\cot U) = \sqrt{\left[\frac{U_o^2}{U^2} - 1\right]} \quad (2-10)$$

$$\text{where } U \equiv \frac{K_2 a}{2} \quad \text{and} \quad U_o^2 \equiv \frac{mV a^2}{2\hbar^2}$$

For a specific quantum barrier height  $V$ , the energy levels  $E$ , i.e. the eigenvalues, can be obtained from either a numerical or graphical solution of eq. (2-10).

### B. Application to compute the electronic levels for a DQW structure

For the DQW structure B423 (detailed in section 2-3), the aluminum fraction of the  $\text{Al}_x\text{Ga}_{1-x}\text{As}$  barrier layer is 0.2, the energy bandgaps at room temperature are 1.674 eV for AlGaAs, and 1.424 eV for GaAs [12].

Referring to Fig. 2-5, the energy levels calculated using Eq.(2-10) are listed in Table 2-2. ( $m_n^* = 0.067m_0$ ,  $m_{hh}^* = 0.62m_0$ , and  $m_{lh}^* = 0.082m_0$ )

Table.2-2 Calculated electronic energy levels for DQW B423

QW thickness (nm)	Electron levels (meV)	Hole levels (meV)	Lasing wavelength (nm)
10	$E_1=26.95$	$hh_1=4.5, \quad lh_1=20.26$	$\lambda_{eh}=852; \lambda_{el}=843$
7	$E_1=42.55$	$hh_1=8.15, \quad lh_1=31.46$	$\lambda_{eh}=841; \lambda_{el}=807$

( Note):  $E_1$ =First electronic level,  $hh_1$ =First heavy-hole level,  $lh_1$ =First light-hole level,  $\lambda_{eh}$  = Lasing wavelength between  $E_1$  and  $hh_1$  levels;  
 $\lambda_{el}$  = Lasing wavelength between  $E_1$  and  $lh_1$  levels

To obtain the electron levels,  $V$ ,  $\Delta E_c$  for this case is set to 0.15 eV by assuming  $\Delta E_c / \Delta E_v = 3/2$ . Looking at the table, it can be seen that the most probable lasing wavelength, i.e.  $\lambda_{eh}$ , for the structure with 10-nm thick QWs, is 852 nm, which is the same as the photoluminescence peak observed in experiments.

Furthermore, it can be found that quantum states are further away from the bottom of energy bands if the thickness of the QW decreases. This result is consistent

with the Uncertainty Principle, indicating that the energy of a quantum will be perturbed by a larger amount, if this quantum is localized in a narrower region.

#### 2-2-4 Excitons

As for the electron and the proton in a hydrogen atom, the electron and hole have opposite charges and attract each other and can form bound states called excitons. Because of this Coulombic attraction, exciton states have a lower total energy than free electrons and holes and therefore appear just below the bandgap in the absorption spectra.

At low temperature, such as the near liquid helium temperature where photoluminescence measurements are generally made, and at low excitation intensities, the injected electrons and holes can combine to form free excitons or the electron-hole pair can be bound to an impurity to form a bound exciton [13]. Recombination then proceeds by the annihilation of these excitons rather than by band-to-band recombination.

By using the centre-of-mass approach [14], the total energy  $E_n$  of a 3-D exciton is similar to that of a hydrogen atom and can be represented by

$$E_n = E_g - \left(\frac{1}{n^2}\right)R \quad \text{with} \quad R = \frac{m_r}{2} \left[ \frac{e^2}{4\pi\epsilon_r\epsilon_o\hbar} \right]^2 \quad (2-11a)$$

$$\text{and} \quad m_r = \left[ \frac{1}{m_n} + \frac{1}{m_p} \right]^{-1}$$

where  $n$  is the quantum number,  $m_r$  is the reduced mass of this centre-of-mass system,  $E_g$  is the bandgap energy and  $R$  is the Rydberg constant.

The second term of Eq. (2-11a) represents the binding energy of an exciton in a crystal. For GaAs, using  $\epsilon_r = 13.1$ ,  $m_n = 0.067 m_o$ ,  $m_{hh} = 0.45 m_o$  and  $m_{lh} = 0.082 m_o$ , the binding energies of light-hole and heavy-hole excitons are 3.0 meV and 4.7 meV respectively. At room temperature, the thermal energy  $KT = 26$  meV. This implies that excitons break up into free carriers very easily, because there are many phonons present. Similarly, if impurity doping increases, excitons tend to dissociate under local electric fields [10]. Excitonic features in bulk GaAs are only observed at room temperature. In specially pure materials, the band-to-band recombination process dominates typically.

Excitons confined in a quantum well are called 2-D excitons. The binding energy for an exciton in the 2-D limit is given by [15]

$$E_n = -\frac{R}{\left(n - \frac{1}{2}\right)^2} . \quad (2-11b)$$

When  $n = 1$ , Eq. (2-11b) gives the binding energy  $E_1 = -4R$  and implies that a 2-D exciton has four times the binding energy of a free 3-D exciton! This binding energy reflects its confinement in the quantum well. The higher binding energy of a 2-D exciton is very important, because excitonic properties can readily be observed optically even at room temperature. Examples like this will be shown later in section 4-5 in the photocurrent response of a QW structure.

By carefully examining the excitonic lines in the spectrum of a crystal or in QW structures, structural damage, lifetime broadening caused by acoustic phonon scattering, the chemical nature of the impurity, lasing-wavelength shifts due to the electric field applied to QWs and many other interesting phenomena can be observed [13].

## 2-3 Optical properties

### 2-3-1 Variation of the refractive index of a QW laser diode

There are many factors affecting the refractive index of a QW semiconductor waveguide. For our purpose, the fluctuation of the total effective refractive index  $\Delta n$  can be expressed by

$$\Delta n(\text{Total}) = \Gamma \Delta n_1 (\text{Free carriers}) + \Gamma \Delta n_2 (\text{Injected carriers}) + \Delta n_3 (\text{Molar fraction}) \\ + \Delta n_4 (\text{Temperature change}) + \Gamma \Delta n_5 (\text{E-O effects}) + \Delta n_6 (\text{QWI}) + \Delta n_7 (\text{Ridge step})$$

where  $\Gamma$  is the confinement factor of the waveguide representing the weighing of the optical field interacting with carriers,  $\Delta n_1$  and  $\Delta n_2$  are variations produced by the free and injected carriers respectively,  $\Delta n_3$  is from the molar-fraction (i.e.  $x$ ) change of  $\text{Al}_x\text{Ga}_{1-x}\text{As}$  compounds,  $\Delta n_4$  is from temperature variation,  $\Delta n_5$  is from linear and nonlinear electrooptic effects,  $\Delta n_6$  is from QW intermixing, and  $\Delta n_7$  is from the ridge step of the waveguide. Among those,  $\Delta n_3$ ,  $\Delta n_6$ , and  $\Delta n_7$  will be fixed when device fabrication is finished. Generally,  $\Delta n_5$  is negligible (see note) compared to other variations such as  $\Delta n_2$  or  $\Delta n_3$ . As a result, the total variation is dominated by

$$\Delta n = \Gamma \Delta n_{1,2} (\text{Carriers}) + \Delta n_4 (\text{Temperature change}) + \Delta n_7 (\text{Ridge step})$$

where the first term includes both free and injected carriers. The first and the second terms of the above expression can be given by the following classical approximations

[1,16]

$$\Delta n (\text{carriers}) = -\left(\frac{Ne^2}{2m\omega^2\epsilon}\right) n \quad (2-12a)$$

$$\Delta n_6(T) = 4 \times 10^{-4} \Delta T \quad (2-12b)$$

where  $\Delta T$  is the temperature variation,  $N$  is the free carrier concentration,  $e$  is the electron charge,  $m$  is the electron/hole effective mass,  $n$  is the refractive index,  $\omega$  is the frequency of the light wave and  $\epsilon$  is the dielectric constant. Typically, a GaAs diode lasing near bandgap has a threshold carrier density  $n_{th} = 1 \times 10^{18} \text{ cm}^{-3}$ . At room temperature, if the wavelength is near  $0.9 \mu\text{m}$ , the  $n = 3.6$  and  $\Delta n (\text{carriers}) = -1.5 \times 10^{-21} N$ . For DQW GaAs/AlGaAs lasers,  $\Gamma = 0.06$  is typical [6], with contributions from both free and injected carriers,  $\Gamma \Delta n (\text{carriers})$  ( $= -2.7 \times 10^{-4}$  by assuming  $N = 3 \times 10^{18} \text{ cm}^{-3}$ ) is in the same order, but with opposite polarity, as that from temperature change ( $\Delta T = 1-2 \text{ }^\circ\text{K}$ ). In this case, the temperature induced guiding cancels out the carrier-induced defocusing effect and makes only a small contribution to the total guiding [17].

Furthermore, Agrawal [18] showed that if the lateral refractive-index step of a ridge waveguide structure is increased beyond  $4 \times 10^{-3}$ , the lasing will then transit from a gain-guiding regime into an index-guiding regime .

*(Note): The  $\Delta n$  change due to the linear electrooptic effect in a GaAs crystal is*

*$\Gamma E(n^3 r/2)$ , which is in the order of  $10^{-5}$  by using field intensity  $E$  of  $5 \text{ V}/\mu\text{m}$ , refractive index  $n = 3.65$  and electrooptic coefficient  $r = 4 \times 10^{-12} \text{ m/V}$ .*

### 2-3-2 Gain-guiding and index-guiding regimes

The optical modes of a gain-guided laser, such as the oxide stripe laser, are confined by the lateral variation of the optical gain. This gain is proportional to the density of injected carriers, which is in turn influenced by the carrier diffusion or spreading.

For an index-guided laser, the refractive-index discontinuity between the active and the cladding layers is formed by a lateral effective refractive-index step, which is responsible for the lateral mode confinement. In a ridge waveguide laser, there are two opposing mechanisms governing the lateral index change  $\Delta n_L$  :

$$\Delta n_{\text{net}} (\text{Lateral}) = \Delta n_{\text{eff}} (\text{Rib}) + \Delta n (\text{Carriers})$$

where  $\Delta n_{\text{eff}}(\text{Rib}) = H(W/2 - |x|)\Delta n_L$ ,  $H$  is the Heaviside step function,  $W$  is the ridge width,  $\Delta n_L$  is the difference in refractive index between the two lateral regions,  $\Delta n(\text{Carriers}) = -(a/2k_0)RN$  [18],  $a$  is the gain constant ( $\text{cm}^2$ ),  $k_0 = \omega / c$ ,  $R$  is the linewidth enhancement factor, and  $N$  is the injected carrier density of the diode.

For small positive  $\Delta n_{\text{net}}$ , the laser operates in a gain-guided regime. When it is increased beyond a critical value,  $4 \times 10^{-3}$  [18], the laser then operates in a stable index-guided regime. Before going into that regime, the index-guiding induced focusing helps to contract the lateral mode, and the peak gain starts to decrease with an increase of  $\Delta n_L$ . When the gain and mode profiles overlap significantly and  $I_{\text{th}}$  saturates, the index-guiding sets in. Once the laser is operating in the index-guided regime, the carrier-induced defocusing plays a relatively minor role [18], since the carrier concentration is, clamped in this condition on the average. From the above formula, it is evident that the lateral refractive index difference  $\Delta n_L$ , the linewidth enhancement factor  $R$ , and the carrier density  $N$  play crucial roles in determining the guiding mechanism.

### 2-3-3 The effective refractive index of a waveguide structure

A QW structure forms a multi-layer waveguide. The effective refractive index for a QW structure is crucial for realizing its most important wave-propagation properties. For instance, the index step for a ridge waveguide and the step between the grating tooth and trench areas, can be estimated well in advance, and they are vital to the success of device fabrication and characterisation.

The departmental program F-wave, a variational method, was used for the simulations. The following are calculated results for both symmetric (B423) and asymmetric (B564) DQW structures.

#### A. Symmetric DQW structure

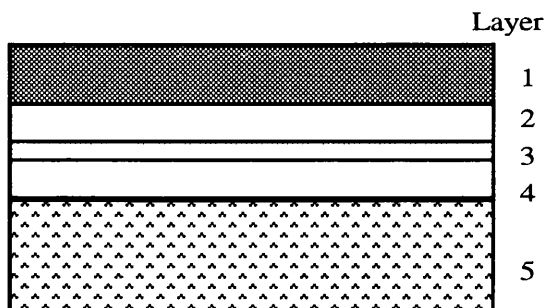
The symmetric DQW structure was simulated with a 5-layer slab waveguide as shown in Fig.2-6 (a) and Table 2-3, in which the thickness of the upper cladding layer was changed. The dependence on the thickness of the upper cladding layer of the effective refractive index is shown in Fig.2-6 (b), and the result is also listed in Table 2-4. In order to obtain a lateral index difference of  $4 \times 10^{-3}$ , the ridge step should be etched down by  $1 \mu\text{m}$ , thereby providing the required stable index-guiding.

#### B. Asymmetric DQW structure

The asymmetric DQW structure, B564, was used in this work to obtain strong optical coupling in a deep-grating DBR laser diode. Similar results to those above were also obtained and demonstrated in Fig.2-5 and in Table 2-4.

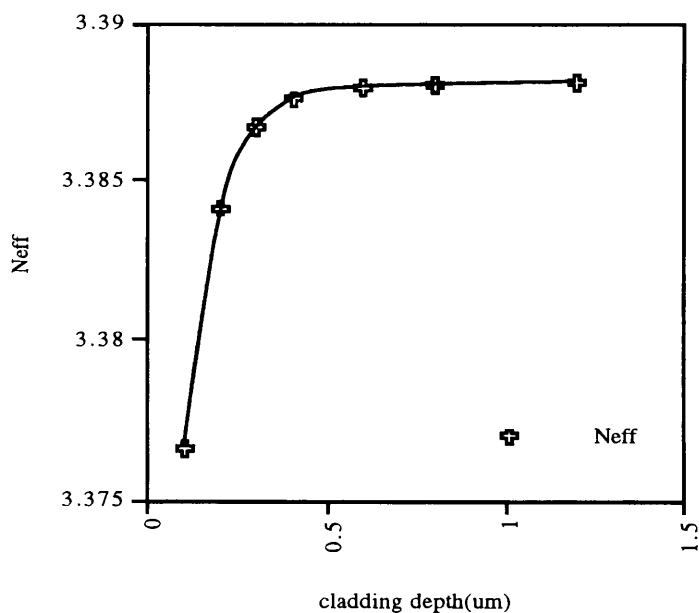
Table.2-3. Five-layer slab waveguide for B423(see Appendix) simulation

Layer no.	(Material) Al fraction of $Al_xGa_{1-x}As$	Refractive index [19]	Layer thickness ( $\mu m$ )
1	0.4	3.321	( 0.1 - 1.2 )
2	0.2	3.452	0.1
3	GaAs QW wells	3.655	0.02
4	0.2	3.452	0.1
5	0.4	3.321	2.0



(a)

B423- Five- layer slab waveguide



(b)

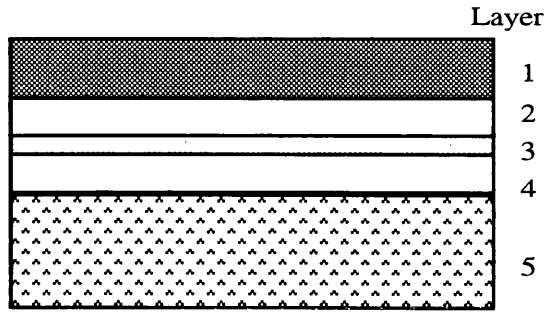
Fig.2-6 ((a).Five-layer slab symmetric waveguide structure (b)Effect of thickness of the upper cladding layer on effective refractive index (TE<sub>00</sub> mode).

Table.2-4. Effective refractive index for the 5-layer slab B423

$d_{clad}$ ( $\mu m$ )	0.1	0.2	0.3	0.4	0.6	0.8	1.2
$N_{eff}$	3.3766	3.3841	3.3867	3.3876	3.3880	3.3881	3.3881

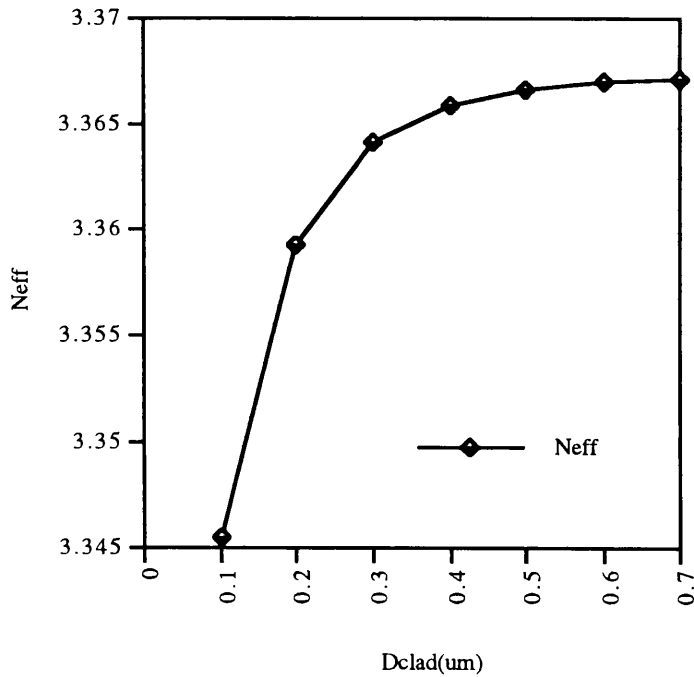
Table.2-5. Five-layer slab waveguide for B564 (see Appendix)simulation

Layer no.	(Material) Molar fraction of $Al_xGa_{1-x}As$	Refractive index [19]	Layer thickness ( $\mu m$ )
1	0.79	3.08	( 0.1 - 0.7 )
2	0.2	3.452	0.142
3	GaAs QW wells	3.655	0.016
4	0.2	3.452	0.0524
5	0.4	3.321	0.7



(a)

Five layer slab-B564



(b)

Fig.2-7 (a)Five-layer asymmetric waveguide structure  
(b)Effect of thickness of the upper cladding layer,  $D_{clad}$ , on effective refractive index (TE00 mode)

Table.2-6. Effective refractive index for the 5-layer slab B564

$D_{clad} (\mu m)$	0.1	0.2	0.3	0.4	0.5	0.6	0.7
$N_{eff}$	3.3454	3.3592	3.3640	3.3658	3.3666	3.3669	3.3670

Further characterization of these structures will be described in details in chapter 5 and 6.

### 2-3-4 Confinement factors for an MQW structure

It is important to know the optical confinement of the ridge waveguide either for monitoring the fabrication or for the diode operation. The details of the 2-D optical-mode plot can be obtained from our departmental program , F-Wave, written by M.Taylor. From the simulated results, lateral(horizontal) and transverse (vertical) confinement can be computed as follows [20]:

Vertical confinement is

$$\Gamma_v(x) = \frac{\int_{-d/2}^{d/2} E_y^2(x,y)dy}{\int_{-\infty}^{\infty} E_y^2(x,y)dy}, \quad (2-13a)$$

horizontal confinement is

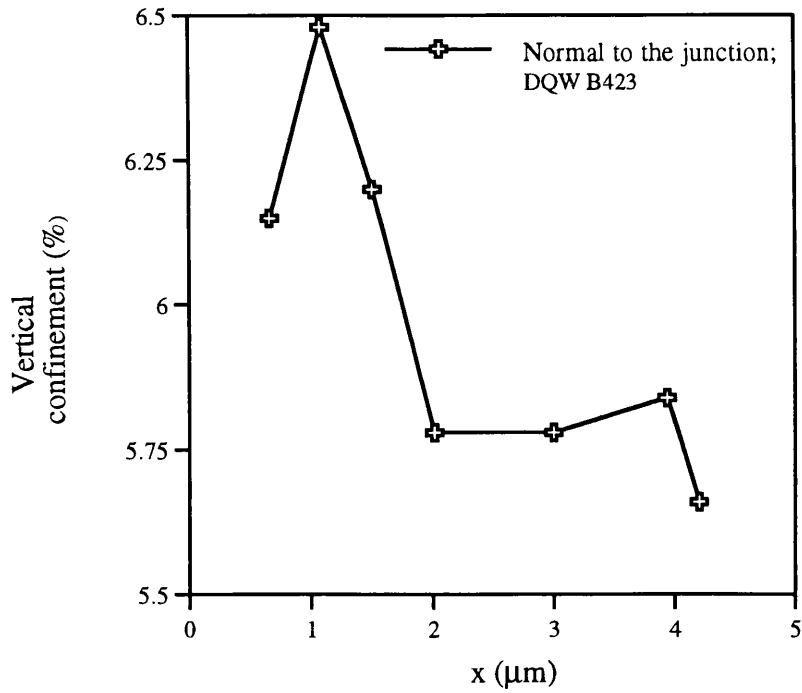
$$\Gamma_H(y) = \frac{\int_{-w/2}^{w/2} E_x^2(x,y)dx}{\int_{-\infty}^{\infty} E_x^2(x,y)dx}, \quad (2-13b)$$

and the total confinement at a point (x,y) is

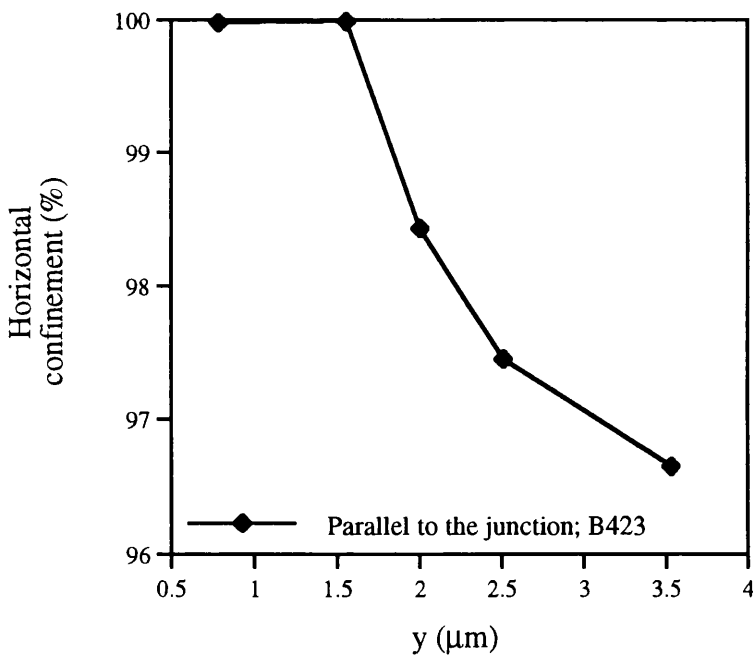
$$\Gamma(x,y) = \Gamma_v * \Gamma_H$$

where d is the (vertical) thickness of the active layer, and W is the width of the ridge. Calculated results are shown in Fig.2-8. Near the centre of the rib, the horizontal confinement factor  $\Gamma_H = 99.99\%$  and the vertical confinement factor  $\Gamma_v \approx 5.6\%$ . The total confinement factor estimated approximately by Arakawa and Yariv [6] (see note below) is 6 % for this structure, which deviates from the computed result by 7 %. For the asymmetric structure B564, the calculated confinement factor is 5.5 % . Compared to the estimated result of 4.8 %, the discrepancy is 13%. It can therefore be concluded that Arakawa and Yariv's formula is good for a quick estimation of waveguide properties, with a reasonably small error.

In the above calculation, however, only passive conditions which do not include the carrier-induced effects are considered. The real confinement factor would be different from the calculated one to a certain extent, because the refractive index of the QW structure may be affected by various mechanisms as described before, which were not taken into account in the calculations.



(a)



(b)

Fig. 2-8 (a) Vertical confinement, as a function of horizontal position, and (b) horizontal confinement, as a function of vertical position, factors of a ridge waveguide (width=4 μm, height = 0.5 μm) (The centre of the ridge : x = 4 μm, y = 1.7 μm ).

(Note): According to Arakawa and Yariv [6],  $\Gamma_r = 0.3N(L_z/L_o)$  where  $N =$  number of QWs,  $L_z =$  QW thickness, and  $L_o = 100$  nm. This formula was generated by assuming the total thickness of QWs, barriers and waveguide core to be 200 nm.

### 2-3-5 Single-mode operation

In the lateral and transverse (vertical) directions, single mode control is very important for obtaining a coherent laser output, such as is required for the launching of light from a laser into a fibre. From electromagnetism, single vertical-(transverse) mode operation is possible only if [21]

$$d < d_{critical} = \frac{\lambda}{2} (n_a^2 - n_c^2)^{-1/2} \quad (2-14)$$

where  $d$  is the thickness of the active layer;  $n_a$  and  $n_c$  are refractive indices of the active and the cladding layers respectively.  $n_a = 3.655$  and  $n_c = 3.452$  for the QW structure B423, so  $d_{critical} = 0.5 \mu\text{m}$  at a wavelength of 850 nm.

On the other hand, single lateral-mode operation can only be achieved if [21]

$$W < W_{critical} = \frac{\lambda}{(8n_e \Delta n_L)^{1/2}} \quad (2-15)$$

where  $W$  is the width of the ridge,  $n_e$  is the average effective refractive index, and  $\Delta n_L$  is the lateral refractive index step. If the etch depth is  $0.7 \mu\text{m}$  for the above material (B423), the simulated  $n_e = 3.422$  and  $\Delta n_L = 3.75 \times 10^{-3}$ , so the critical width  $W_{critical}$  is  $2.7 \mu\text{m}$  at the wavelength of 850 nm. In other words, the above ridge waveguide structure gives single lateral and vertical mode operation only if the active layer is thinner than  $0.5 \mu\text{m}$  and the ridge is narrower than  $2.7 \mu\text{m}$ . However, a shallower etch of the rib results in a smaller  $\Delta n_L$  and a wider critical width. In this case, the carrier-induced defocusing (with  $N = 3 \times 10^{18} \text{ cm}^{-3}$ ) will dominate over  $\Delta n_L$ , and the laser will then go from the index-guiding into the gain-guiding regime.

Furthermore, single -mode operation of a laser is more difficult to achieve in the longitudinal direction, compared to the other two directions, because it must have special arrangements, such as distributed feedback (DFB) or distributed Bragg reflectors (DBR), to meet the criterion of single-mode operation. Ways to maintain single longitudinal-mode operation in a DBR laser will be described in chapter 3 and then discussed further in chapter 6.

## 2-4 Summary

In section 2-2, a conceptual introduction to current spreading and diffusion was described. A model was used to describe the effects of contact stripe geometry on the spreading and diffusion current components. After that, the basic mechanisms to reach transparency, the gain spectra and gain-current relationships, and the threshold conditions for both 2D and 3D cases were established for future reference. A quantum-mechanical approach for computing electronic energy levels was undertaken for a 1-D quantum well with a finite barrier. A transcendental equation was derived and then applied to calculate the energy levels for the DQW structure used for device fabrication in this work. By using this approach, excitonic phenomena in the two-dimensional and three-dimensional cases were described.

Section 2-3 describes the factors affecting the fluctuation of the refractive index in a QW laser diode. A variational method was used to simulate the QW structures and confinement factors were then calculated. Guidelines for single-mode operation were finally described in the last section.

## 2-5. References

- [1] G.H.B.Thompson, ' *Physics of Semiconductor Laser Devices* ', Section 6-3, New York, Wiley, 1980.
- [2] T.P.Lee, C.A.Burrus, J.A.Copeland, A.G.Dentai, and D.Marcuse, 'Short-cavity InGaAsP injection lasers: Dependence of mode spectra and single-longitudinal-mode power on cavity length', pp.1101-1113, V.18, No.7, IEEE J. Quantum Electron., 1982.
- [3] W.T.Tsang, 'The effects of lateral current spreading, carrier out-diffusion, and optical mode losses on the threshold current density of GaAs-Al<sub>x</sub>Ga<sub>1-x</sub>As stripe-geometry DH lasers', pp.1031-1044, 49(3), J.Appl.Phys., 1978.
- [4] H.C.Casey and M.B.Panish, '*Heterostructure lasers*', section 3-2 , Part A, New York, Academic Press,1978.
- [5] Y.Arakawa, '*Low Dimensional Electronic Systems for Lasers*', lecture note at NATO Advanced Study Institute at Erice of Italy, July, 1993.
- [6] Y.Arakawa and A.Yariv, 'Theory of gain, modulation response, and spectral linewidth in AlGaAs quantum well lasers', pp.1666-1674, V.21, No.10, IEEE J. Quantum Electron., 1985.
- [7] C.Weisbuch, 'Low dimensional structures in semiconductors', lecture note at NATO Advanced Study Institute at Erice of Italy, July, 1993.
- [8] P.W.A.McIlroy, A. Kurobe and Y.Uematsu, 'Analysis and applications of theoretical gain curves to the design of multi-quantum-well lasers', V-21, No.12, pp.1958-1963, IEEE J. Quantum Electron. 1985.

- [9] A. Kurobe, H.Furuyama, S.Naritsuka, N.Sugiyama, Y.Kokubun and M. Nakamura, 'Effects of well number, cavity length, and facet reflectivity on the reduction of threshold current of GaAs/AlGaAs multiquantum well lasers', pp.635-640, V.24, No.4, IEEE J. Quantum Electron., 1988.
- [10] E.E.Mendez and K.V.Klitzing, '*Physics and applications of quantum wells and superlattices*', second edition, Plenum Press, New York, 1989.
- [11] John Davies, '*Nanoelectronics*', chapter 3, lecture note of Department of Electronics and Electrical Engineering, Glasgow University, 1993-1994.
- [12] H.C.Casey and M.B.Panish, '*Heterostructure lasers*', P.193, part A, New York, Academic Press,1978.
- [13] V.Swaminathan and A.T. Macrander, '*Material Aspects of GaAs and InP Based structures*', chapter 5, Prentice Hall, New Jersey, 1991.
- [14] John Davies, '*Nanoelectronics*', chapter 9, lecture note of Department of Electronics and Electrical Engineering, Glasgow University, 1993-1994.
- [15] R.C.Miller, D.A.Kleinmann, and A.C Gossard, 'Energy-gap discontinuities and effective masses for GaAs-AlGaAs quantum wells', pp.7085-7087 B29, Phys.Rev.1984.
- [16] C.H.Henry, R.A.Logan, and K.A.Bertness, 'Spectral dependence of the change in refractive index due to carrier injection in GaAs lasers',52(7), pp.4457-4461, J. Appl. Physics, 1981.
- [17] H.C.Casey and M.B.Panish, '*Heterostructure lasers*', P.252, part B, New York, Academic Press,1978.
- [18] G.P.Agrawal, 'Lateral analysis of quasi-index-guided injection lasers:: Transition from gain to index guiding', V.-2, No.4,pp.537-543, IEEE J.Quantum Electron., 1984.
- [19] S. Adachi, 'GaAs, AlAs, and  $\text{Al}_x\text{Ga}_{1-x}\text{As}$ : Material parameters for use in research and device applications', R1-29, 58(3), J. Appl. Phys., 1985.
- [20] G.P.Agrawal and N.K.Dutta, '*Long-Wavelength Semiconductor Lasers*', p.184, Van Nostrand Reinhold, New York, 1986.
- [21] G.P.Agrawal and N.K.Dutta, '*Long-Wavelength Semiconductor Lasers*', section 2-5, Van Nostrand Reinhold, New York, 1986.

## Chapter 3. Theories of extended-cavity and distributed-Bragg-reflector lasers

### 3-1 Introduction

In the presence of fibre-chromatic dispersion, the unwanted longitudinal modes limits the data transmission rate by reducing the fibre bandwidth. So the lasers used in fibre optic communications should be single-moded to fulfill the requirement of high repetition rate. The linewidth-narrowed, DFB and DBR, lasers are fabricated as extended-cavity structures with a long passive grating section providing longitudinal mode selection [1].

Based upon the Schawlow-Townes formula [see Appendix, section 3-7], it is obvious that the linewidth of the laser can be narrowed by either increasing the cavity length and power output or by decreasing the absorption losses and the linewidth enhancement factor. A long extended-cavity structure with low propagation losses in the passive waveguide section is required to achieve a narrow linewidth.

A detailed theoretical model is derived in section 3-2 to describe the propagation losses of the passive waveguide section. Additionally, wavelength shifts for an extended cavity laser due to various mechanisms are also depicted.

A DBR laser has an extended cavity to provide longitudinal mode selection. Section 3-3 gives a simple description of the operation of an DBR laser.

### 3-2 Extended cavity lasers

#### 3-2-1 Propagation losses

For a QW laser at threshold, the gain must be equal to the loss, according to:

$$\begin{aligned}\Gamma g_{th} &= \alpha_i + \frac{1}{L} \ln\left(\frac{1}{R}\right) \\ &\equiv \alpha_i + \alpha_m \quad \text{with } \alpha_m = \frac{1}{L} \ln\left(\frac{1}{R}\right)\end{aligned}\quad (3-2)$$

where  $g_{th}$  is the threshold gain,  $\Gamma$  is the overall confinement factor defined as the fraction of the electromagnetic radiation within the gain region.  $\alpha_i$  is the total internal loss including band - to - band absorption, free - carrier absorption, scattering, and evanescent coupling losses.  $\alpha_m$  is the mirror loss,  $L$  is the cavity length, and  $R$  is the facet reflectivity. The relationship between gain per well,  $g$ , and the current density per well,  $J$ , in a quantum well laser structure is given by [2] :

$$g(J) = g_o \left[ \ln \left( \frac{J}{J_o} \right) + 1 \right]$$

where  $g(J)$  is the gain per well,  $g_o$  is the optimum gain coefficient per well,  $J_o$  is the current density per well at the optimum working point. This equation can also be expressed in terms of the transparency current density,  $J_{tr}$ , at which the gain per well is zero:

$$g(J) = g_o \ln \left( \frac{J}{J_{tr}} \right) \quad (3-3a)$$

It should be noted that the above expression holds only at the peak of the optical gain spectrum, but is a good approximation for the degree of detuning found in this work (discussed in chapter 6). In particular, at threshold, (3-3a) becomes:

$$g_{th}(J_{th}) = g_o \ln \left( \frac{J_{th}}{J_{tr}} \right) \quad (3-3b)$$

which can be re-arranged, by using eq.(3-2), as:

$$\begin{aligned} \ln J_{th} &= \frac{g_{th}}{g_o} + \ln(J_{tr}) = \frac{\alpha_i + \alpha_m}{\Gamma g_o} + \ln(J_{tr}) \\ &= - \left[ \frac{\ln R}{\Gamma g_o} \right] \frac{1}{L} + \left[ \frac{\alpha_i}{\Gamma g_o} + \ln(J_{tr}) \right] \end{aligned} \quad (3-4)$$

For an extended cavity laser, as shown in Fig.3-1, with active and passive section lengths of  $L_a$  and  $L_p$  respectively, a new threshold current density,  $J_{th}'$ , is required. The ratio of the current densities is thus [3]

$$\begin{aligned} \ln [J_{th}' / J_{tho}] &= \ln [J_{th}' / J_{tho}] \\ &= \frac{\alpha_p}{\Gamma g_o} (L_p / L_a) + \frac{1}{\Gamma g_o L_a} \ln(1/\kappa) \end{aligned} \quad (3-5)$$

where  $J_{tho}$  is the threshold current density for a laser with a zero-length passive section defined in Eq. (3-4),  $\kappa$  is the coupling coefficient (typically slightly less than one) between the active and passive sections of the laser, and  $\alpha_p$  is the loss coefficient in the passive section.

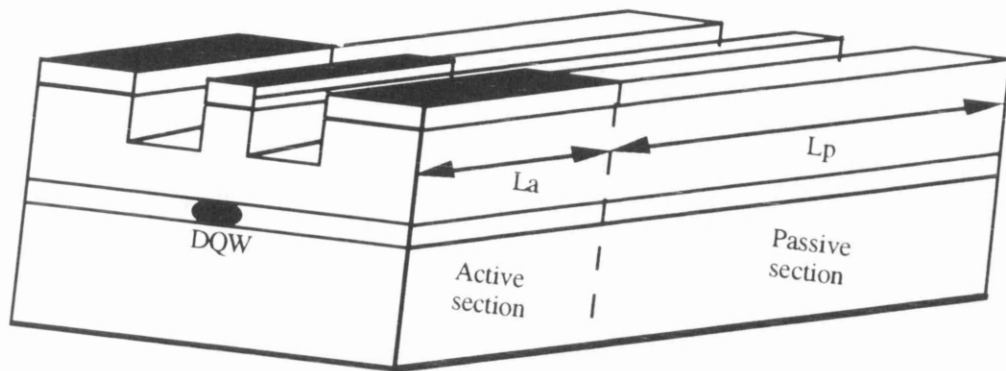
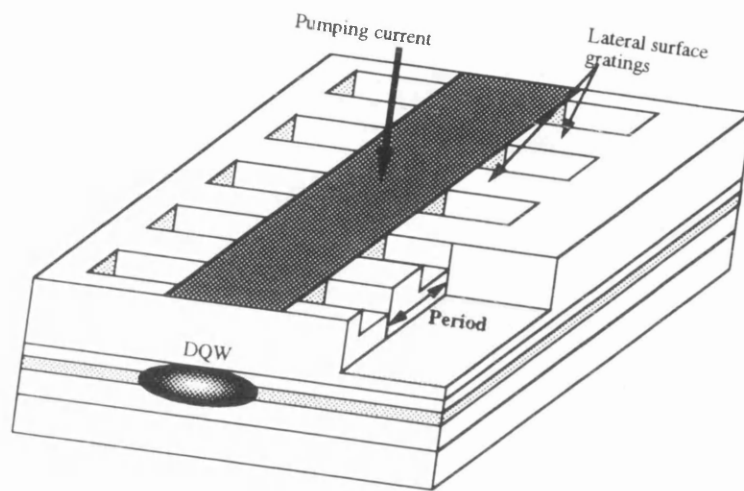
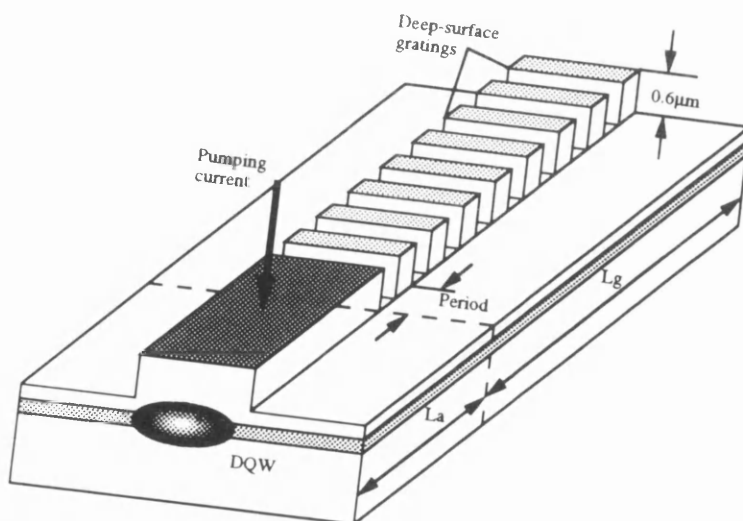


Fig.3-1. Schematic diagram of an extended (composite) cavity laser



(a)



(b)

Fig.3-2. Schematic diagrams of (a) a DFB, and (b) a DBR laser with deep surface gratings.

$\Gamma g_0$  can be obtained by using Eq. (3-4) from experiments on both disordered and nondisordered lasers with a range of different cavity lengths. Measured data for the threshold current as a function of the length of the passive section for extended cavity lasers were used in Eq. (3-5) to determine  $\alpha_p$  from a plot of  $\ln[I_{th}'/I_{tho}]$  vs  $(L_p / L_a)$ , with  $L_a$  fixed. It should be emphasized that this method has the advantage of estimating the gain constant-confinement factor product  $\Gamma g_0$  without introducing extra assumptions. The validity of this approach was confirmed by the fact that the experimental results, as shown in chapter 5, were in good agreement with the above theoretical treatment .

### 3-2-2 Lasing wavelength shifts

Many factors may affect the refractive index of a laser diode, which in turn will change the lasing wavelength. If a laser diode is maintained at a constant temperature, the wavelength shift due to temperature variation can be negligible. There are then two opposite effects arising from carrier injection. One is the bandgap narrowing effect, the other is the band-filling effect.

#### 1. Carrier-induced wavelength shifts

##### A. Bandgap narrowing effect

Many-body effects on carriers and carrier-LO phonon interaction are the primary reasons causing the red shift of a laser diode [4]. For a 3-D Fermi gas in GaAs at room temperature, the bandgap reduction  $\Delta E_g$  is given by [5]

$$\Delta E_g(\text{eV}) = -1.6 \cdot 10^{-8} (p^{1/3} + n^{1/3}) \quad (3-6)$$

where  $p$  and  $n$  are the hole and electron densities ( $\text{cm}^{-3}$ ) respectively. For a 2-D Fermi gas in GaAs at room temperature,  $\Delta E_g$  is given by [4]

$$\Delta E_g(\text{eV}) = -1.8 \cdot 10^{-8} (p^{1/2} + n^{1/2}) \quad (3-7)$$

where  $p$  and  $n$  are in units of  $\text{cm}^{-2}$ . For lower carrier densities, experimental results for  $\Delta E_g$  are close to Eq. (3-7). When the density is higher, the value of  $\Delta E_g$  approximates to Eq. (3-6), because the carriers will penetrate or spill over the QW barriers, and behave as a partially confined 3-D Fermi gas.

##### B. Band-filling effect

Photo-generated carriers from the valence band to the conduction band cause the

material absorption to be reduced because they result in a decrease in the number of unoccupied states available for carriers from further photoexcitation. This phenomenon is less significant in a 3-D system due to its continuous distribution of the density of states. On the other hand, as carrier injection increases, due to the constant density of states for the 2-D case, the quasi-Fermi levels will deepen into the conduction and valence bands faster than for the 3-D case. The corresponding absorption constant change  $\Delta\alpha(E)$  is given by [6]

$$\Delta\alpha(E) = \alpha_o(E)[f_v(E) - f_c(E) - 1] \quad (3-8)$$

where  $f_v(E)$  and  $f_c(E)$  are the Fermi-Dirac distribution functions in the valence and conduction bands respectively and  $\alpha_o(E)$  is the unperturbed absorption spectrum. Substituting (3-8) into the Kramers-Kronig Relationship, the change in refractive index from the band filling effect can be obtained.

According to [4], the lasing wavelengths from the first and the second sublevels of a GaAs QW diode are 852 nm and 800 nm respectively. When  $n < 3 \times 10^{18} \text{ cm}^{-3}$ , bandgap narrowing is more significant than band-filling, implying a red shift. When  $n > 3 \times 10^{18} \text{ cm}^{-3}$ , the situation is reversed, and the band-filling effect becomes the dominant one, resulting in a blue shift.

In addition to carrier-induced shifts, the wavelength shift from gain-loss competition of an extended-cavity structure also has an important effect on the lasing properties and will be discussed in the next section.

### *B. Wavelength shift due to gain-loss competition*

The absorption edge of the passive waveguide section will shift to a shorter wavelength, relative to that of active section, due to QW intermixing. Furthermore, the peak of the net gain for an extended-cavity structure depends strongly on the loss of the waveguide section, in addition to other internal losses, and on the gain of the active section. The actual gain-loss difference, i.e. the net gain, in the overlapping region of the gain curve and the absorption tail for the passive waveguide section will therefore determine the lasing wavelength of an extended-cavity structure.

A qualitative model of this lasing wavelength shift will be discussed further in chapter 5, together with experimental data.

## **3-3 DBR lasers**

### **3-3-1 Introduction**

DFB and DBR lasers provide longitudinal-mode selection based upon the distributed feedback effect. However, in contrast to DFB lasers, the gratings for DBR

lasers are situated outside of the active section. Effectively, a DBR laser can be taken as a Fabry-Perot laser the end mirror of which exhibits frequency-dependent reflectivity [7] and for which lasing occurs at or close to the wavelength where the reflectivity is maximum.

A problem inherent to the DBR laser is that when gratings are etched into the waveguide layers, optical losses inside the DBR region can be high and the resulting DBR reflectivity is poor [7, 8]. Therefore, a low-loss grating waveguide is crucial for a DBR laser in order to obtain high reflectivity and good mode selectivity.

### **3-3-2 Comparison between DBR and DFB lasers**

To understand the basic properties of DFB and DBR lasers, it would be easy from comparing their similarities and differences (diagrams shown in Fig.3-2). For a DBR laser, gratings are situated in a separate passive section. This situation not only provides better wavelength tunability (see section 3-4), but also avoids the nonradiative recombination introduced by grating-etch defects in the pumping section like that in a conventional DFB laser.

Since DFB lasers operate (ideally) without facet mirrors, the resonant-mode characteristics are symmetric with respect to the Bragg wavelength, so that longitudinal modes with the same minimum threshold gain exist in pairs on both sides of the Bragg wavelength. In this symmetric case, the lasing oscillation at the Bragg wavelength is essentially forbidden unless a phase adjustment design is used [9, 10].

On the other hand, for DBR lasers, the resonant-mode characteristics determined by the phase shifts of the active and passive DBR regions are usually asymmetric. The deviation of the lasing wavelength from the Bragg wavelength is changed by adjusting the length of active region. Therefore, if the phase shift of the active section is properly controlled, the lasing wavelength can be (nearly) matched to the Bragg wavelength [8].

The coupling coefficient of a DFB laser with exterior third-order gratings described above typically ranges from 5 to 15  $\text{cm}^{-1}$  [11]. From our experimental observations (in chapter 6) and other researchers' results [12], for a DBR laser with gratings situated on one side only of the pumping region, a coupling coefficient of 100  $\text{cm}^{-1}$  can be easily achieved.

### **3-3-3 Key parameters of a DBR laser**

Coupled-wave theory [13, 14] is a useful tool to realize and analyze the properties of a DFB or a DBR laser. To facilitate later discussions, this theory will be briefly discussed in this section.

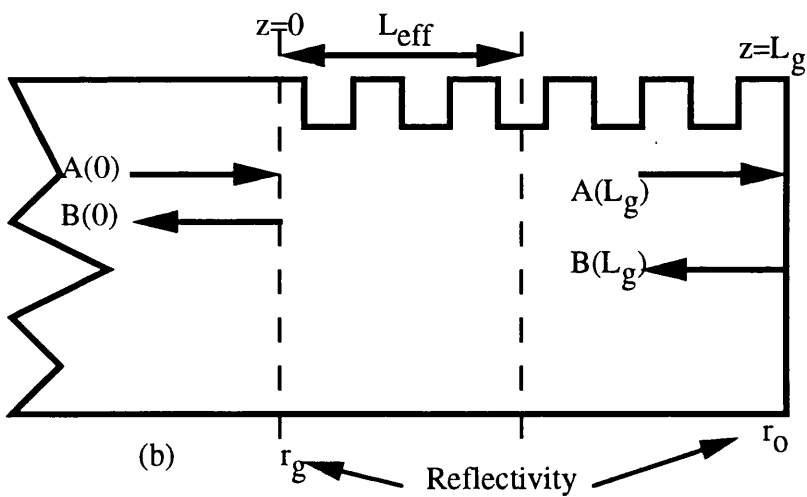
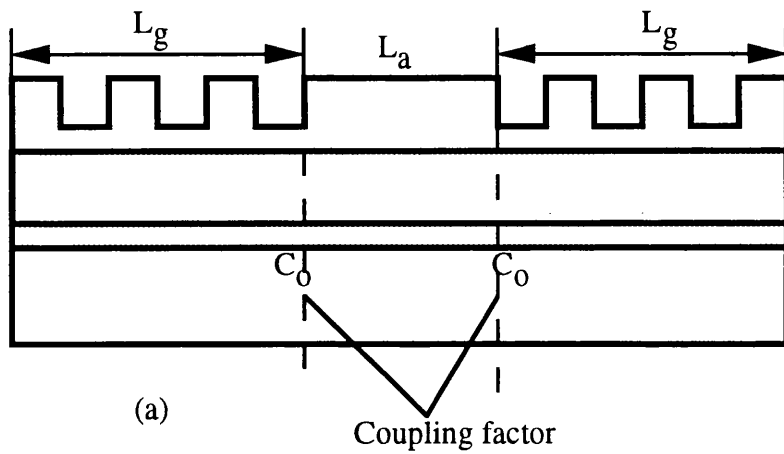


Fig.3-3. (a) Schematic diagram of a DBR laser with double-sided gratings  
 (b) Counter-running waves in DBR gratings

From electromagnetism, the fundamental wave equation for an electric field  $E$  is given by

$$\nabla^2 E + K^2 E = 0 \quad (3-9)$$

with  $K^2 = K_o^2 n^2 - jK_o n \alpha_g$

where  $K_o \equiv 2\pi / \lambda$  is the vacuum wave number,  $\alpha_g$  is the absorption coefficient, and  $n$  is the refractive index of the waveguide. The refractive index of a corrugated periodic structure, as shown in Fig.3-3, can be expressed by

$$n^2(x, z) = n_o^2 + \Delta n^2(x, z) \quad (3-10)$$

where  $n_o$  is the refractive index of the waveguide without corrugations, and  $\Delta n$  is the index variation generated from a corrugated perturbation. According to the coupled-wave theory, the forward and the backward propagating waves in the  $z$  direction couple with each other. The resultant electric field of these guided waves  $E(x, z)$  is

$$E(x, z) = [A(z)e^{-j\beta_o z} + B(z)e^{j\beta_o z}]E_x(x) \quad (3-11)$$

where  $\beta_o = m\pi / \Lambda$  is for the  $m$ th order of the Bragg reflection,  $\Lambda$  is the period of corrugations, and  $A(z)$  and  $B(z)$  are the amplitudes of the forward and the backward propagating waves respectively. Applying (3-10) and (3-11) to the first-order approximation of (3-9), the coupled-wave equations [7] become:

$$\begin{aligned} \frac{dA}{dz} &= j\Delta\beta A + j\kappa B \\ -\frac{dB}{dz} &= j\Delta\beta B + j\kappa A \end{aligned} \quad (3-12)$$

where  $\Delta\beta = \beta - \beta_o$  is the deviation of the propagation constant  $\beta$  from the Bragg wavelength, and  $\kappa$  is the coupling coefficient between the propagating waves  $A(z)$  and  $B(z)$ , which is given by

$$\kappa = \frac{K_o^2}{2\beta N^2} \int_{\text{corrugation}} \Delta n^2(x, z) E_x^2(x) dx \quad (3-13)$$

with  $N^2 \equiv \int_{-\infty}^{\infty} E_x^2(x) dx$

A general solution of (3-12) has the form

$$\begin{aligned} A(z) &= A_1 \exp(iqz) + A_2 \exp(-iqz) \\ B(z) &= B_1 \exp(iqz) + B_2 \exp(-iqz) \end{aligned} \quad (3-14)$$

Substituting Eq. (3-14) into Eq. (3-12) with boundary conditions, constants  $A$  and  $B$  can then be obtained. In the formulas above  $q = \pm[\Delta\beta^2 - \kappa^2]^{1/2}$ ,  $\delta = -\frac{2\pi n_{ge}}{\lambda^2} \Delta\lambda$ ,  $\Delta\beta = \delta + j(\alpha_g / 2)$ ,  $\Delta\lambda = \lambda - \lambda_B$  is the wavelength detuning and  $n_{ge}$  is effective refractive index of the grating waveguide.

#### A. Bragg reflectivity

The complex amplitude reflectivity  $r_g$  of a Bragg reflector can be expressed by [7]

$$\begin{aligned} r_g &= \frac{B(0)}{A(0)} = \frac{B_2 + r(q)A_1}{A_1 + r(q)B_2} \\ &= \frac{j\kappa \sin(qL_g)}{q \cos(qL_g) - j\Delta\beta \sin(qL_g)} \\ &\equiv |r_g| \exp(j\Phi) \end{aligned} \quad (3-15)$$

where  $\Phi$  is the phase of  $r_g$ . From Eq. (3-15), it is obvious that the Bragg reflectivity depends on the coupling coefficient, grating length, grating loss and effective refractive index, in addition to the lasing wavelength and its detuning.

#### B. Effective grating length $L_{eff}$

Since the phase shift  $\Phi$  of a Bragg reflector is approximately a linear function of  $\Delta\beta$  around the Bragg wavelength [15], the effective length of a DBR can be defined as [16]

$$\exp[j\partial\Phi / \partial\lambda(\lambda - \lambda_B)] \equiv \exp(-2j\Delta\beta L_{eff}) \quad (3-16)$$

and  $L_{eff}$  can be obtained from Eq. (3-15) and Eq. (3-16):

$$L_{eff} = \tanh(\kappa L_g) / (2\kappa) \quad (\text{for } \lambda \approx \lambda_B) \quad (3-17)$$

$L_{eff}$  is useful for analyzing the approximate lasing condition and dynamic properties of a DBR laser. By using it, the cavity will act like a Fabry-Perot cavity with the wavelength-dependent Bragg mirror reflectivity at the Bragg peak, and a total

cavity length equivalent to  $L_t = L_a + L_{eff}$ , where  $L_a$  is the length of the active (gain) section. This will immediately yield a mode spacing (*at the Bragg peak*) expressed by

$$\Delta\lambda_m = \frac{\lambda^2}{2n_{ge}L_t} = \frac{\lambda^2}{2n_{ge}\left[L_a + \frac{\tanh(\kappa L_g)}{2\kappa}\right]} \quad (3-18)$$

Therefore, the coupling coefficient  $\kappa$  can be estimated by measuring mode spacing, typically 0.21 nm for the DBR lasers in this work, from a spontaneous-emission spectrum, which will be demonstrated later in chapter 6.

In contrast to FP lasers, however, the modes are not equally spaced since  $\Phi$  depends on the detuning wavelength of the mode from the Bragg wavelength.

### C. Coupling factor and DBR loss

Threshold conditions for a DBR laser are given by [7]

$$C_o^2 |r_g|^2 \exp(\alpha_{net} L_t) = 1 \quad (3-19a)$$

$$n_e K_o L_t + \Phi = m\pi \quad (3-19b)$$

where  $C_o$  is the field amplitude coupling coefficient factor between the active and the passive sections,  $\alpha_{net} = \Gamma g - \alpha_i$  is the net optical gain,  $\alpha_i$  is the total internal loss, and  $n_e$  is the effective modal refractive index.  $C_o$  is defined by [17]

$$C_o = \int_{-\infty}^{\infty} E_a^0(x) E_p^0(x) dx$$

where  $E_a^0(x)$ ,  $E_p^0(x)$  are the lowest - order confined modes in the active section and the passive section respectively. Due to the corrugated perturbation, the modal distributions in the active and the passive sections should be different, so  $C_o$  is generally less than unity. It would be small if the discontinuity at the active-passive interface, i.e. waveguide step, is high or if the effective refractive-index difference at the interface is large.

Just as for an F-P laser, the DBR mirror loss is given by:

$$\alpha_g = \frac{1}{L_t} \ln \left[ \frac{1}{C_o^2 r_g^2} \right] \quad (3-20)$$

For a DBR laser with gratings situated on one side of the pumping section, Eq.(3-20) can be simplified further to:

$$\alpha_g = \frac{1}{L_t} \ln \left[ \frac{1}{C_o r_g \sqrt{R_f}} \right] \quad (3-21)$$

where  $R_f$  is the power reflectivity of the crystal facet. Note that the DBR loss  $\alpha_g$  is strongly related to the effective Bragg reflectivity,  $C_o r_g$ , as expected.

### 3-4 Design considerations of a DBR laser

From the viewpoint of laser-linewidth improvement [19], the cavity length should be increased and cavity absorption and scattering losses need to be decreased. For the operation of a DBR laser diode, the power coupling coefficient - grating length product (i.e. coupling strength),  $\kappa L_g$ , is a crucial factor which affects the laser performance.

If  $\kappa L_g$  is too large ( $\gg 2$ ), most light will be reflected back and forth in the cavity, hence (external) quantum efficiency suffers. On the other hand, if  $\kappa L_g$  is too small ( $< 1$ ), the threshold gain and the linewidth would increase.

The requirement of having a single longitudinal mode restricts the intermode spacing  $\Delta \lambda_m$  to be equal to or greater than the Bragg reflectivity bandwidth. Koch et al. [16] have suggested that  $\kappa L_g$  should be in the range of  $2.18 < \kappa L_g < 3.74$ . However, Soda et al. [19] recommended that  $\kappa L_g = 1.25$  in order to exempt from the two-mode emission and to maintain a large threshold gain difference above threshold. An AT & T research group [1] used  $\kappa L_g = 1.8$ , with  $L_a = 225 \mu\text{m}$  and  $L_g = 360 \mu\text{m}$ , and achieved a record-high side mode suppression ratio (SMSR) of 58.5 dB.

Although the suggestions above seem diverse, the solution of getting a high-performance single-moded DBR laser is to use "long and weak gratings" [1]. In order not to induce multimode operation, the length of active section should be short, and the grating length must be sufficiently large [1]. For instance, if the coupling coefficient is 50, the combination of  $L_a = 250 \mu\text{m}$  and  $L_p < 400 \mu\text{m}$  will meet the above criteria. This criterion will be used as the fabrication guideline in this work.

### 3-5 Tunability

A suitable form of tuning is required for optical communication systems to align the transmitter and local oscillator lasers for heterodyne or homodyne detection. To achieve the required tuning, it is important to rearrange the gain margins of the various cavity modes or to shift the wavelength of the DBR mode towards or away from the gain peak of the laser spectrum. Compared to a DFB laser, the DBR laser is easier to tune separately from the pumping region, and the tuning characteristics are more predictable [8].

Two tuning methods, which have been frequently mentioned in the literature [16, 19], are briefly introduced here:

#### *A. Temperature tuning*

It is well known that the laser emission of a F-P laser follows the temperature dependence of the energy gap, while the lasing wavelength of the DFB/DBR laser follows the smaller temperature dependence of the refractive index [20]. Typically, the tuning coefficients are 0.5 nm/°K for the FP mode ( i.e. gain peak ) and 0.06-0.08 nm/°K[8] for the DBR mode respectively. Temperature tuning can be achieved by adjusting the lasing wavelength and hence the threshold current, so it is particularly useful for DBR laser tuning. There are two possible cases:

(1)First, if the wavelength of the DBR lasing mode is smaller than the wavelength of the gain peak, the gain peak will move away from the lasing wavelength peak during temperature increases (Fig.3-4(a)). This will drive the threshold current higher when the temperature is increased and can often be found during a diode test.

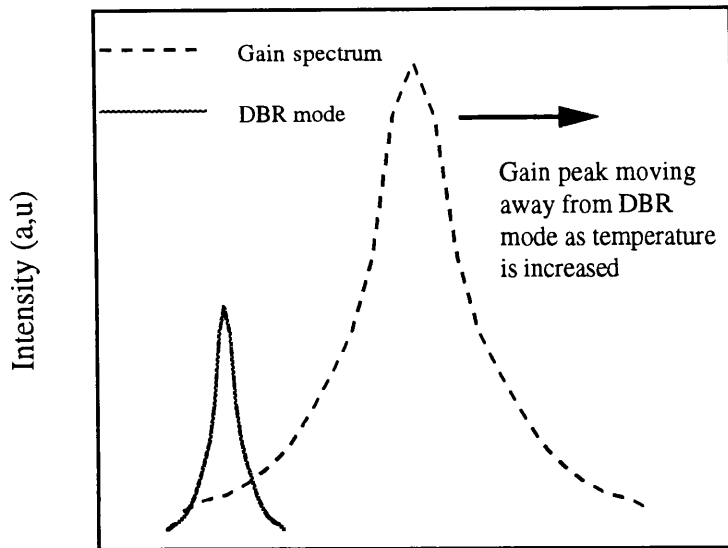
(2)Second, if the lasing wavelength is greater than the gain peak, the peak will move toward the DBR mode when the temperature is increased (Fig.3-4(b)). Simultaneously, the laser gain would decrease as the temperature is increased. In this case, two opposite mechanisms competes. If the DBR mode could obtain sufficiently large gain, due to better matching of the gain peak and Bragg wavelength, to overcome the increase of the threshold current with temperature, a decrease in threshold current with increasing temperature can be observed [21].

#### *B. Current tuning*

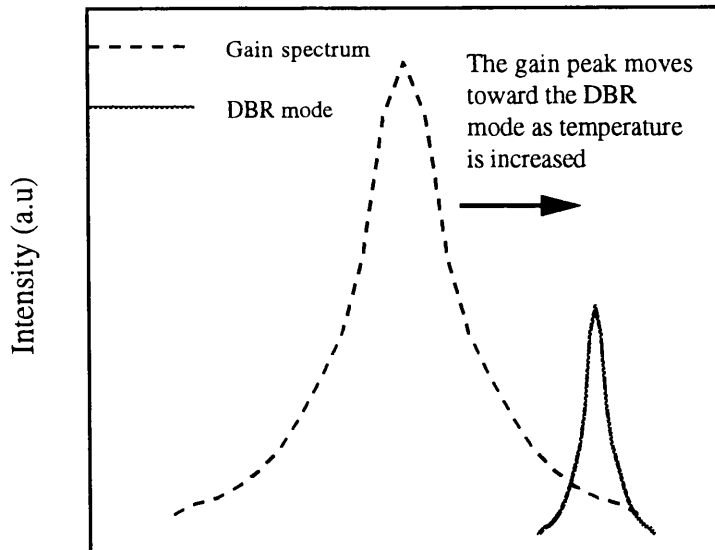
A multi-section DBR laser has the advantage of providing monolithic integration of the various optical cavity elements. It not only has the potential of stable and efficient coupling, but also affords the convenient way to tune the laser for system requirements.

Forward injection into a double heterostructure with lasing frequency below the bandgap of the active layer is usually used for current tuning. Since the Bragg reflectivity profile is a function of  $\beta = 2\pi n_g / \lambda$ , a change in the grating index,  $\Delta n_g$ , would yield a wavelength shift in the peak of the reflectivity profile, and tune the DBR lasing mode.

It has been found that if the change of a DBR lasing mode is performed at the same time as the peak of the Bragg reflection is shifted, the continuous-tuning range can be considerably larger than one F-P mode spacing[16]. Compared to the 2-3 nm temperature tuning range, a continuous current tuning range of over 10 nm can be easily achieved for the DBR laser [22].



(a)



(b)

Fig.3-4. Two possible temperature ( $T$ ) tuning conditions:  
 (a) The gain peak moves away from the DBR mode as  $T$  increases, which in turn increases the threshold current  $I_{th}$ .  
 (b) The gain peak moves toward the DBR mode as  $T$  increases, and the threshold current  $I_{th}$  is thus reduced.

### 3-6 Summary

In this chapter, two device theories were introduced and discussed. For the extended-cavity laser, a theoretical model was derived for the analysis of the effect of the passive-section length on the propagation losses in the passive section. The lasing wavelength shifts, due to carrier injection and gain-loss competition, of a composite-cavity structure were also described.

For the DBR laser, comparisons with a DFB laser were described. Fundamental formulae were described for future reference. Key parameters of a DBR laser were derived and depicted. It was found that the effective Bragg reflectivity of a DBR laser depends on many factors, such as active-to-passive power coupling factor, grating losses, detuning, and coupling strength  $\kappa L_g$ . Care should be taken to control these factors affecting the DBR laser performance.

The availability and importance of the wavelength tuning for a DBR laser were finally discussed in this chapter.

### 3-7 Appendix

#### A. Laser linewidth

The laser linewidth is defined as the full width of half maximum (FWHM) of the Lorentzian-shaped spectral density function of the laser field. It is given by [23]

$$(\Delta\nu)_{laser} = \frac{2\pi h\nu(\Delta\nu)_{cavity}^2 n_{sp}}{P} + R \quad (a)$$

where  $(\Delta\nu)_{laser}$  is the laser linewidth,  $(\Delta\nu)_{cavity}$  is the cavity linewidth (defined below),  $n_{sp}$  is the spontaneous emission factor defined as the ratio of the spontaneous emission rate to the stimulated emission rate,  $P$  is the laser output, and  $R$  is the residual linewidth when output power goes to infinity.

#### B. Cavity linewidth

The photon loss  $\alpha_t$  is defined as the effective fraction loss of optical power per unit length of the cavity [24]:

$$\begin{aligned} \alpha_t &= \frac{(-dP / P)}{dz} = \frac{-1}{P} \frac{dP}{dz} \\ &= \alpha_i + \alpha_m \end{aligned} \quad (b)$$

where  $\alpha_i$  is the internal loss and  $\alpha_m$  is the mirror loss of the laser.

The photon lifetime is defined as

$$\frac{1}{\tau_{ph}} = \frac{-1}{P} \frac{dP}{dt} \quad (c)$$

For a plane wave,  $z-vt = \text{constant}$ , where  $v$  is the phase velocity of light and  $z$  is the position of the wavefront.  $(dz/dt) = v = (c/n_p)$  and  $n_p$  is the phase refractive index.

$$\begin{aligned} \frac{1}{\tau_{ph}} &= -\frac{1}{P} \frac{dP}{dz} \frac{dz}{dt} \\ &= \alpha_i \left( \frac{c}{n_p} \right) \end{aligned} \quad (d)$$

The cavity linewidth  $(\Delta\nu)_{cavity}$  is defined by [23]

$$\begin{aligned} \Delta\nu_{cavity} &= \frac{1}{2\pi\tau_{ph}} \\ &= \frac{c}{2\pi n_p} (\alpha_i + \alpha_m) \end{aligned} \quad (e)$$

$$= \frac{c}{2\pi n_p} \left[ \frac{\alpha_a L_a + \alpha_p L_p}{L_a + L_p} + \frac{1}{L_a + L_p} \frac{1}{\ln(R_1 R_2)^{1/2}} \right] \quad (f)$$

The first term of the above equation is contributed from the average of the internal loss, where  $\alpha_{a,p}$  and  $L_{a,p}$  are the loss and the length of the active (or passive) section respectively. The second term is due to the mirror loss, in which  $R_1$  and  $R_2$  are the facet reflectivities.

### 3-8 References

- [1] F.S.Choa, W.T. Tsang, R.A.Logan, R P Gnall, U Koren, T L Koch, C A Burrus, M C Wu, Y K Chen, P F Sciortino, A M Sergent and P J Corvini, 'Very High Sidelobe-Suppression- Ratio Distributed-Bragg-Reflector Lasers Grown by Chemical Beam Epitaxy', pp.1001-1002, V-28, No.11, Electron Lett., 1992
- [2] P.W.A.McIlroy, A.Kurobe, and Y.Uematsu, 'Analysis and application of theoretical gain curves to the design of multi-quantum-well lasers', V-21, No.12, pp.1958-1963, IEEE J. Quantum Electron. 1985.
- [3] J.Werner, E. Kapon, N.G. Stoffel, E. Colas, S.A.Schwarz, C.L.Schwartz, and N. Andreadakis, 'Integrated external cavity GaAs/AlGaAs lasers using selective quantum well disordering', 55(6), pp.540-542, Applied

Phys.Lett., 1989.

- [4] A.Tomita, and A.Suzuki, 'Carrier-induced lasing wavelength shift for quantum well laser diodes', V-23, No.7, pp.1155-1159, IEEE J. Quantum Electron. 1987.
- [5] H.C.Casey and M.B.Panish, '*Heterostructure Lasers*', Part A, section 3- 7, Academic Press, New York, 1978.
- [6] R.V. Penty, ' Picosecond Optical Switching Using Near Bandedge Nonlinearities in Semiconductor Waveguides', 6/1, IEE Colloquium on "Ultra-Short Optical Pulses", Nov., 1993.
- [7] G.P.Agrawal and N.K.Dutta, '*Long-Wavelength Semiconductor Lasers*', p.184, Van Nostrand Reinhold, New York, 1986
- [8] W.T.Tsang, '*Semiconductors and Semimetals*', chapter 4, Academic Press, New York V-21, 1985.
- [9] S.L.McCall and P.M.Platzman, 'An optimized  $\pi / 2$  Distributed Feedback Laser ', V-21, No.12, pp.1899-1904, J. of Quantum Electron., 1985.
- [10] J.E.A.Whiteaway, G H B Thompson, A J Collar and C J Armistead, 'The Design and Assessment of  $\lambda / 4$  Phase-Shifted DFB laser structures', V-25, No.6, pp.1261-1279, J. of Quantum Electron , 1989.
- [11] H. Abe, Master thesis, Glasgow University, 1994.
- [12] D.Hofstetter, H.P. Zappe, J.E.Epler and J. Söchtig, ' Single-growth Step GaAs/AlGaAs Distributed Bragg Reflector Lasers with holographically-defined recessed gratings ',V.30, No.22, Electron.Lett., 1994.
- [13] H.Kogelnik and C.V.Shank, 'Coupled-Wave theory of Distributed Feedback Lasers', pp.2327-2335, V.43, No.5, J Appl. Physics, 1972.
- [14] A. Yariv and M. Nakamura, 'Periodic Structures for Integrated Optics', pp.233-253, V.13, No.4, IEEE J. Quantum Electron., 1977.
- [15] Y.Suematsu, S.Arai and K.Kishino, 'Dynamic Single-Mode Semiconductor Lasers with a Distributed Reflector', pp.161-175,V-1,J Lightwave Tech.,1983.
- [16] T.L.Koch and U.Koren, 'Semoconductor Lasers for Coherent Optical Fiber Communications', pp.274-293, V-8, No.3, J Lightwave Tech., 1990.
- [17] H.M.Stoll, 'Optimally Coupled, GaAs-Distributed Bragg Reflection Lasers',V-26, No.12, IEEE Tran. on Circuits and Systems, 1979.
- [18] A.Yariv, '*Introducción to Optical Electronics*', 3rd edition, John Wiley, New York, 1985.
- [19] H.Soda, Y.Kotaki, H.Sudo, H.Ishikawa, S.Yamakoshi and H.Imagi,

'Stability in Single Longitudinal Mode Operation in GaInAsP/ InP Phase-Adjusted Distributed Feedback Lasers', pp.804-814, V-23, No.6, J Quantum Electron., 1987.

[20] H.C.Casey and M.B.Panish, '*Heterostructure Lasers*', Part B. section 7-12, Academic Press, New York, 1978.

[21] G.Hasnain, K.Tai, L.Yang, Y.H.Wang, R.J.Fischer, J.D.Wynn, B.Weir, N.K.Dutta and A.Y.Cho, 'Performance of Gain-Guiding Surface Emitting Lasers with Semiconductor Distributed Bragg Reflectors ', pp.1377-1384, V-27, No.6, J Quantum Electron, 1991.

[22] L.A.Coldren and S.W Corzine, 'Continuously-Tunable Single-Frequency Semiconductor Lasers ', pp.903-908; V-23, No.6, J. Quantum Electron., 1987.

[23] A.Yariv, '*Optical Electronics*', section 10-7, 3<sup>rd</sup> edition, Wiley, New York,1984.

[24] J.Gowar, '*Optical Communication System*', p.342-343, Prentice-Hall, London, 1985

## Chapter 4 Impurity free vacancy diffusion

### 4-1 Introduction

Quantum-well (QW) intermixing techniques have been proposed for applications in OEICs. By using this technique, the so-called "window section" can be obtained, which has a wider bandgap to allow more photons to be transmitted after QW intermixing than in the original QW structure. The propagation loss can be effectively reduced considerably by a blue shift of the absorption edge, if a proper process is selected. Recent work in the Optoelectronics Research Group in Glasgow University has led to progress in three different QW disordering processes. These are Impurity-Induced Disordering (IID) [1,2,3], Impurity Free Vacancy Diffusion (IFVD) [4,5,6], and Photo-Absorption (laser) Induced disordering (PAID) [7]. The last technique was developed recently and involves intermixing initiated by laser annealing.

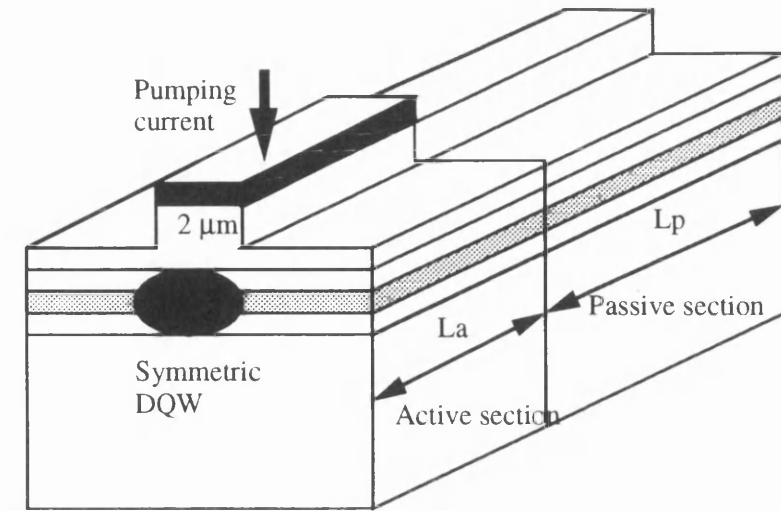
IID is probably the most developed and reproducible technique among these three. In order to avoid generating too many free carriers and consequent free-carrier absorption, impurities which are at room temperature electrically-active, such as Si and Zn, should be avoided. Since fluorine-implanted (a neutral impurity) MQW structures have a larger blue-shift (up to 100 meV)[8], producing a lower-loss waveguide, compared to that for boron implantation, fluorine is the better neutral impurity to be considered for this application.

Instead of IID, the IFVD technique has been used for the QW disordering in this work. A low-temperature photoluminescence (PL) measurement is generally required to measure the bandgap shift after a sample has been disordered in a rapid thermal annealer (RTA). The photocurrent response can further serve as a complementary tool to gain further insight into the disordering process. The important roles of native oxide and the oxide-on-GaAs system for the disordering process are described in detail below since achievement of satisfactory result depends strongly on them.

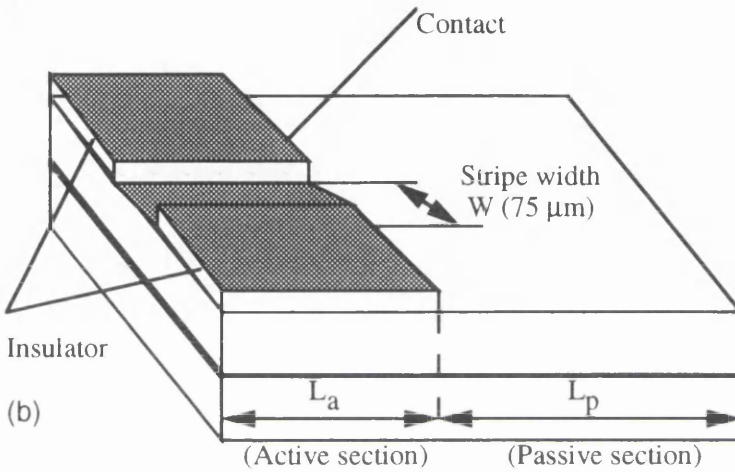
### 4-2 Disordering mechanism of IFVD

It is well known that a laser with an extended cavity ( Fig.4-1) can have greatly reduced linewidth and IFVD can be used as an effective tool to reduce the waveguide loss for such a laser [6].

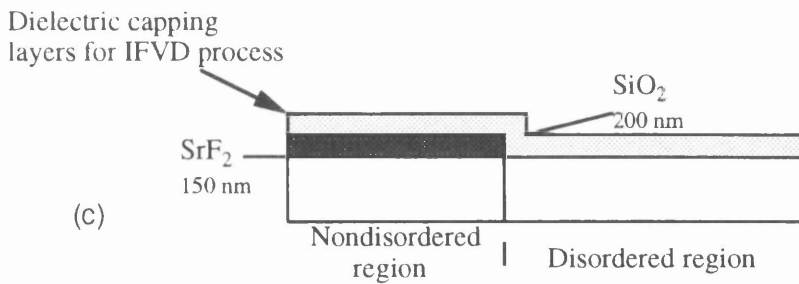
For a conventional quantum-well laser with an extended passive section, any blue shift of its lasing wavelength, caused by the band-filling effect, would rapidly increase absorption losses in the passive section due to the proximity of the band



(a)



(b)



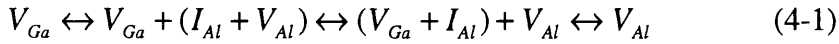
(c)

Fig.4-1. Schematic diagrams of an extended-cavity (a) ridge waveguide, (b) oxide stripe laser. (c) The dielectric capping layers for the IFVD process.

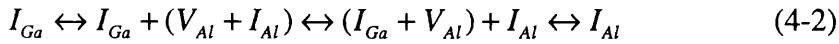
edges[2].

In order to blue-shift the absorption edge of the passive waveguide section, IFVD was used. Fig.4-1 shows the extended cavity structure used for QW intermixing with selective dielectric capping layers of strontium fluoride and silicon dioxide.

Although the full details of the IFVD disordering mechanism are not well-understood, it is believed that the model proposed by Deppe et al [4] is a good approach to understand the microscopic mechanism of this intermixing process. According to this model, there are two equations governing the Al-Ga interdiffusion and layer intermixing. Either type of point defects can lead to group III self-diffusion through a similar reaction:



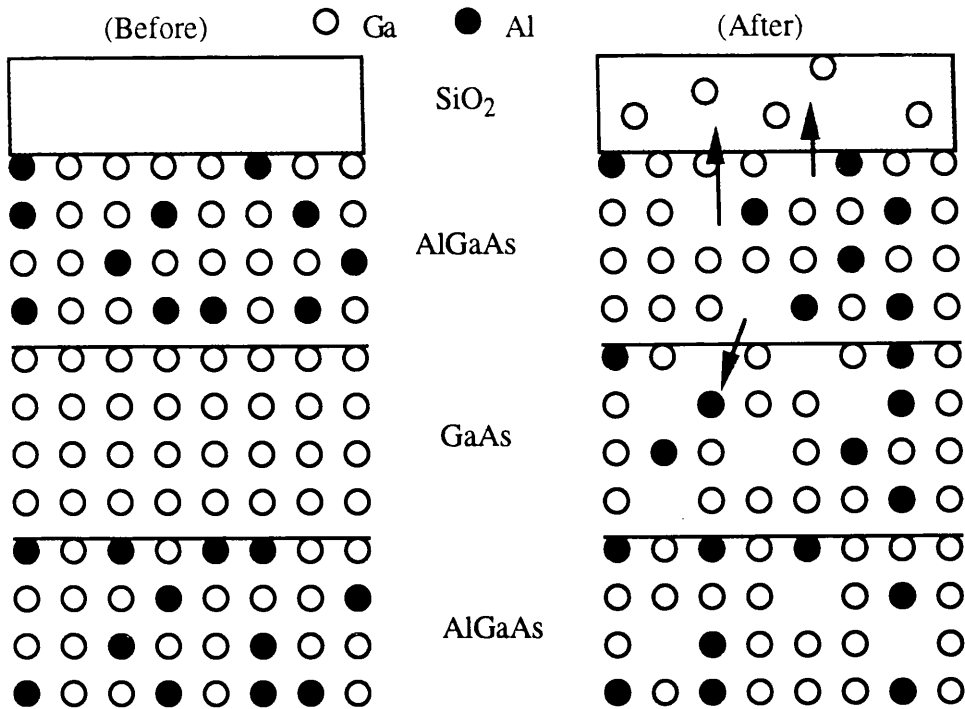
or



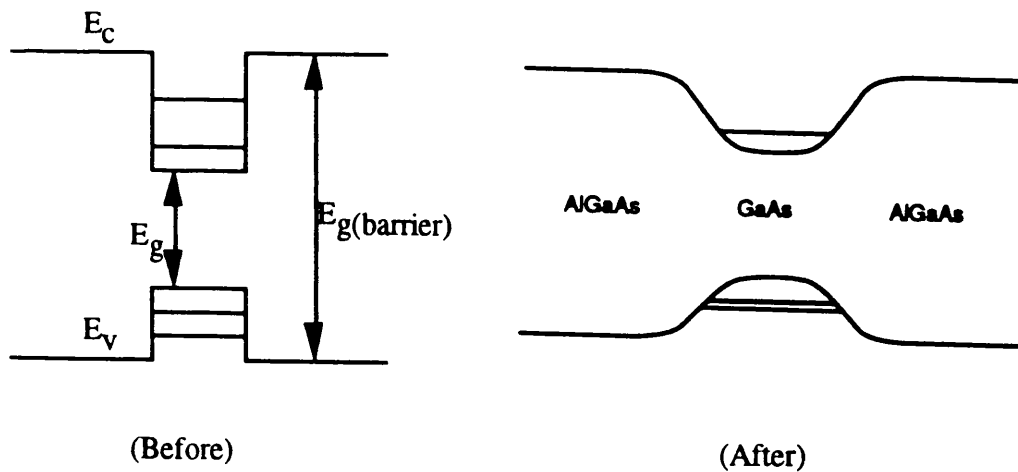
where V and I denote the vacancy-type and interstitial-type point defects respectively,  $(I_{Al} + V_{Al})$  is the Frenkel pair for Al lattice atoms on the column III sublattice, and  $I_{Al}$  and  $V_{Al}$  are the interstitial and vacancy defects originating from Al atoms respectively. The above equations clearly show how the group III Frenkel pair can be replaced and how to promote Ga-Al interdiffusion rate through either vacancy or interstitial medium.

However, the above layer intermixing would be influenced by many variables. Deppe et. al [4] showed that the layer interdiffusion in AlGaAs-GaAs superlattices will be enhanced under high As vapor pressure annealing conditions for a strongly n-type crystal or under low As pressure for a strongly p-type crystal. The amount of QW intermixing would be a function of the distance between the QWs and the GaAs surface and the induced bandgap shift also depends on the thickness of the SiO<sub>2</sub> capping layer [10]. Additionally, the native or As antisite defects may also affect Ga-Al interdiffusion rate.

Fig.4-2 (a) demonstrates the interdiffusion of group III atoms or vacancies in a AlGaAs-GaAs superlattice. Rapid thermal annealing (RTA) of GaAs/AlGaAs heterostructures at elevated temperatures causes the gallium atoms to out-diffuse into the silica capping layer (see Fig.4-2(a)). This generates a great number of vacancies on the group-III sites which subsequently diffuse into the substrate, allowing some aluminium atoms in the AlGaAs barrier to migrate into GaAs quantum wells. However, the active section under the strontium fluoride capping layer experiences only a negligible amount of Ga out-diffusion, thus providing very good suppression of the bandgap shift. After rapid thermal annealing, the change in energy from abrupt (square as-grown) interfaces to gradual (complementary error function) interfaces [9,10]



(a)



(b)

Fig.4-2. (a)Schematic diagram of an IFVD disordering process  
 (b)Energy band diagrams before and after an IFVD disordering process

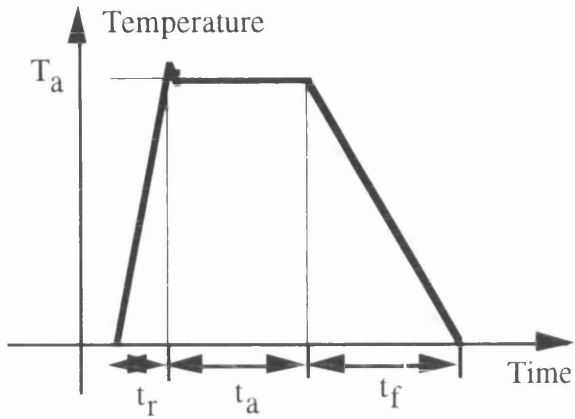


Fig.4-3. The RTA cycle for the IFVD process

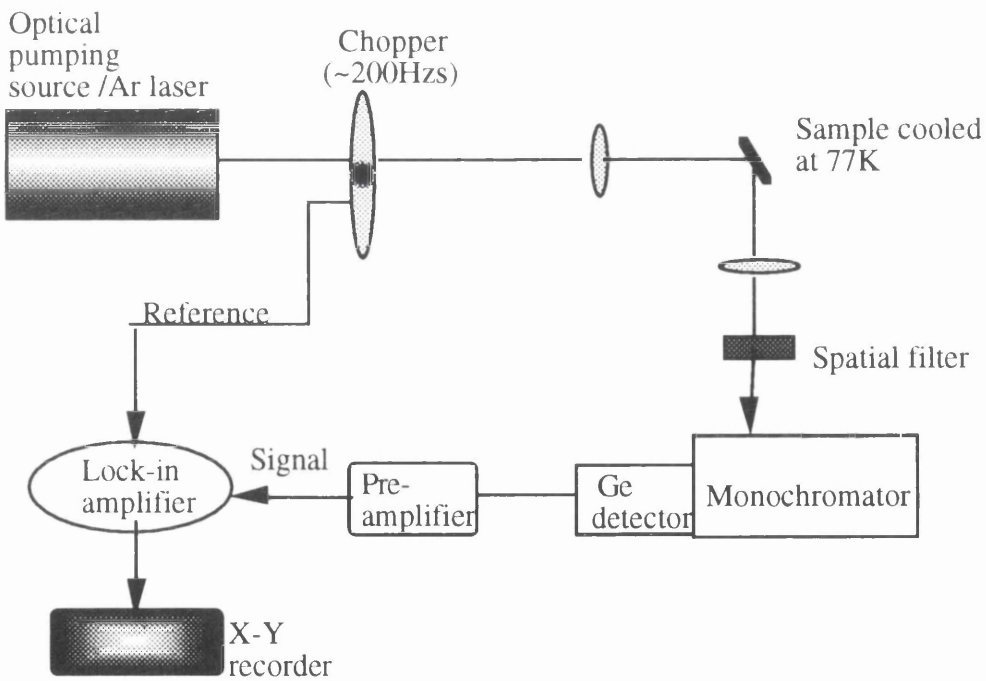


Fig.4-4 The experimental setup for a PL measurement

increases the energies of the quantized electronic levels of double quantum wells (Fig.4-2(b)). The magnitude of these energy increases depends strongly on the widths of the QW's, the annealing temperature and time and, most importantly, on the density of vacancies available [10] in this sample.

It has been observed [5] that a large relative blue shift can be achieved through promoting gallium out-diffusion in the silicon dioxide layer and suppressing Ga out-diffusion in the strontium fluoride layer. Furthermore, quantum well intermixing by dielectric cap disordering allows large bandgap shifts in quantum well devices without introducing impurities into the active region of the structure [8]. Losses introduced by non-radiative recombination centres or by free carriers, as in IID, are therefore effectively reduced.

### **4-3 Rapid thermal annealing (RTA)**

For a SiO<sub>2</sub>-on-GaAs system, the thermal expansion coefficient of GaAs is fourteen times that of SiO<sub>2</sub> [11]. When it is heated up, SiO<sub>2</sub> will experience a compressive stress, since it expands less than GaAs does. On the other hand, SiO<sub>2</sub> deposited at elevated temperature will suffer from a tensile stress as it is cooled down, because it shrinks less than GaAs does.

It has been shown [11] that the compressive stress will be partly released by atomic (Ga or As for this case) out-diffusion as the temperature rises, hence vacancies will be induced in the crystal lattice and QW disordering continues after RTA annealing. On the other hand, the tensile stress in the cooling period of an RTA cycle can relax through yielding of thin films. This is why the rise time, in addition to the anneal time, in the annealing cycle, is so important to the disordering result.

The rapid thermal annealer, model JIPELEC FAV4, was used in this work. During the annealing, samples are placed face down on a piece of GaAs to provide proximity capping. Another piece of GaAs cap is placed on the back of the samples. A silicon susceptor is situated underneath the samples and equipped with a pyrometer temperature sensor. Typically, the rise time,  $t_r$ , and fall time,  $t_f$ , are set to be 15 and 30 seconds respectively. The anneal time  $t_a$  ranges from 30 to 60 seconds and the appropriate anneal temperature ranges from 900 to 950° C, depending on the required bandgap shift for the device fabrication. The RTA cycle for an IFVD disordering process is shown in Fig.4-3.

### **4.4 Photoluminescence (PL) measurement**

Among optical characterization techniques, PL measurement is one of the most widely used in characterizing compound semiconductors and their alloys. It is employed both to understand the fundamental recombination processes in the

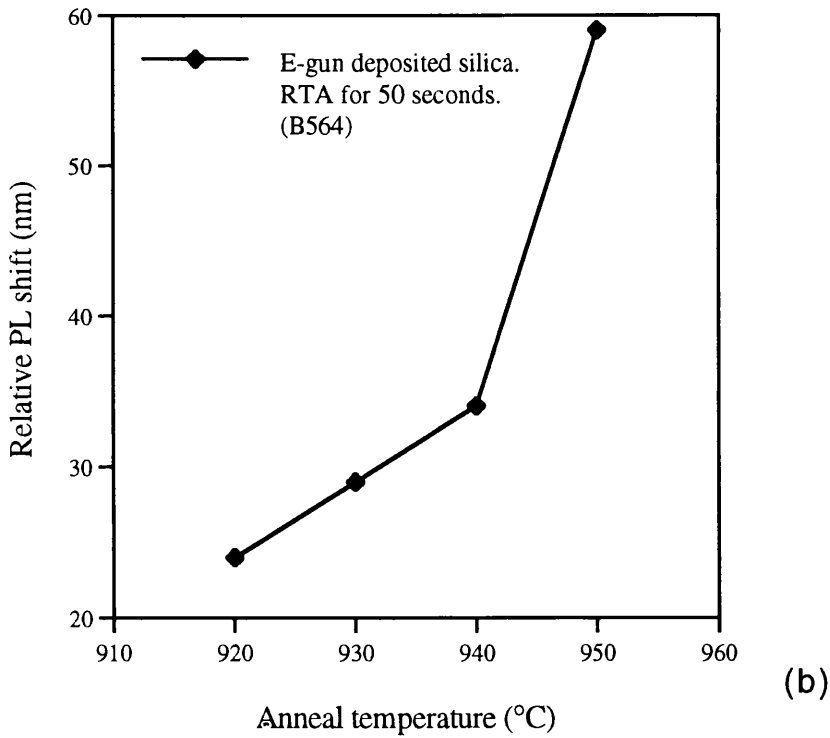
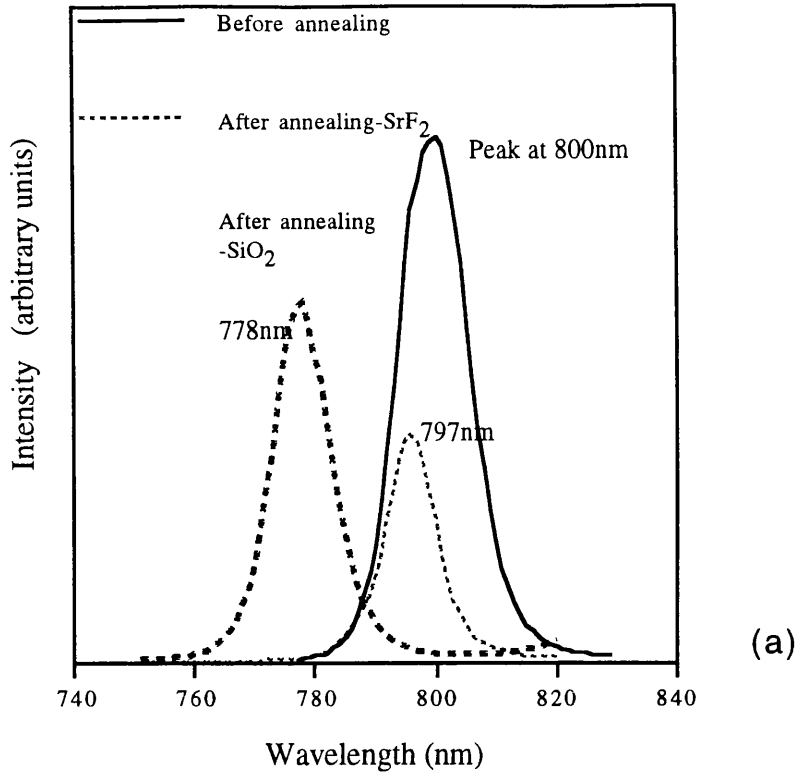


Fig.4-5(a) A typical PL-shift measurement for the IFVD process.  
 (b) The relative PL shifts as a function of anneal temperatures for the samples annealed for 50 seconds.

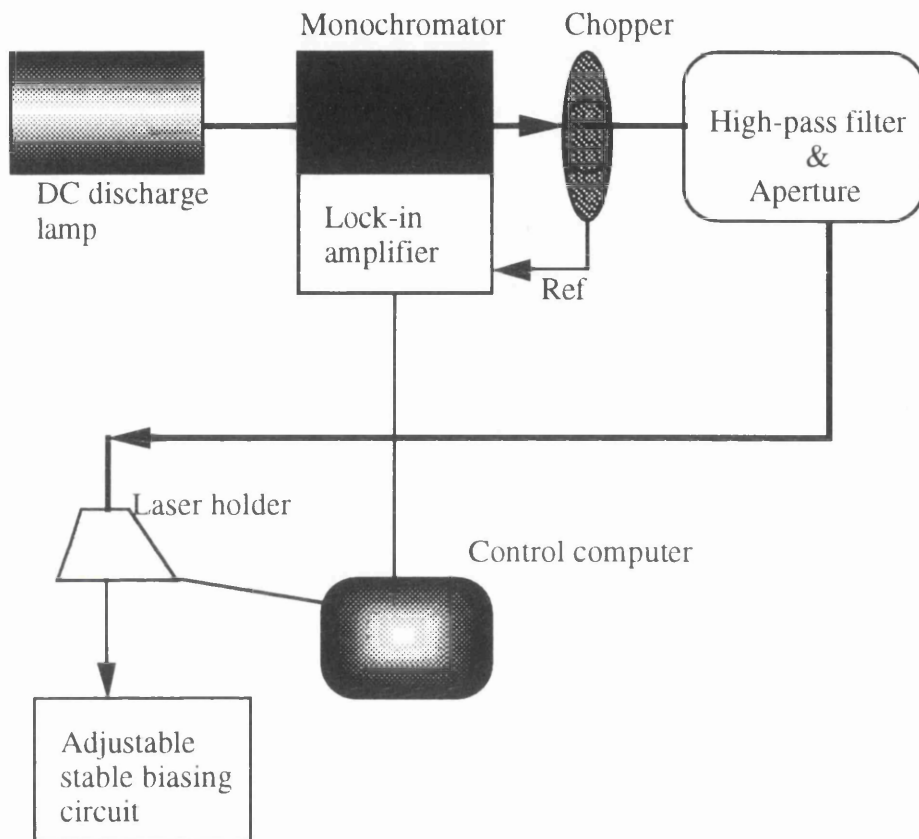


Fig.4-6. The setup for a photocurrent response measurement

semiconductor and to determine material quality. In the laser fabrication of this work, PL measurements were performed at 77°K to determine the extent of the quantum-well intermixing. The experimental setup for PL measurement is shown in Fig.4-4 .

Fig.4-5(a) shows the typical PL shifts for a ridge waveguide laser annealed in an RTA apparatus. The relative PL peak shift between the SiO<sub>2</sub> and SrF<sub>2</sub> covered regions (Fig.4-1(c)) reflects directly the bandgap shift by QW intermixing. Fig.4-5(b) demonstrates the PL shifts as a function of the anneal temperature. The SiO<sub>2</sub> capping layer was deposited by an E-gun apparatus through a low-temperature (< 50 °C) process. Fig.4-5(b) shows that a relative shift of over 30 nm can be achieved for the sample annealed at 940 °C or above for 50 seconds. Experimental results, to be described in chapter 6, showed that this bandedge shift was sufficiently large to greatly reduce the waveguide loss in the passive section.

#### 4.5 Photocurrent response measurement

Photocurrent measurement is a useful characterisation technique for structures which contain a PN junction. It can serve as a complementary technique to PL measurement, because it reflects the photons absorbed in the material, instead of the carriers being recombined to produce luminescence. Fig.4-6 is a block diagram of the set-up for photocurrent measurement.

In order to check the quality of the material in the range of disordering, a photocurrent response at zero bias, as shown in Fig.4-7, was measured. The excitonic peaks for transitions from both heavy and light holes to ground-state electrons are pronounced. Those peaks become weaker when the reverse bias is increased, because the overlap of the electron and hole wavefunctions in the QW is reduced [12] and the absorption strength is smaller. For  $V < 0$ , there exists a potential energy gradient in the QW, this results in a smaller electronic transition energy and the absorption edge moves toward longer wavelength. This is the so-called 'Quantum Confined Stark Effect (QCSE)'.

Because the height of the QW barriers after disordering was reduced, and the binding energy of excitons is small at room temperature, the excitonic peaks were less pronounced and hence merged into one. Due to the higher binding energy at lower temperature, e.g. 77° K, excitonic peaks were still significant even after quantum -well intermixing (not shown here).

Measuring the difference between the middle points of the absorption tails (Fig.4-7), before and after RTA, it was found that this difference was consistent with the relative PL shift observed in a PL measurement.

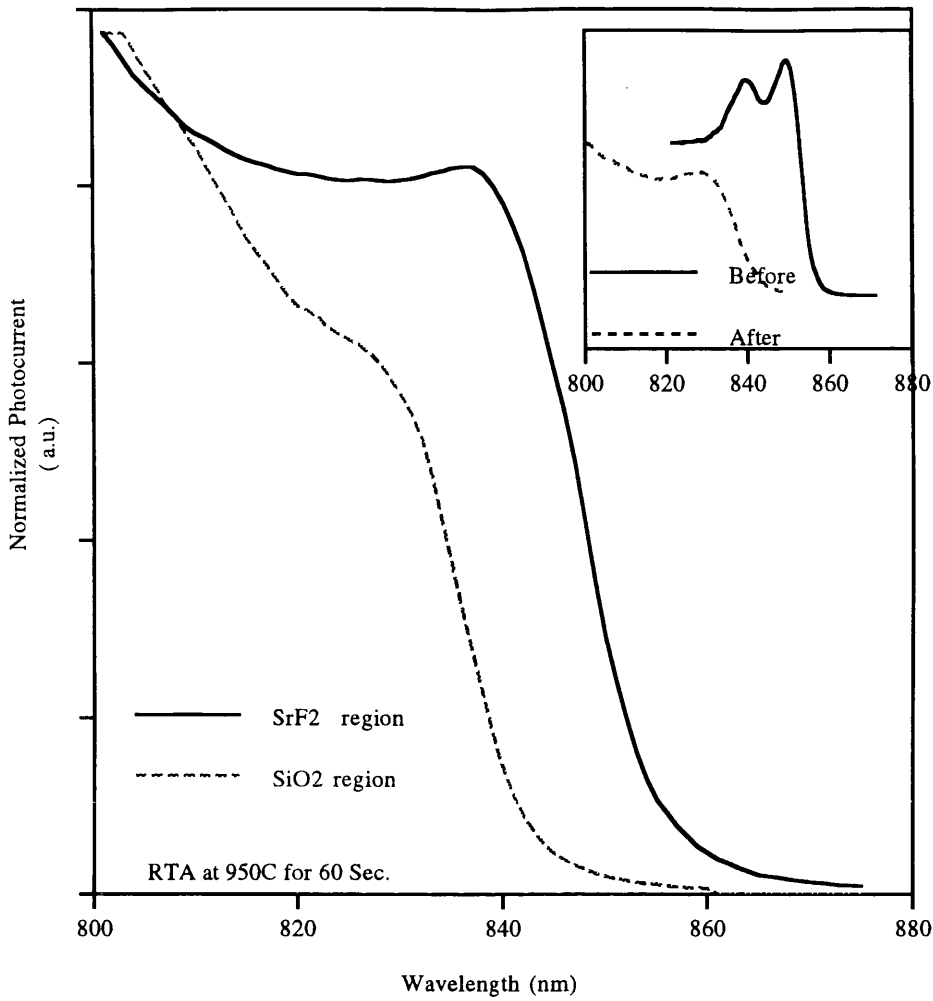


Fig.4-7. Photocurrent response for the sample disordered by IFVD process. Responses in the inset are from the sample disordered for shorter anneal time and lower temperature

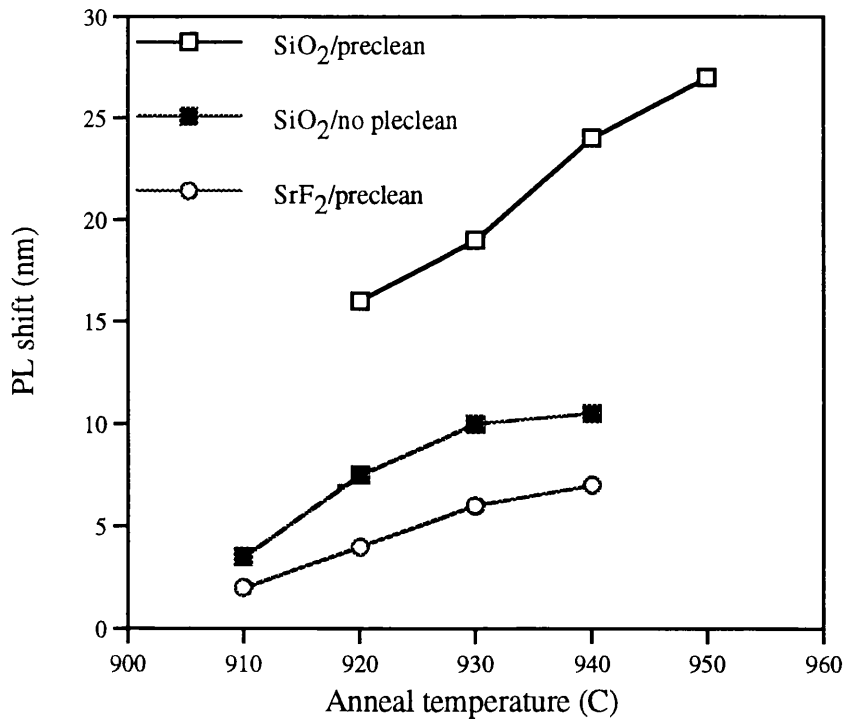


Fig.4-8. PL shifts with and without HCl precleaning for removing the native oxide on samples

#### 4-6 Native oxide effects

It has been observed that the presence of a native oxide significantly suppresses the quantum well intermixing[13]. In order to have successful disordering, the native oxide on the sample surface should be cleaned off before covering with a dielectric layer (details to be depicted in chapter 5). Fig.4-8 gives the shift in the PL peak for various precleaning and covering film situations. Note that the smallest PL peak shifts are obtained in the SrF<sub>2</sub>-capped region, provided that precleaning is used. For SiO<sub>2</sub>-capped region, there is a 24-nm blue shift for the sample annealed at 940° C for 30 seconds with HCl precleaning, but only a 10.5 nm blue shift if the precleaning is not used[13].

The thermal growth of a native oxide on GaAs[14,15] is affected both by the greater stability of gallium oxide, in comparison with the arsenic oxides, and by the relatively greater ease with which gallium is able to diffuse through a layer which is predominantly gallium oxide (Ga<sub>2</sub>O<sub>3</sub>) layer. The composition and thickness of the oxide are also determined by the growth temperature.

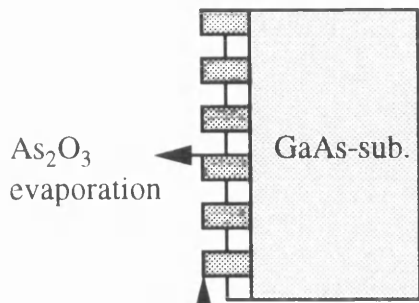
Fig.4-9 is a schematic diagram of the model for initial oxide growth [15]. Fig.4-9 (a) shows that native oxidation begins with chemisorbed oxygen at the surface, and the subsequent nucleation of Ga and As oxides. This nuclei film grows outward and the GaAs surface is covered by island-like Ga<sub>2</sub>O<sub>3</sub> oxide. Fig.4-9 (b) shows that the As oxide evaporates, leaving Ga<sub>2</sub>O<sub>3</sub> on the surface. In Fig.4-9 (c), the evaporation of As oxides and collection of Ga oxide proceed until a continuous layer of Ga<sub>2</sub>O<sub>3</sub> is formed all over the GaAs surface.

It appears that the relatively thin native oxide layer which forms on the surface after a limited period in ambient atmosphere at room temperature or at heated temperature during the subsequent processing, can considerably modify the rate at which gallium diffuses out of GaAs samples which are also covered by SiO<sub>2</sub> and/or SrF<sub>2</sub>. The out-diffusion of gallium from the GaAs/AlGaAs QW heterostructure, in turn, affects the intermixing rate between the wells and barriers of that heterostructure via the formation of defects. Additionally, Guido et al [16] have shown that the interdiffusion between surface gallium vacancies [ $V_{Ga}^-$ ] and surface arsenic antisite defects [ $As_{Ga}^+$ ] plays an important role in such QW intermixing processes.

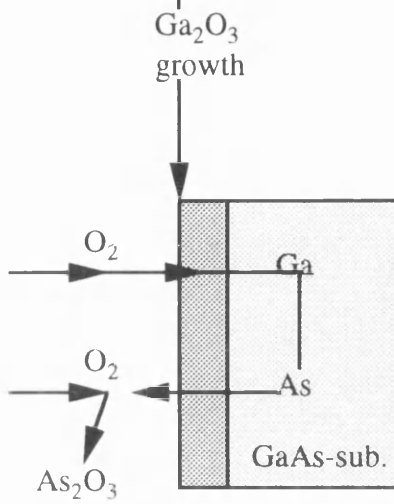
In summary, to obtain an adequate and controlled shift in absorption edge using the IFVD process based on SiO<sub>2</sub> covering layer, we need to remove the native oxide layer shortly before the deposition of SiO<sub>2</sub> and SrF<sub>2</sub> layers.

#### 4-7 Oxide-on-GaAs systems

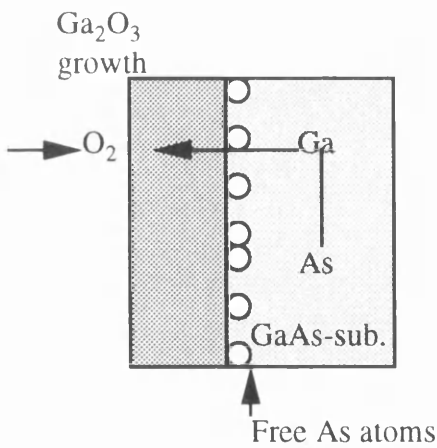
Oxide films grown upon a GaAs substrate can experience various types of stress. For instance, extrinsic stress arising from film-substrate adhesion [11] and due



(a) Initially, the oxidation begins with the breaking of Ga-As bonds. Island-like  $\text{Ga}_2\text{O}_3$  forms on the surface.



(b) Arsenic oxide evaporates, leaving  $\text{Ga}_2\text{O}_3$  grown all over the surface.



(c)  $\text{Ga}_2\text{O}_3$  keeps growing outward, while As atoms accumulate near the oxide-GaAs interface.

Fig.4-9. A model for the initial oxide growth and the interface formation of a thermal oxide on a GaAs surface [15].

to differential thermal expansion between the film and the substrate. The extrinsic stress can also be due to film lattice misfit with the substrate lattice, or the removal of grain boundaries during thin film grain growth. On the other hand, an intrinsic stress can result from crystal defects, such as dislocations and stacking faults.

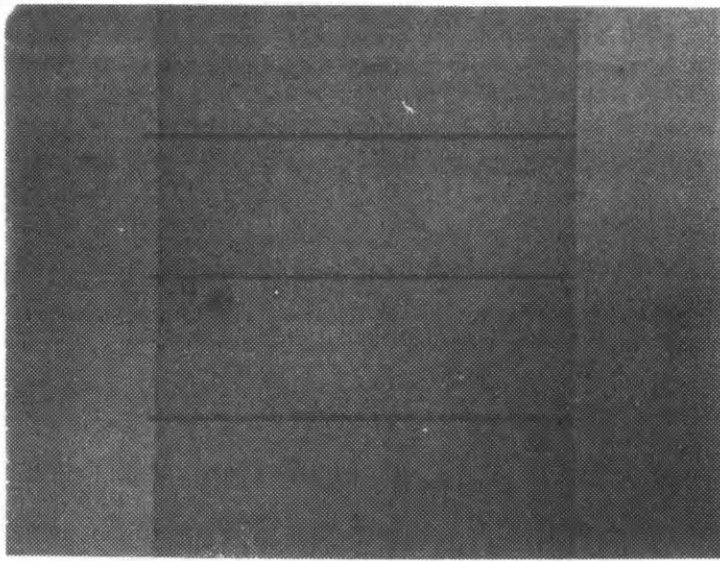
As native oxide grows[15], as shown in Fig.4-9, it is probable that contaminants on the original semiconductor surface will remain at the substrate-oxide interface, even after the oxidation process. When a sample is annealed, cracking may be promoted at these contaminated sites. In addition, intrinsic stress caused by dislocations and stacking faults may also introduce cracks both in the thin films and on the GaAs surface during annealing.

For samples with a worse surface morphology in the active section, larger PL shifts have been found in the worm-like damaged areas. The damage not only reduces the relative PL shift between the active and the passive sections, but also introduces extra leakage current through high surface recombination rate.

To minimize stress effects, optimum conditions for thin film deposition can be obtained[17]. Adjusting the deposition conditions, such as RF power, deposition pressure and temperature, will produce different degrees of stress. If a thin film is deposited under optimum conditions, less stress and better morphology can be obtained.

In an attempt to obtain optimum conditions for depositing high-performance dielectric films for quantum well disordering, samples were first covered with an evaporated 150 nm-thick  $\text{SrF}_2$  film which was deposited at the rate of 0.3 to 0.4 nm/min, and then capped by an  $\text{SiO}_2$  layer (200 nm thick) which was deposited by a PECVD process. The lines in Fig. 4-10(a) & (b) are the identification marks to indicate the region of the active section. For comparison, the  $\text{SiO}_2$  layers were deposited both by the standard existing process and by a process with new parameters. In the standard process, the  $\text{SiO}_2$  layer was deposited with an RF power of 10 Watt, a chamber pressure of 1000 mtorr, a temperature of 300°C and a deposition rate of 66.1 nm/min. A variety of annealing results were then obtained by adjusting the above process parameters in a series of trial samples. The annealed sample with the best (out of 12) morphology is shown in Fig.4-10(c). The deposition conditions for this sample were an RF power of 8 Watt, a chamber pressure of 730 mtorr, a temperature of 260°C, and a deposition rate of 55.6 nm/min. From Fig.4-10, it can be clearly seen that the worm-like cracks generated during the RTA process, under unfavourable annealing conditions, were not present. The results were obviously much better than for the standard process.

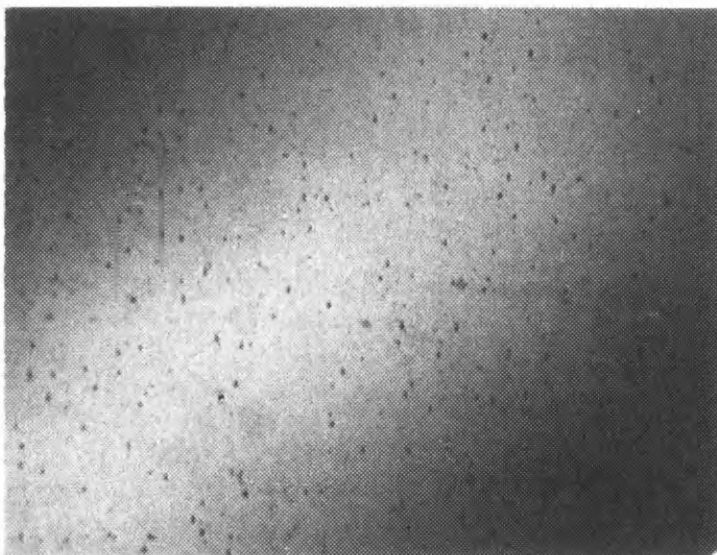
Due to the large demand for the only PECVD silica machine available in the department, this work was not continued further, but undoubtedly shows how to obtain



(a)



(b)



(c)

Fig.4-10 (a) The sample, with identification marks, before RTA processing (by the standard PECVD process). (b) The sample with worm-like cracks after RTA processing (by the standard PECVD process). (c) The sample with silica layer deposited under optimum conditions after RTA processing. Note that the RTA process was done at 930 ° C for 60 seconds.

superior dielectric films, compared to the standard ones, for the IFVD disordering process.

Rao et al [18] showed alternatively that a phosphorus-doped silicon dioxide layer could eliminate the influence of built-in strain and increase the reproducibility of the dielectric cap disordering. Furthermore, Si IID from the SiO<sub>2</sub> layer during annealing is a possibility which should be considered in certain cases. Guido et al [19] demonstrated that Si diffusion can have a significant influence on Al-Ga interdiffusion if a SiO<sub>2</sub> layer is employed during sample annealing. Under this circumstance, the GaAs contact layer must be relatively thick ( > 100 nm ) to effectively screen the Si diffusion from the SiO<sub>2</sub> source layer and prevent Si IID. If this condition is not met, the SiO<sub>2</sub> layer and the GaAs contact layer would react, resulting in a Si source at the SiO<sub>2</sub>-GaAs interface. The Si IID therefore also contributes to the QW intermixing, in addition to the vacancy-induced disordering.

#### 4-8 Summary

At the beginning of this chapter, the need for and the alternative types of quantum well disordering for an extended-cavity structure were introduced. The IFVD disordering mechanism was then depicted. The key technique, rapid thermal annealing, was described in detail. Afterward, PL measurement, followed by a complementary technique- photocurrent response, for evaluating the bandgap shift before and after a QW disordering were introduced.

Special efforts have been put into investigating the impact of a native oxide upon the IFVD process. A model was used to explain the formation of the initial native oxide growth and suggestions were given for ways to achieve successful disordering. This chapter ended up with an introduction to the oxide-on-GaAs system. It has been found that the surface morphology is an important factor that could not be ignored during QW disordering. Finally, it should be noted that the effect of Si IID from the SiO<sub>2</sub> layer may have to be taken into account during IFVD processing, if the GaAs surface layer is thin.

#### 4-9 References

- [1] D.G. Deppe, G.S.Jackson, and N. Holonyak, Jr., 'Coupled stripe Al<sub>x</sub>Ga<sub>1-x</sub>As-GaAs quantum well lasers defined by impurity-induced(Si) layer disordering', pp.632-634, 50(11), Appl. Phys. Lett., 1987.
- [2] R.L.Thornton, J. E. Epler, and T.L Paoli, 'Monolithic integration of a transparent dielectric waveguide into an active laser cavity by impurity-induced disordering', pp.1983-1985, 51(24), Appl. Phys. Lett., 1987.

- [3] S.R.Andrew, J.H.Marsh,M.C.Holland, and A.H.Kean, 'Quantum well laser with integrated passive waveguide fabricated by neutral impurity disordering' V.4,No.5,pp.426-428, IEEE Photon. Tech. Lett.,1992.
- [4] D.G.Deppe, N. Holonkak, Jr., W. E Plano. V.M.Robbins, J.M.Dallessasse, K.C. Hsieh and J. E.Barker, 'Impurity diffusion and layer interdiffusion in  $Al_xGa_{1-x}As$ -GaAs heterostructures ', pp.1838-1844, 64(4), J. Appl. Phys., 1988
- [5] J.Beauvais, J.H.Marsh, A. H.Kean, A.C.Bryce and C. Button, 'Suppression of bandgap shifts in GaAs/AlGaAs quantum wells using strontium fluoride caps', pp.1670-1672, V-28, No.17, Electron. Letters, 1992.
- [6] I.Gontijo, T.Krauss, R.M.De La Rue, J.S. Roberts, and J.H. Marsh, 'Very low loss extended cavity GaAs/AlGaAs lasers made by impurity-free vacancy diffusion', pp.145-146, V-30, No.2, Electron. Lett., 1994.
- [7] J.E. Epler, R. D. Burnham, R.L.Thornton, T. L.Paoli, M. C.Bashaw,' Laser induced disordering of GaAs-AlGaAs superlattice and incorporation of Si impurity' , pp.1447-1449, 49(21), Appl. Phys. Lett, 1986.
- [8] M.O'Neill, A. C. Bryce, J.H.Marsh, R.M. De La Rue, J.S.Roberts and C. Jeynes, 'Multiple quantum well optical waveguides with large absorption edge blue shift produced by boron and fluorine impurity induced disordering', pp.1373-1375, 55(14), Appl. Phys. Lett., 1989.
- [9] I. Gontijo, T.Krauss, J.H.Marsh, and R. M.De La Rue, 'Postgrowth control of GaAs/AlGaAs quantum well shapes by impurity-free vacancy diffusion', pp.1189-1195, V-30, No.5,1994.
- [10] E. S.Koteles, B.Eleman, P.Melman, J.Y.Chi, and C.A.Armiento, 'Quantum well shape modification using vacancy generation and rapid thermal annealing', S 779-787, No.23, Optical and Quantum Electronics, 1991.
- [11] K.N.Tu, J.W.Mayer and L.C.Feldman,`*Electronic Thin Film Science For Electrical Engineers and Material Scientists*', Macmillan Publishing Comp., New York, 1992.
- [12] C.Weisbuch and B.Vinter, ' *Quantum Semiconductor Structures*', chapter 3, Academic Press, New York, 1991.
- [13] H.H.Yee, S.Ayling, R.M.De La Rue, B.Vögele and Y.P.Song, 'Fabrication of high performance extended cavity double-quantum-well lasers with integrated passive sections', accepted for publication in IEE Proc. Part J Optoelectronics, 1996.
- [14] S.K.Ghandhi,`*VLSI Fabrication Principles: Silicon and Gallium Arsenide* Chapter 7, Wiley, New York, 1982
- [15] C.W.Wilmsen, R.W. Kee, and K.M.Geib, 'Initial oxidation and oxide/ semiconductor interface formation on GaAs', 16(5), pp.1434-1438, J.Vac.Sci.

Technol., 1979.

[16] L.J.Guido, N.Holonyak, K.C.Hsieh, and J.E.Baker, 'Depth-dependent native-defect-induced layer disordering in  $\text{Al}_x\text{Ga}_{1-x}\text{As-GaAs}$  quantum well heterostructures', 54(3), pp.262-264, Appl. Phys. Lett., 1989.

[17] W.R. Runyan and K.E.Bean, '*Semiconductor Integrated Circuits Processing Technology*', section 4.6, Addison-Wesley Inc., New York, 1990.

[18] E. V. K.Rao, A.Hamoudi, P.Krauz, M.Juhel and H.Thibierge, 'New encapsulant source for III-V quantum well disordering', pp.472-473, 66(4), Appl.Phys. Lett., 1995.

[19] L.J. Guido, N.Holonyak, Jr., K.C.Hsieh, R.W.Kaliski, and W.E.Plano, 'Effects of dielectric encapsulation and As overpressure on Al-Ga interdiffusion in  $\text{Al}_x\text{Ga}_{1-x}\text{As-GaAs}$  quantum-well heterostructures', pp.1372-1379, 61(4), J. Appl. Phys., 1987.

## Chapter 5 Extended-cavity laser diodes

### 5-1 Introduction

The linewidth-narrowed laser, with an integrated passive waveguide, is an important component for photonic integrated circuits (PICs) and optoelectronic integrated circuits (OEICs). It is well known that a laser with an extended cavity can effectively reduce the linewidth, which can be estimated by using the Schawlow-Townes formula (section 3-7). For a normal quantum well laser with an extended passive section, any blue shift of its lasing wavelength caused by the band-filling effect would rapidly increase absorption losses in the passive section due to the proximity of the band edges. In this work one of the QW disordering techniques, IFVD, was implemented to investigate how much the propagation loss can be reduced, and how far the lasing wavelength shift can be effectively controlled.

Integrated quantum-well disordered passive sections not only provide the low losses required for the passive waveguide section, but also allow the best optical coupling and virtually negligible optical power reflection at the transition between the active and passive sections (as discussed in section 5-7).

Before making extended-cavity lasers for the above purposes, the fundamental structure and waveguide analyses will be performed in section 5-2 and 5-3. In section 5-4, a low-damage/loss RIE process, MCP RIE, will be described in detail and compared to a conventional RIE process.

Both gain-guided and index-guided laser fabrication and experimental results are demonstrated in sections 5-5 and 5-6. A detailed discussion on the above topics follows in section 5-7, particularly for extended-cavity ridge waveguide lasers. Additionally, the degree of influence of the gain-guiding mechanism on the lasing wavelength shifts is compared with the impact of the index-guiding mechanism in this section.

### 5-2 Material structure

A variety of DQW structures have been used to fabricate different kind of laser diodes in this work. The structure used for fabricating extended-cavity ridge waveguide lasers was a symmetric DQW MBE material, details of which are tabulated, in the sequence of grown layers, in Table 5-1 as below.

Five layers, including QWs and barriers, were deliberately undoped, because this can effectively reduce free carrier absorption. The thickness of the QW layer is very critical on the optical confinement factor and the quantization of electronic energy levels

in the band diagram, which, in turn, affects the threshold current [1] and the lasing wavelength of this diode (section 2-2 & 2-3).

Table.5-1 Details of the symmetric DQW MBE material used for fabricating extended-cavity laser diodes

Layer	Thickness (nm)	Material / Al fraction	Concentration (cm <sup>-3</sup> )	Purpose of layers
Sub	-	GaAs	N <sup>++</sup> 5E18	Contact layer
0	500	GaAs	N <sup>+</sup> 2E18	Buffer
1	1500	AlGaAs / 0.40	N 5.5E17	Lower cladding
2	100	AlGaAs / 0.20	Undoped	QW barrier
3	10	GaAs	Undoped	Q W
4	10	AlGaAs / 0.20	Undoped	QW barrier
5	10	GaAs	Undoped	QW
6	100	AlGaAs / 0.20	Undoped	QW barrier
7	700	AlGaAs / 0.40	P <sup>+</sup> 1E18	Upper cladding
8	100	GaAs	P <sup>++</sup> 5E18	Contact layer

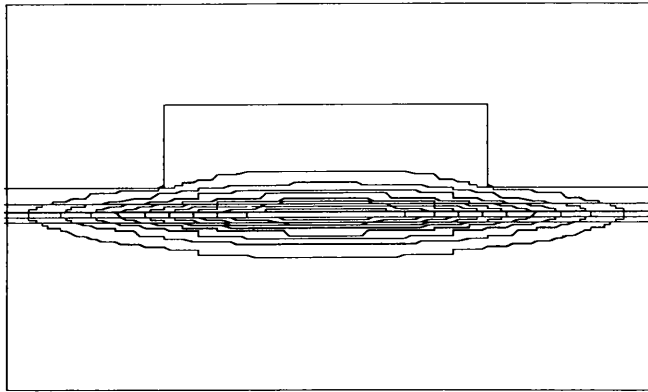
Additionally, as mentioned in literature, e.g.[2], the thickness of the barrier layers between the QWs also has an impact on the carrier tunneling probability, which obviously would affect the transmission current density.

In order to maintain single transverse-mode operation and to have low radiation coupling loss, the thicknesses of lower and upper cladding layers should be well controlled [3].

### 5-3 Waveguide structure

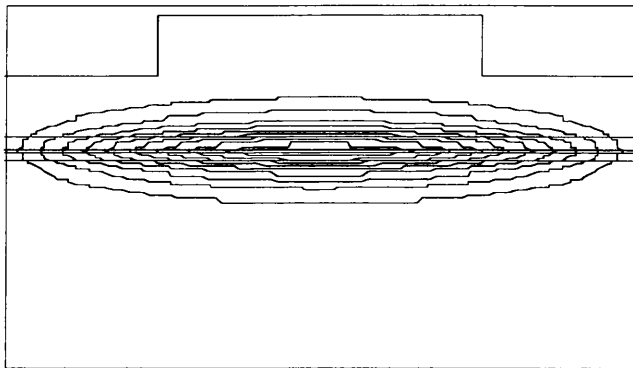
In this work, a symmetric DQW structure (B423) was used to fabricate extended-cavity ridge waveguide lasers. The TE<sub>00</sub> mode contours of this structure are shown in Fig.5-1. For investigation of the lasing wavelength shift due to the gain-loss competition of an extended-cavity structure (see section 3-2), a sufficient lateral (i.e. parallel to the junction) refractive index step  $\Delta n_L$  should be maintained to ensure that the ridge waveguide laser operates in the strongly index-guiding regime, which makes the carrier concentration, on the average, beyond threshold nearly unchanged and the red shift due to gain-loss competition in the composite structure is clear.

For these ridge waveguide structures, the refractive index step was set to a minimum value of  $4 \times 10^{-3}$ , and the ridge was etched to 1  $\mu\text{m}$  high and 2  $\mu\text{m}$  wide. At the operating wavelength of 850 nm, the ridge waveguide width (2  $\mu\text{m}$ ) is narrower



(a) B423: Rib height :  $1 \mu\text{m}$  ; Width:  $2 \mu\text{m}$

(Note):The intensities of the field contours are 1%, 10 %, 20%, 30 %, 40%,.....(from the outermost inward).



(b) B423: Rib height :  $0.6 \mu\text{m}$  ; Width:  $2 \mu\text{m}$

Fig. 5-1.  $\text{TE}_{00}$  mode profiles of a ridge waveguide ( B423 )  
 (a)  $W = 2 \mu\text{m}$ ,  $H = 1 \mu\text{m}$ , (b)  $W = 2 \mu\text{m}$ ,  $H = 0.6 \mu\text{m}$ , where  $W$ ,  $H$  are the width and the height of the ridge respectively.  
 (The top layer, above the ridge, is air )

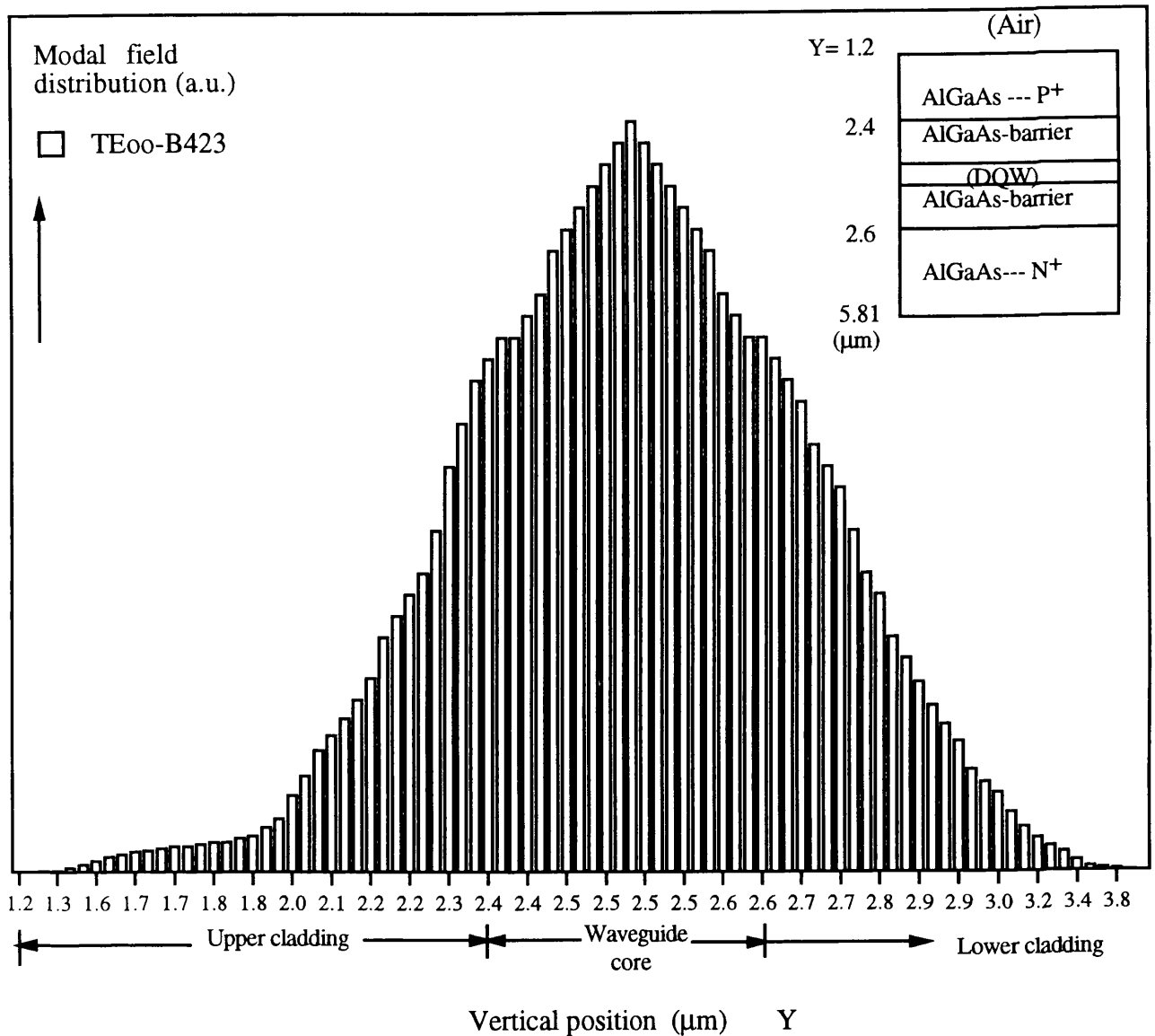


Fig.5-2 The detailed modal distribution of the TE<sub>00</sub> mode at the centre of the waveguide ridge for DQW structure B423.  
 Note that the mesh spacings are not the same for the sake of saving memory and calculation time.(The centre of the QW region is at  $y = 2.52 \mu\text{m}$ )

than the critical width of  $2.7 \mu\text{m}$  (see section 2-3), below which single lateral mode operation can be maintained. However, the outermost contour (Fig.5-1(a))(1%) of this mode profile is quite close to the ridge sidewalls. For the second case, the outermost contour is further away from the ridge sidewalls with shallower ridge step (Fig.5-1(b)), the trade-off of which is having a weaker lateral-mode confinement. To reduce the sidewall-scattering loss, a low-damage etching process should be adopted.

As mentioned in the previous section, the thickness of the upper cladding layer was designed to  $1.2 \mu\text{m}$ , so the ratio of the square of the optical field at the interface between the contact and the upper cladding layers to that at the QW centre is as low as  $2 \times 10^{-7}$ . This result clearly indicates that the radiation coupling loss of the evanescent tail is virtually negligible by this design consideration.

Fig.5-2 shows the vertical modal-distribution of the  $\text{TE}_{00}$  mode for the DQW structure B423.

#### **5-4 Magnetically confined plasma RIE (MCP-RIE)**

Reactive ion etching (RIE) has long been used as an effective technique to fabricate semiconductor devices. It not only provides very good pattern transfer from the mask to the semiconductor surface, but also can give vertical sidewalls and a smooth surface [5]. However, RIE processes may induce etch damage which potentially degrades both the optical and the electrical properties of the material. It was found that damage on the sidewalls would generate high scattering loss for a GaAs/AlGaAs ridge waveguide structure [6].

In our department, a conventional parallel-plate RIE system (Plasma Technology RIE80) (Fig.5-3) has been used for most GaAs etching. When the etching was carried out at DC bias of  $-350 \text{ V}$  with a  $\text{SiCl}_4$  flow rate of 9 SCCM (Cubic centimeter per minute at standard temperature and pressure), RF power of 100 Watts, an etch pressure of 10.5 mTorr and the table temperature was fixed at  $38^\circ \text{C}$ , a damage depth of 10 nm was observed by using a quantum-well intermixing probe [7].

To alleviate the damage caused by ion bombardment, the bias voltage and, equivalently, the RF power density need to be reduced. For most applications, nonselective and damage-low etching is required. How to obtain vertical and smooth sidewalls with negligible etch damage becomes a challenging and increasingly important goal of the dry etching work.

In a good reactive ion etching (RIE) system, a stable plasma should be easy to maintain by separating the extraction of the plasma for etching purposes from the generation of the plasma. It has been found that an electron cyclotron resonance (ECR) RIE machine can fulfill this requirement. Fig.5-4 is a schematic diagram of the Plasmatech ECR system. Microwave energy of 2.45 GHz is guided by a circulator into

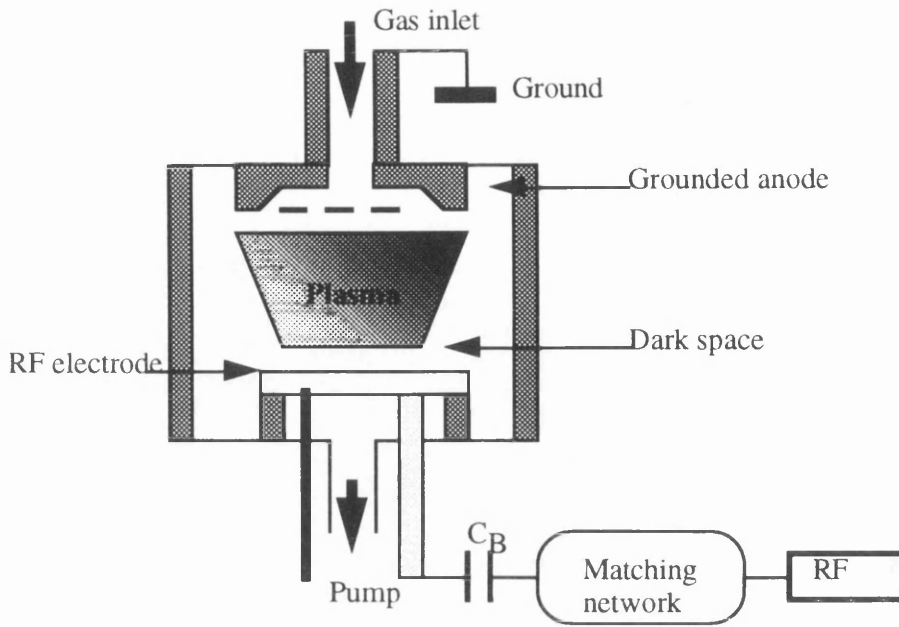


Fig.5-3. A conventional parallel-plate reactive ion etching system [4]

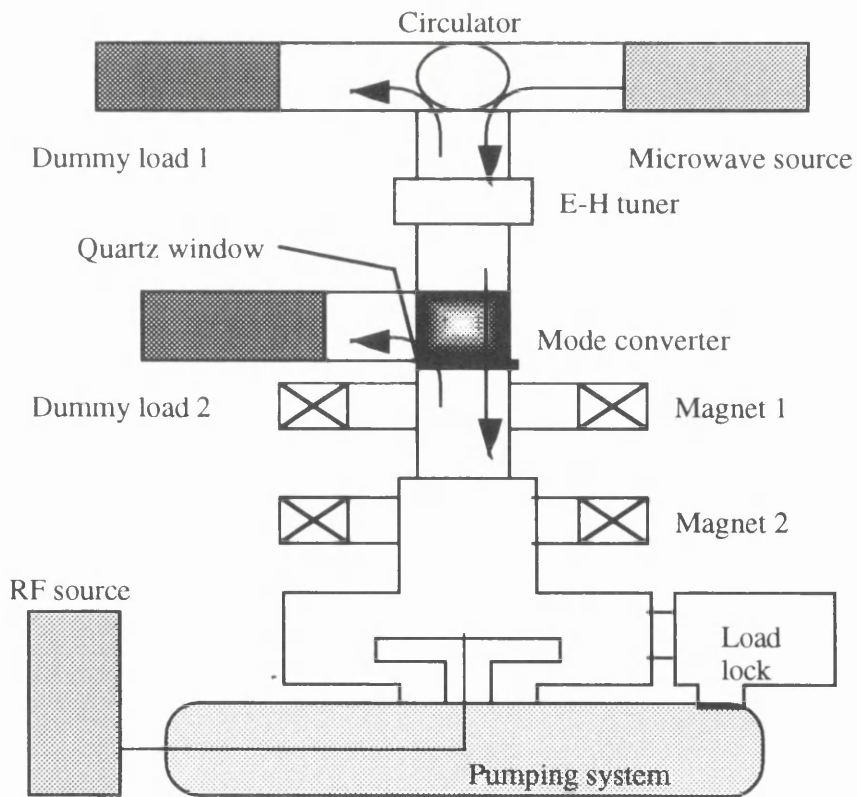


Fig.5-4 Schematic diagram of Plasmatech etching system [5]

a section of rectangular waveguide and then into E-H tuner. A mode converter follows and transforms the  $TE_{10}$  mode of the rectangular waveguide into the  $TE_{11}$  mode of the circular waveguide. Reflected power from the plasma traveling in the circular waveguide is absorbed in dummy load 2, while reflected power in the rectangular waveguide is absorbed in dummy load 1. Magnets are used for generating magnetic field for electron cyclotron motion. The specimen table is driven by a 13.45 MHz RF power supply, and it is used to extract the reactive ions. It should be stressed that the microwave power for maintaining the discharge is independent of the RF-driven electrode for extracting the reactive ions. It is therefore easy to generate a stable plasma.

We found in preliminary work that using  $SiCl_4$  in an ECR-RIE machine led to rough sidewalls with undercut profiles [8]. We have developed a better etching recipe which is to reduce the magnetic field to a value well below that required to satisfy the ECR condition. This is the so-called 'Magnetically Confined Plasma'(MCP)-RIE. Under low magnetic field condition ( $<300$  Gauss), a stable plasma column is formed in this system, which still can maintain the required cyclotron movement, and so drastically reduce the loss of electrons and ions to the chamber walls of this machine.

In Fig.5-5, it can be found that smooth and damage-low sidewalls [5] were formed by using MCP-RIE for the fabrication of extended-cavity lasers in this work, the ridge of which is  $2\ \mu\text{m}$ -wide and  $1\ \mu\text{m}$ -high. Details of the etching parameters used for this fabrication are given in the next section .

## **5-5 Fabrication of extended cavity lasers**

The fabrication of nondisordered extended-cavity lasers is easier than that of disordered ones. For the fabrication of the latter, QW intermixing using the IFVD technique, as described in chapter 4, must be performed in advance of other processing.

### **5-5-1 Fabrication of an extended-cavity ridge waveguide laser**

The fabrication details for a disordered extended cavity laser with a ridge waveguide section are described step by step as follows:

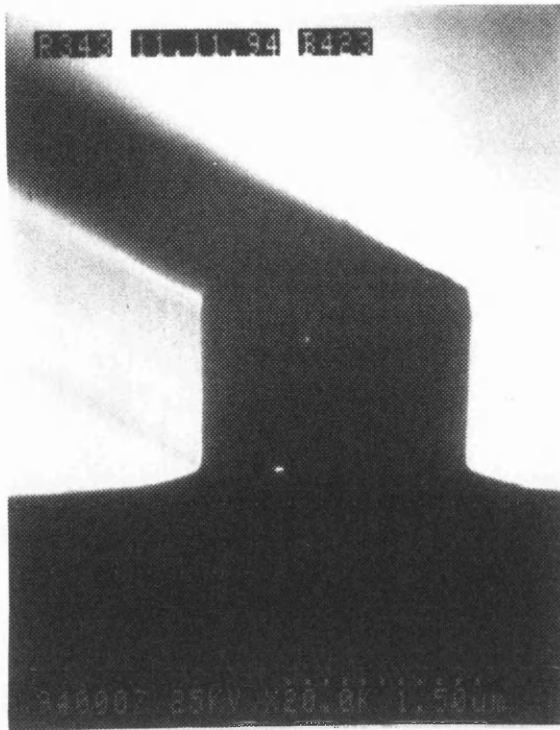
#### *1. Sample cleaning*

Samples must be cleaned according to following procedures:

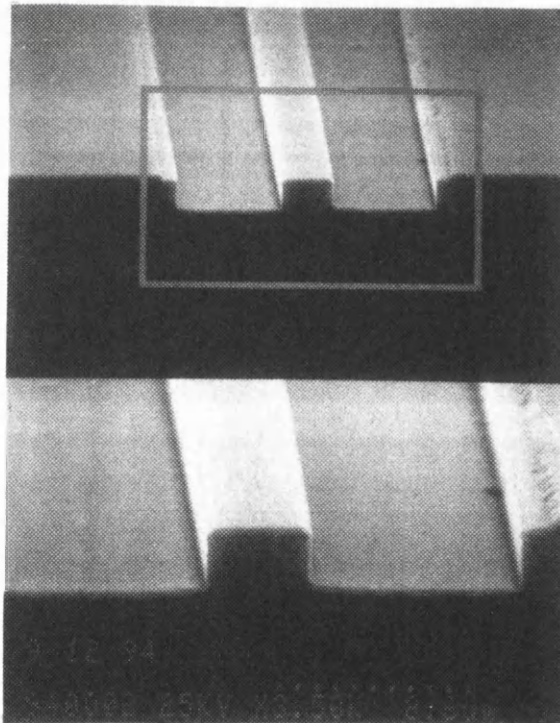
- (a) Immerse in Opticlear and clean ultrasonically for 5 minutes, and then blow dry.
- (b) Repeat the above process by changing the organic solvents with acetone, methanol, and RO water in order.

#### *2. Removal of the native oxide*

Immerse samples in diluted HCl acid (36.5%) for 1 minute and rinse in RO



(a)



(b)

Fig.5-5.SEM micrographs of (a)the smooth and vertical ridge sidewalls after MCP RIE process, and (b)the well-prepared extended cavity laser for testing.

water and fully blow dry.

### 3. $SrF_2$ evaporation

A 150 nm-thick  $SrF_2$  film is evaporated in a tungsten boat with a current around 50 Amp at an evaporation rate of 0.4 nm/sec. Before this evaporation, the  $SrF_2$  powder should be degased to completely expel the moisture.

### 4. *Definise the passive section*

The dielectric film is then patterned to define the passive section, by an appropriate photomask, using photoresist Shipley S1400-31. Afterward, the sample is developed ( 1 part RO water : 1 part developer) for 75 seconds, rinsed in RO water for 2 minutes, blown dry and then postbaked at 90° C for 30 minutes.

### 5. *Select the $SrF_2$ -capped region:*

The  $SrF_2$  film in the passive section is removed using HCl for 1 minute, with the aid of cotton bud to rub out the unwanted film, if necessary. After that, photoresist should be cleaned off and fully blown dry.

Note that the above film patterning can also be done by a lift-off technique.

### 6. $SiO_2$ deposition

Samples are cold-loaded in a PECVD chamber to deposit  $SiO_2$  layer (200 nm) at 350° C.

### 7. *Rapid thermal annealing (details in section 4-3):*

Anneal samples at 900-950° C for an appropriate time duration, generally no more than 60 seconds, to get a sufficient differential PL shift for the device requirement.

### 8. *PL measurement:*

Measure the differential PL shifts for the disordered and the control samples at 77° K. Check if the QW intermixing is sufficient for device fabrication.

### 9. *Stripe off the dielectric films:*

Remove the upper  $SiO_2$  layer by immersing samples in a buffered HF acid for 30 seconds. The  $SrF_2$  layer is then stripped off in HCl (36.5%) for 1 minute. After that, the sample is rinsed for 2 minutes and fully blown dry. It is essential to check under a microscope to make sure if these films are totally removed.

*(Note):The above QW disordering process is skipped, if a nondisordered sample is fabricated.*

### 10. *Removal of $P^+$ contact layer in the passive waveguide section:*

a. Pattern samples by the standard lithography and then postbake at 120° C

for 30 minutes.

b. The exposed region in the passive section is then wet-etched by using 1 part  $\text{NH}_3$  : 20 parts  $\text{H}_2\text{O}_2$  for 8 seconds. Rinse and then blow dry.

*11. Sample preparation for the subsequent RIE process:*

- a. Deposit  $\text{SiO}_2$  layer (as the etching mask) in a PECVD chamber.
- b. Spin-on the photoresist S1400-17 and bake for 30 minutes at  $90^\circ\text{C}$ .
- c. Develop, rinse and blow dry. Postbake samples at  $90^\circ\text{C}$  for 10 minutes.

*12. RIE processing:*

The  $\text{SiO}_2$  layer was dry-etched with  $\text{C}_2\text{F}_6$  in a parallel-plates rf RIE system. The GaAs ridge was then etched by MCP-RIE as described in the previous section. Table 5-3 shows the etching parameters of these processes:

Table.5-3

Material	Technique	Gas	Flow (sccm)	RF power (Watts)	Pressure (mTorr)	Bias (volts)
$\text{SiO}_2$	RIE	$\text{C}_2\text{F}_6$	20	100	12	-460
GaAs(*)	MCP-RIE	$\text{SiCl}_4/\text{O}_2$	15/1	40	0.63	-160

(\*)The magnetic flux density is 300 Gauss.

13. Fully clean off the resist and deposit  $\text{SiO}_2$  layer for passivation by PECVD.

*14. Open the contact window*

Open the contact window by a lithography using a contact mask.

15. Wet-etch the silica as step 9 and clean off the photoresist. The ridge is thus formed.

16. Deoxidize surface oxide by immersing samples in the acid of 1 part  $\text{NH}_3$ : 2 part RO water for 40 seconds.

17. Evaporate Ni/Au on the  $\text{P}^+$ -GaAs contact layer.

18. Thin samples to  $200\ \mu\text{m}$  thick, and fully clean samples in a reflux unit by using Opticlear to remove any wax residual. Then carefully clean the sample as step 1.

19. Deoxidize samples and then evaporate Au/Ge/Au/Ni/Au on the N-GaAs contact layer.

20. Scribe, cleave and test for the sample needs.

For the fabrication of interest here, the lasers were cleaved with five different passive section lengths of 500, 690, 800, 1000, and  $1200\ \mu\text{m}$ , and with the active section length fixed at  $460\ \mu\text{m}$  (see Fig.5-6 (a)).

## 5-5-2 Fabrication of an extended-cavity oxide stripe laser

### (a).Material structure

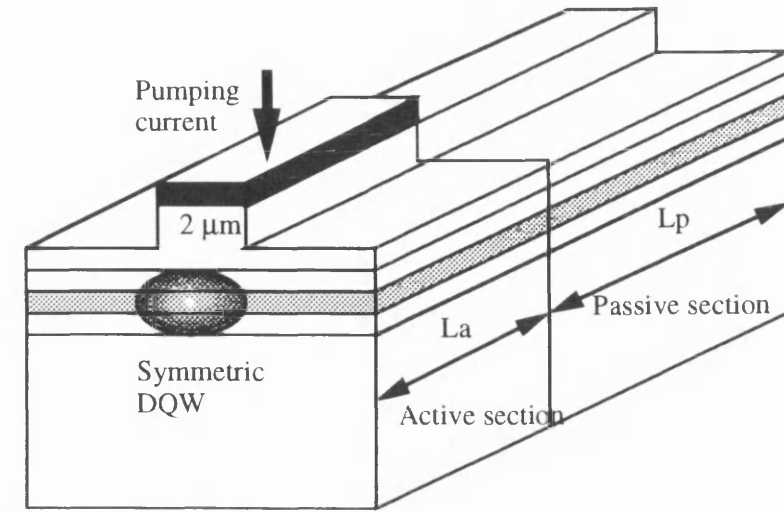
An MOCVD-grown material with GRIN SCH structure was used for this fabrication, details of which are demonstrated in Table 5-4. The laser geometry is shown in Fig.5-6(b) with details of capping layers for the IFVD process (Fig.5-6(c)), in which we can find that the contact stripe is 75  $\mu\text{m}$  wide, the active section is 460  $\mu\text{m}$  long, and the passive waveguide section was cleaved with varying lengths of 460, 690, and 800  $\mu\text{m}$ .

Table 5-4.The structure details of DQW QT632

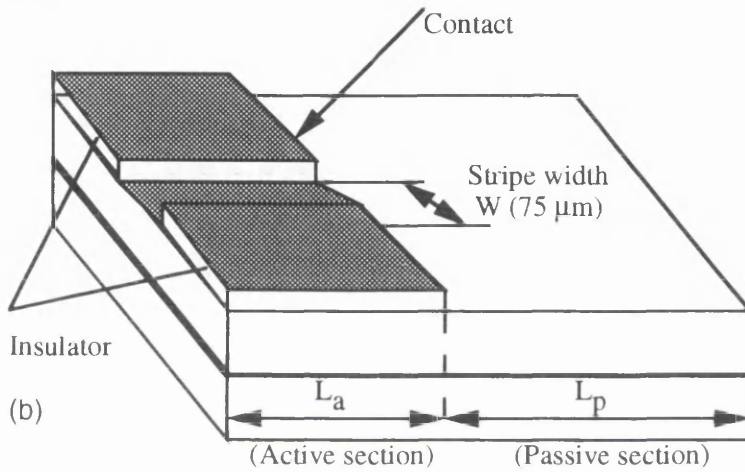
Layer	Thickness (nm)	Material / Al fraction	Concentration ( $\text{cm}^{-3}$ )	Purpose of layers
Sub	-	GaAs	$\text{N}^{++}$ 2.6E18	Contact layer
0	500	GaAs	$\text{N}^+$ 1 E18	Buffer
1	1500	AlGaAs / 0.40	$\text{N}$ 7.7E17	Lower cladding
2	100	AlGaAs / 0.20	Undoped	Graded barrier
3	10	GaAs	Undoped	Q W
4	10	AlGaAs / 0.20	Undoped	QW barrier
5	10	GaAs	Undoped	QW
6	100	AlGaAs / 0.20	Undoped	Graded barrier
7	1500	AlGaAs / 0.40	$\text{P}^+$ 5.4E17	Upper cladding
8	100	GaAs	$\text{P}^{++}$ 1.8E19	Contact layer

In addition to the formation of a ridge waveguide, the fabrication processes of an extended-cavity oxide stripe laser have no much difference from those of a ridge waveguide laser. The fabrication details are described as follows:

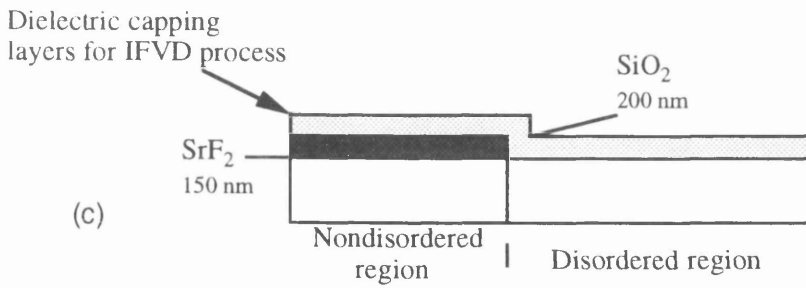
- 1.Sample cleaning and then silica deposition (200 nm) by PECVD.
- 2.Use standard lithography to open the active region on the resist pattern.
- 3.Use diluted HF acid to etch off the silica layer in the active region.
- 4.Use standard lithography to open 5- $\mu\text{m}$  stripes for the section mark.
- 5.Etch the above stripe marks using 1 part  $\text{NH}_3$  : 20 parts  $\text{H}_2\text{O}_2$  for 6 seconds.
- 6.Clean off the photo resist and postbake at 90°C for 30 minutes.
- 7.Evaporate  $\text{SrF}_2$  film in a conventional Bell jar.
- 8.Anneal control sample, measure PL shift, and then anneal LD samples.
- 9.Use buffered HCl (36.5%) to remove  $\text{SrF}_2$  film for one minute.
10. Use HF acid to clean off the silica film.
11. Check by a microscope if both dielectric films are gone.



(a)



(b)



(c)

Fig.5-6 Schematic diagrams of an extended-cavity (a) ridge waveguide, (b) oxide stripe laser. (c) The dielectric capping layers for the IFVD process.

12. Open the passive section and remove contact layer using the same recipe as step 5
13. PECVD silica deposition ( 200 nm thick ).
14. Open the contact window.
15. Etch off the silica capped on the window region and then remove the resist.
16. Deoxidize samples in 1 part  $\text{NH}_3$  : 2 parts  $\text{H}_2\text{O}$  for 40 seconds.
17. P contact evaporation.
18. Thin and fully clean the samples.
19. Chemically etch away the mechanical damage from the sample thinning.
20. N contact evaporation.
21. Scribe, cleave and test.

The details of the above processes are similar to those of making a ridge waveguide laser described in the previous subsection.

## **5-6 Experimental results**

By using the photomask designed for the laser fabrication, an 8 mm-wide sample could be scribed and cleaved into 20 to 25 extended-cavity lasers with the same cavity length. The chips near the edges of the samples generally gave worse performance compared to those from the central part and were not used. For both extended-cavity ridge waveguide and oxide stripe lasers, it should be noted that the data given in sections 5-6 and 5-7 were obtained from the typical values for the five best ones out of ten to twelve. The values within this selected group varied by between five and ten percent.

### **5-6-1 Measurements**

#### *A. L-I curves and lasing spectra*

Fig.5-7 shows the system setup for measuring light-current (L-I) curves and lasing spectra. The L-I characteristics were measured by using current pulses with a 400 -ns pulse width and with a repetition rate of 1 KHz. The lasers were maintained at 20°C by a Peltier Effect cooler. A family of L-I curves for the disordered extended-cavity lasers, with passive section lengths as parameters, are shown in Fig.5-8(a). From which it can be seen that the laser with a 1 mm-long disordered passive waveguide and a 460  $\mu\text{m}$ -long active section had a threshold current of only 18 mA, a small increase compared with 15 mA for lasers without a passive section. This confirms that the propagation loss of the passive waveguide was small [9], as discussed in the next subsection.

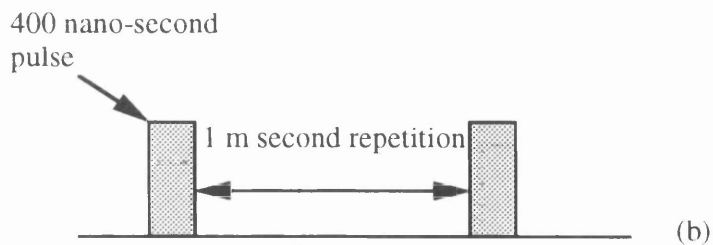
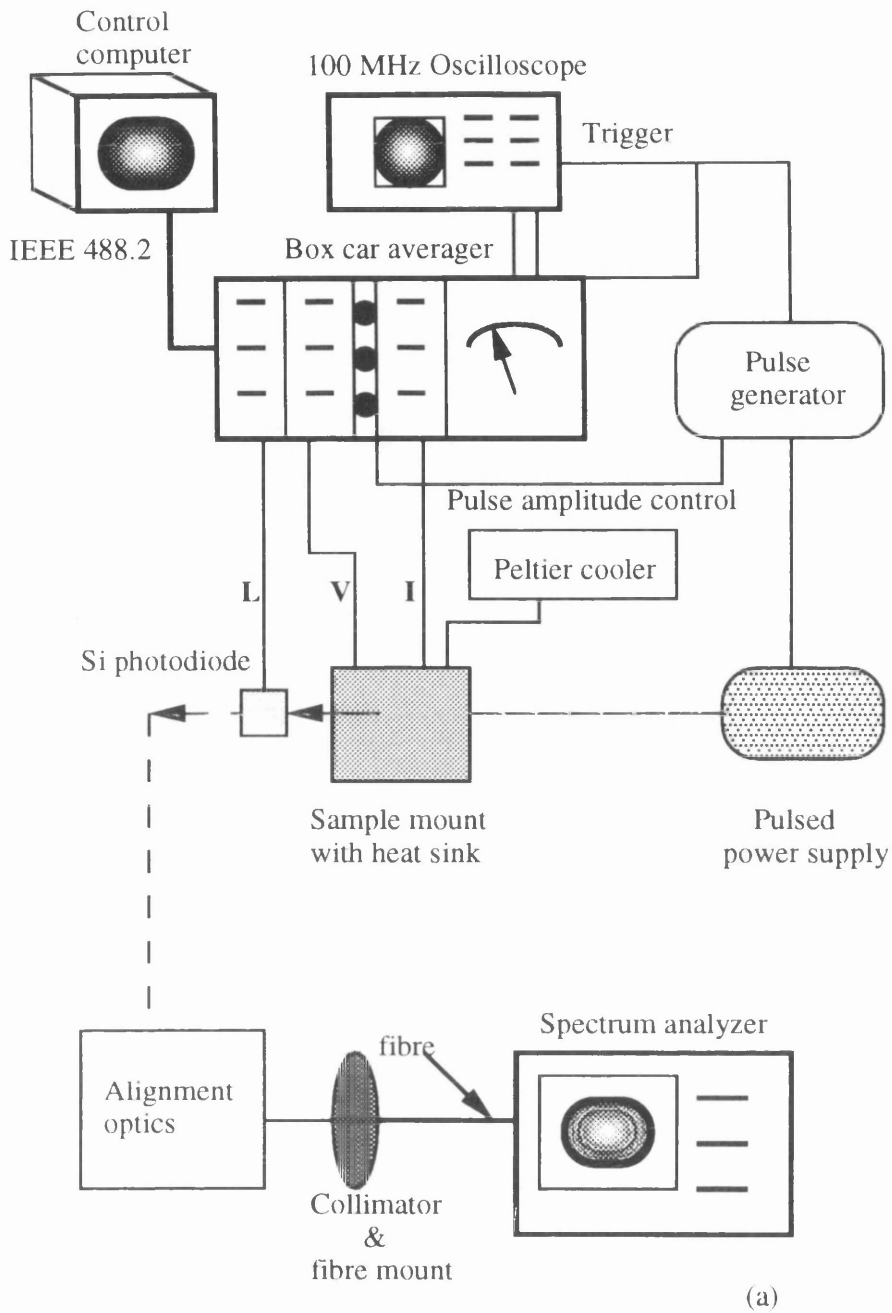
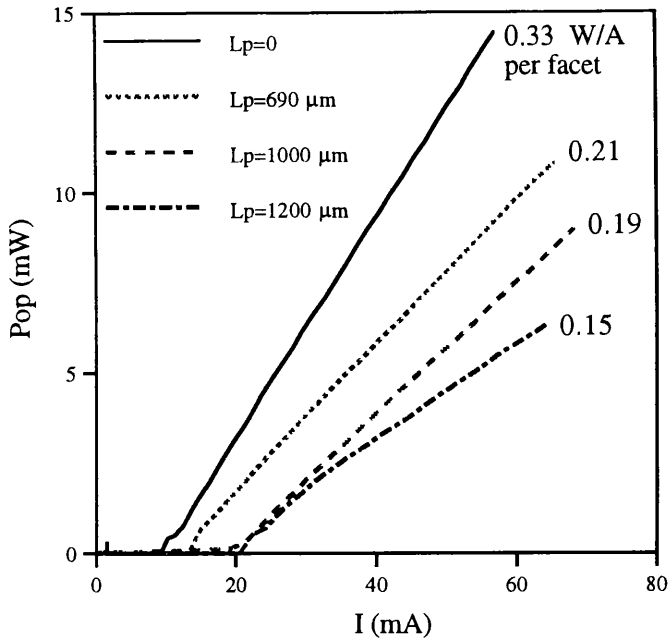
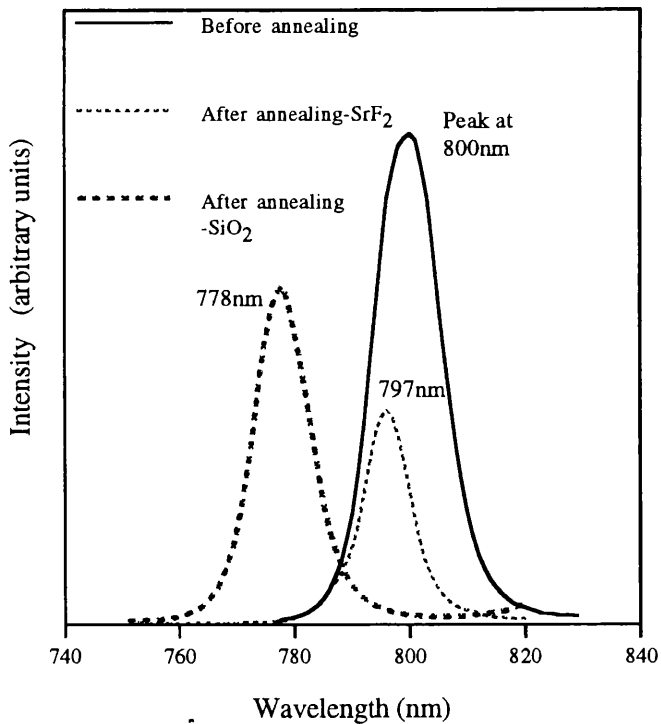


Fig.5-7. (a). The system setup for measuring L-I curves and lasing spectra. (b). Pulse signal for the test in pulse operation



(a)



(b)

Fig.5-8 (a) L-I curves of the disordered extended-cavity ridge waveguide lasers with passive-section lengths as parameters.

(b) PL peaks of both the passive and active sections before and after RTA processing.

The same measurement conditions as above were used to obtain the lasing spectra at the highest resolution, 0.1 nm, of spectrum analyzer used.

### B. PL measurements

PL shifts of disordered samples were measured at 77 °K (as described in chapter 4), the details of which are shown in table 5-2 below:

Table.5-2 PL peaks of extended-cavity lasers at 77 °K

#### A.Ridge waveguide lasers

PL peaks before RTA (nm)		PL peaks after RTA (nm)		Relative PL shifts (nm)	
SrF <sub>2</sub>	SiO <sub>2</sub>	SrF <sub>2</sub>	SiO <sub>2</sub>	SrF <sub>2</sub>	SiO <sub>2</sub>
800	800	797	778	3	19

#### B.Oxide stripe lasers

PL peaks before RTA (nm)		PL peaks after RTA (nm)		Relative PL shifts (nm)	
SrF <sub>2</sub>	SiO <sub>2</sub>	SrF <sub>2</sub>	SiO <sub>2</sub>	SrF <sub>2</sub>	SiO <sub>2</sub>
808	808	807	796.5	1	11.5

Fig.5-8 (b) shows the PL peaks of the waveguide section before and after RTA processing for the disordered extended-cavity ridge waveguide lasers.

### C.Propagation loss measurements

The propagation loss measurement was undertaken based upon the model demonstrated in section 3-1, in which the propagation losses were calculated by the slope of the threshold current ratio of the composite-cavity laser to the solitary laser.

## 5-6-2 Experimental results

### A. From extended-cavity ridge waveguide lasers

The lateral refractive index difference of the etched ridge waveguide was about  $4 \times 10^{-3}$ , which was computed by using a variational method. This provided good lateral confinement, ensuring that the laser operated in the index-guiding regime. This behaviour was confirmed by the single-lobe patterns from the far-field measurement shown in Fig. 5-9(a). The single lateral mode was preserved even when the injection current was six times (or more) larger than the threshold current. Under these circumstances, the carrier concentration, on the average, remained constant, so the carrier induced shift was nearly clamped beyond threshold [10], which can be confirmed by Fig. 5-9(b). The stable lasing condition implied that strong index-guided focusing was still dominant over the carrier-induced defocusing [10].

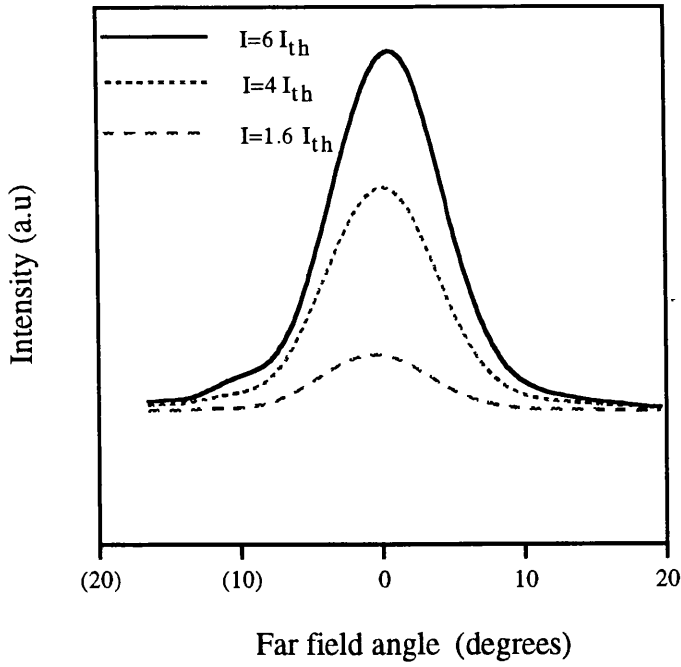


Fig.4 (a)

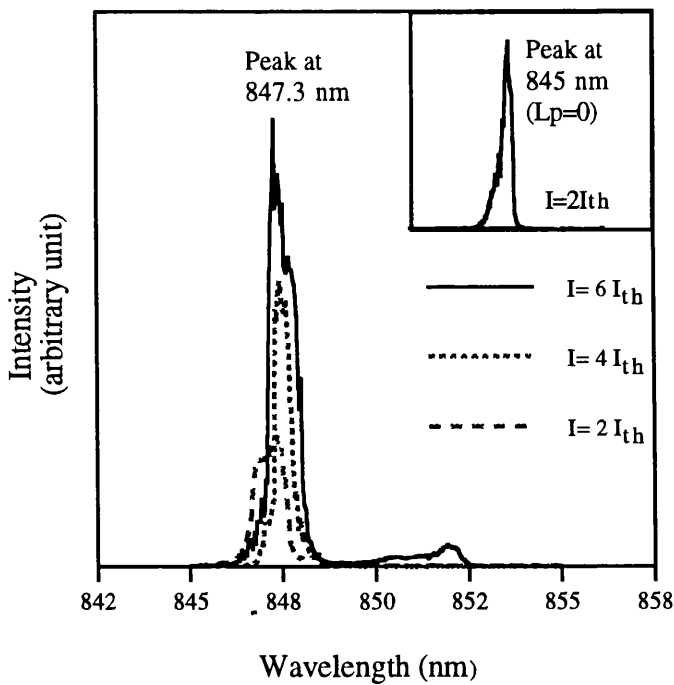
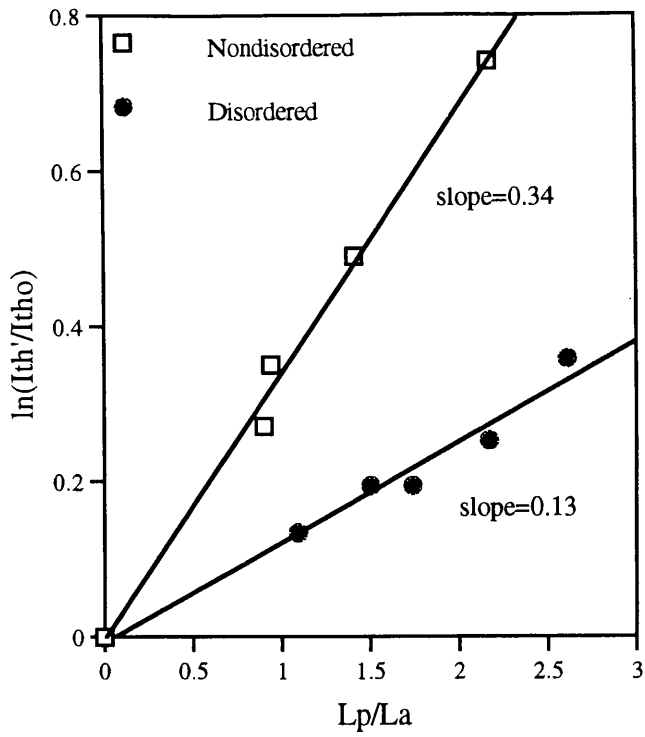
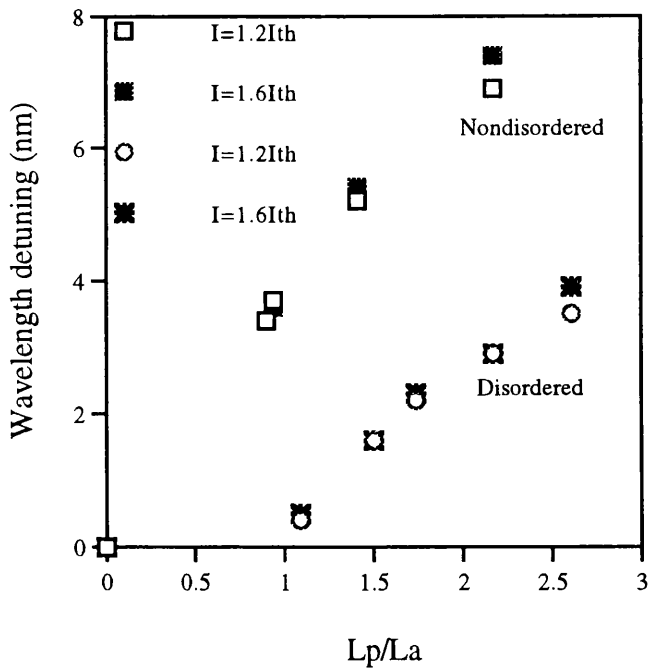


Fig.5-9 (a) Far-field patterns at different current levels. Single-lobe response confirms single lateral-mode operation. (b) Lasing spectra of the composite laser with 1 mm passive-section length with currents as parameters. The inset is the spectrum of a solitary laser for comparison.



(a)



(b).

Fig.5-10. (a)Threshold current change, and (b) lasing wavelength shifts as a function of passive section lengths,with injection currents as parameters ( $L_a= 460 \mu\text{m}$ ).

As described in section 3-2-1, the  $\Gamma_{g_o}$  value needed for computing the propagation loss,  $\alpha_p$ , was obtained from the  $\ln[ J_{th} ]$  vs.  $L_a^{-1}$  plot for these lasers with a range of different active-section lengths. The calculated value of  $\Gamma_{g_o}$  was  $37.5 \pm 2.5 \text{ cm}^{-1}$  for the nondisordered samples and  $18.9 \pm 2.5 \text{ cm}^{-1}$  for the disordered samples. These values were then used to obtain the propagation loss via Eq.(3-5).

It was assumed that the facet reflectivity  $R$  is close to that for plane-waves, i.e. 0.32. Referring to Fig. 5-10(a), the slope of the  $\ln(I_{th}/I_{th0})$  versus  $(L_p/L_a)$  curve, which is proportional to the propagation loss in the passive section, was much lower for the devices in which the passive section had undergone QW intermixing (disordering) than for devices with a non-disordered passive section. While the average propagation loss at the lasing wavelength for devices with nondisordered passive sections was estimated to be  $13 \text{ cm}^{-1} \pm 0.6$  ( $56 \pm 2.6 \text{ dB/cm}$ ), the propagation loss in the passive waveguide section for devices which had been disordered was greatly reduced to  $2.4 \pm 0.6 \text{ cm}^{-1}$  ( $10.3 \pm 2.6 \text{ dB/cm}$ )[9]. The error in this data was calculated by taking account of the uncertainty,  $\pm 2 \text{ mA}$ , in the estimation of the threshold current.

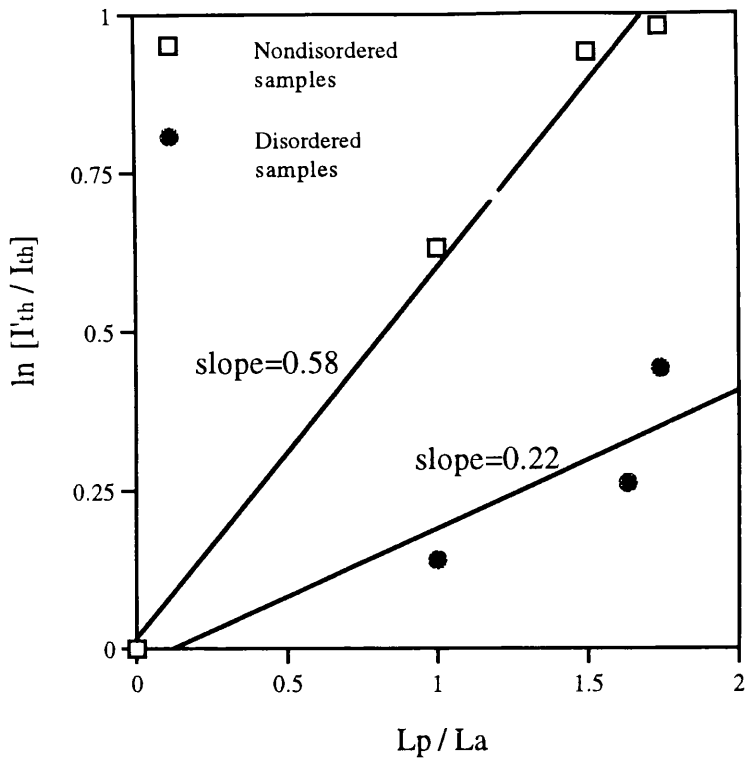
The lasing wavelength shift is defined as the difference of the lasing peak wavelength between the extended cavity ( $L_p > 0$ ) and the solitary ( $L_p = 0$ ) lasers. The red shift of the wavelength peak (as shown in Fig.5-10(b)), resulting from gain-loss competition in the composite structure, was less than 3-nm for the disordered sample with a 1-mm-long passive section, compared with a shift of 7-nm for the nondisordered laser with the same active and passive section lengths.

### ***B. From the extended-cavity oxide stripe lasers.***

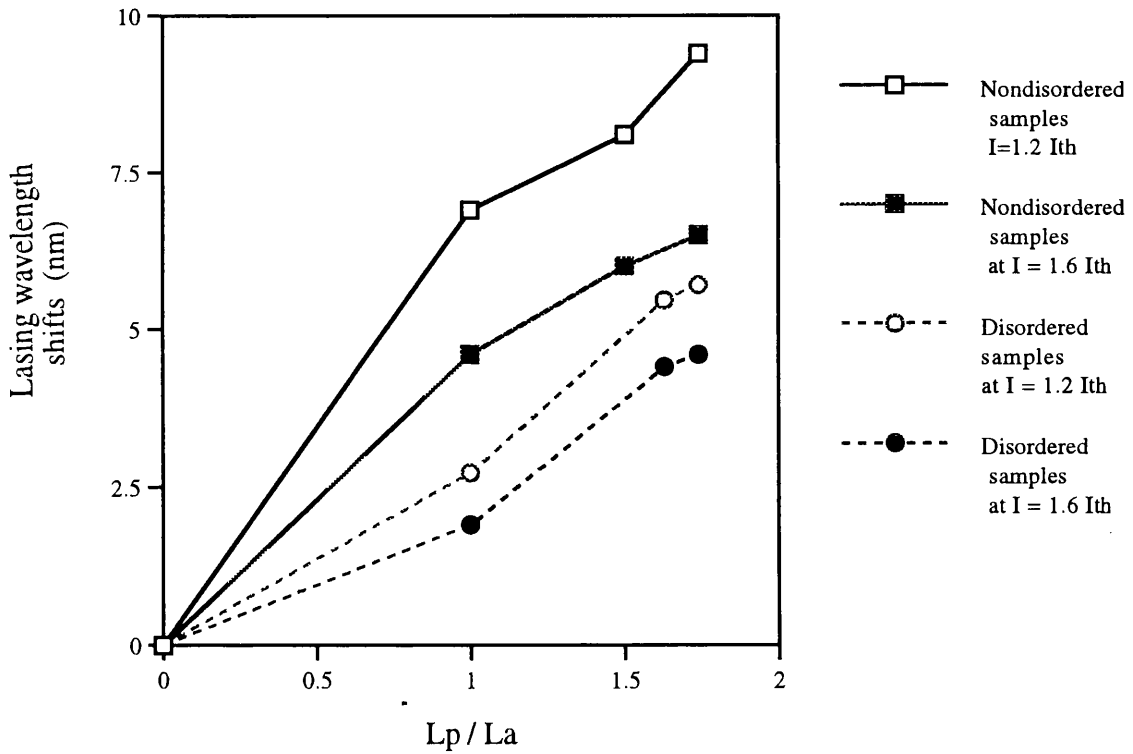
The disordered samples were annealed in a rapid thermal annealer (RTA) at  $930^\circ\text{C}$  for 60 seconds. The rise and fall times in the annealing cycle were 6 and 30 seconds respectively. Samples were face down with a single GaAs proximity cap underneath. The relative PL shift was 11.5 nm, from 808 nm to 796.5nm, as shown in table 5-2.

Before calculating the propagation loss,  $\Gamma_{g_o}$  was obtained from the  $\ln[ J_{th} ]$  vs.  $L_a^{-1}$  plot for these lasers with different active-section lengths. The calculated value of  $\Gamma_{g_o}$  was  $24.7 \pm 3.1 \text{ cm}^{-1}$  for the nondisordered samples and  $23.1 \pm 3.1 \text{ cm}^{-1}$  for the disordered samples

By using the same evaluation method as above, the propagation loss was calculated from the slope of the curve in Fig.5-11(a). The average propagation loss for disordered samples was  $5.1 \text{ cm}^{-1}$  (i.e. 22 dB/ cm), compared to  $14.3 \text{ cm}^{-1}$  (i.e. 61.5 dB/cm) for nondisordered samples at lasing wavelengths.

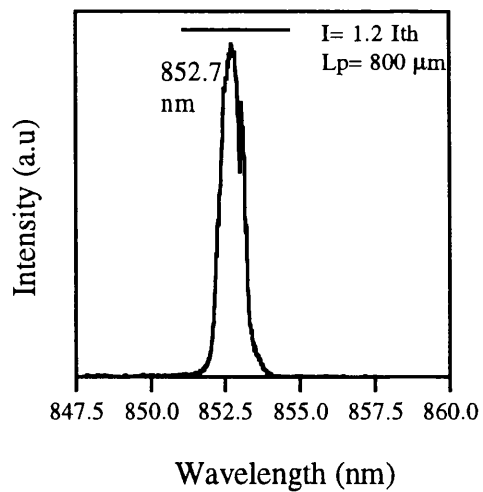
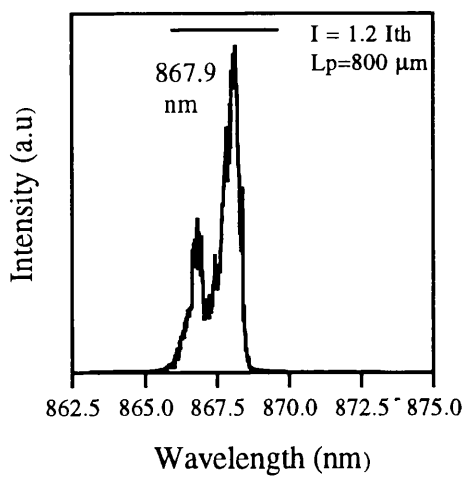
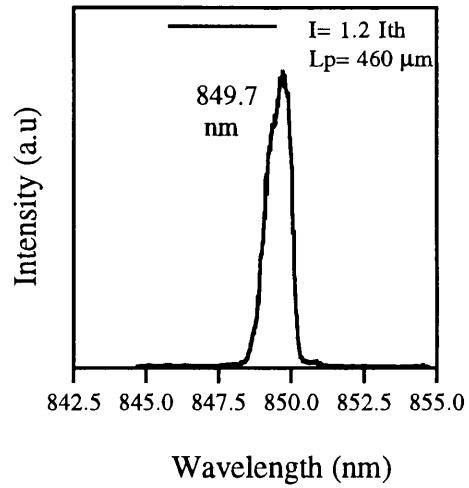
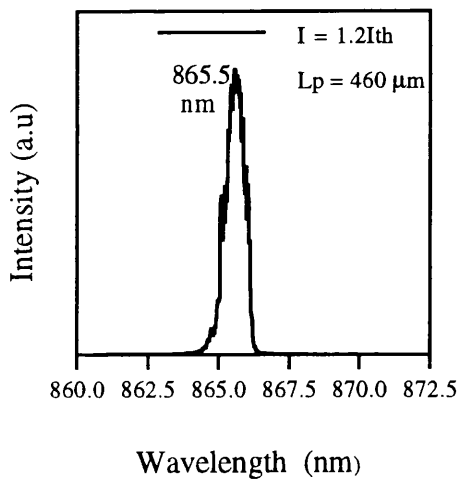
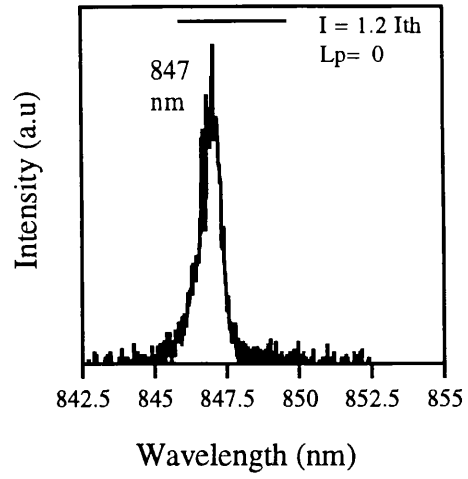
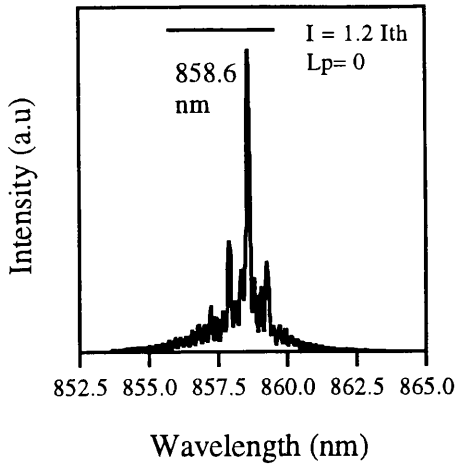


(a)



(b)

Fig.5-11 (a)Threshold current change and (b) lasing wavelength shifts of extended-cavity oxide-stripe lasers as a function of passive section lengths, with injection currents as parameter ( $L_a = 460 \mu\text{m}$ ).



(a)

(b)

Fig.5-12. Lasing spectra of (a) nondisordered, and (b) disordered extended-cavity oxide stripe lasers with varying passive section lengths ( at  $T = 20^\circ C$  ). Note that the spectra were shown with 1 to 2 nm per division to observe the details.

As to the wavelength shifts of the samples operated at  $1.2 I_{th}$  (Fig.5-11(b)), it was found that the wavelength was red-shifted by 9.3 nm for the nondisordered samples with  $L_p = 800 \mu\text{m}$ , compared to 5.7 nm for the disordered samples with the same passive section length. Fig.5-12 demonstrates the lasing spectra for both disordered and nondisordered lasers at  $1.2 I_{th}$  injection level with varying cavity lengths.

It should be noted that the minimum resolution, 0.1 nm, of spectrum analyzer was used for the above wavelength-shift measurement.

## 5-7 Discussion

### 5-7-1 On extended-cavity ridge waveguide lasers

#### A. Propagation losses

The total propagation loss in the passive waveguide section can be expressed as [11]

$$\alpha_p = \alpha_{b-b} + \Gamma\alpha_{fc} + (1 - \Gamma)\alpha_{fc,con} + \alpha_s + \alpha_c \quad (5-1)$$

where  $\alpha_{b-b}$ ,  $\alpha_s$  and  $\alpha_c$  are band-to-band, scattering, and evanescent coupling losses respectively.  $\alpha_{fc}$  and  $\alpha_{fc,con}$  are the free-carrier absorption constants in the active and the confining layers respectively. The free-carrier absorption in the active layer, i.e. the second term in (5-1), must be less significant than that of the confining layers (the third term in (5-1)) because the active layer is undoped and most of the evanescent field will couple into the cladding layers. The theoretical value of the confinement factor for a DQW structure with a well thickness of 10 nm is as low as 0.06 [1]. When the doping density of the cladding layer is  $5 \times 10^{17} \text{cm}^{-3}$ , as in our samples, the free carrier absorption in the passive section should be less than  $2 \text{ cm}^{-1}$  (8.6 dB/cm) [12].

Hunsperger [13] has pointed out that the surface scattering losses of semiconductor waveguides are typically not important, compared to the band-to-band and free carrier contributions to the absorption. By using a quantum well intermixing probe, a damage depth of 10 nm in conventional RIE etched regions was found by Ooi et al [7]. This conventional RIE was carried out at DC bias of -350 V with a  $\text{SiCl}_4$  flow rate of 9 SCCM and an RF power of 100 Watts. In the present work, MCP RIE was used. The DC bias and RF power were significantly lower at -210 V and 40 Watts respectively. The flow rate was 15 SCCM for  $\text{SiCl}_4$  and 1 SCCM for  $\text{O}_2$ . The presence of oxygen in this process provided very good sidewall smoothness and verticality (Fig.5-4). Sidewall damage, assessed by measuring the conductance of etched wires with different widths ranging from 50 to 500 nm, was estimated to be below 3 nm [5]. Table 5-3 lists the etching parameters for the comparison between conventional RIE and

MCP RIE. This novel etching technique yields low geometrical and electrical damage, which would contribute to a very low ridge sidewall-scattering loss as expected [6].

Table.5-3. Comparison between RIE and MCP RIE

Items	RIE [7]	MCP RIE [5]
1.Reactive gases	SiCl <sub>4</sub> / 9 SCCM	SiCl <sub>4</sub> / 15 SCCM, O <sub>2</sub> / 1 SCCM
2.DC bias (v)	-350	-210
3.RF power	100	40
4.Damage thickness (nm)	10	3

Since the thicknesses of the upper and the lower cladding layers were 1.2  $\mu\text{m}$  and 1.5  $\mu\text{m}$  respectively, the penetration of the evanescent field outside those layers could be neglected (analyzed in section 5-3) [3]. If the free-carrier absorption resulting from the carrier diffusion and spreading into the guiding layers of the unpumped waveguide section was subtracted further, the propagation losses in the passive waveguide section should be even lower than the measured value of  $2.4 \pm 0.6 \text{ cm}^{-1}$  ( $10.3 \pm 2.6 \text{ dBcm}^{-1}$ ). This value was comparable to the loss of  $0.84 \text{ cm}^{-1}$  ( $3.6 \text{ dB.cm}^{-1}$ ) which was the *lowest* previously reported, and to  $2.33 \text{ cm}^{-1}$  *typical* ( $10 \text{ dB.cm}^{-1}$ ) for lasers made by the same technique [14]. For similar work using the IID technique, the lowest propagation loss using the neutral impurity, fluorine, as an implant is  $2.4 \text{ cm}^{-1}$  ( $10.3 \text{ dB.cm}^{-1}$ ) [15]. The lowest loss reported for comparable DQW devices fabricated by silicon IID is  $11 \text{ cm}^{-1}$  ( $47.3 \text{ dB.cm}^{-1}$ ) [16].

It was thought that the reasons for obtaining such low waveguide losses are three-fold. Firstly, the absorption edge of the passive section was greatly blue-shifted away from the emission peak of the active region, so that the residual bandtail-absorption was not significant. In addition, because impurity-free vacancy induced diffusion (IFVD) was used, the free-carrier absorption loss should be low as well. This was clearly confirmed by the  $\ln [I_{\text{th}}/I_{\text{th0}}]$  versus  $(L_p/L_a)$  curve as shown in Fig.5-10(a), since its slope is proportional to the propagation loss (Eq.3-5). From this, we found that when  $L_p$  is as long as 2.74 times  $L_a$ , i.e. 1.2 mm, the threshold current was only increased by 30 %. Secondly, the MCP RIE process gave smooth and vertical sidewalls as well as a thin damage layer, implying low sidewall scattering losses. Thirdly, good quality MBE grown material was used in these devices.

### B. Lasing wavelength shifts in the composite DQW structure

As mentioned in section 3-2, carrier injection induces wavelength shifts due to

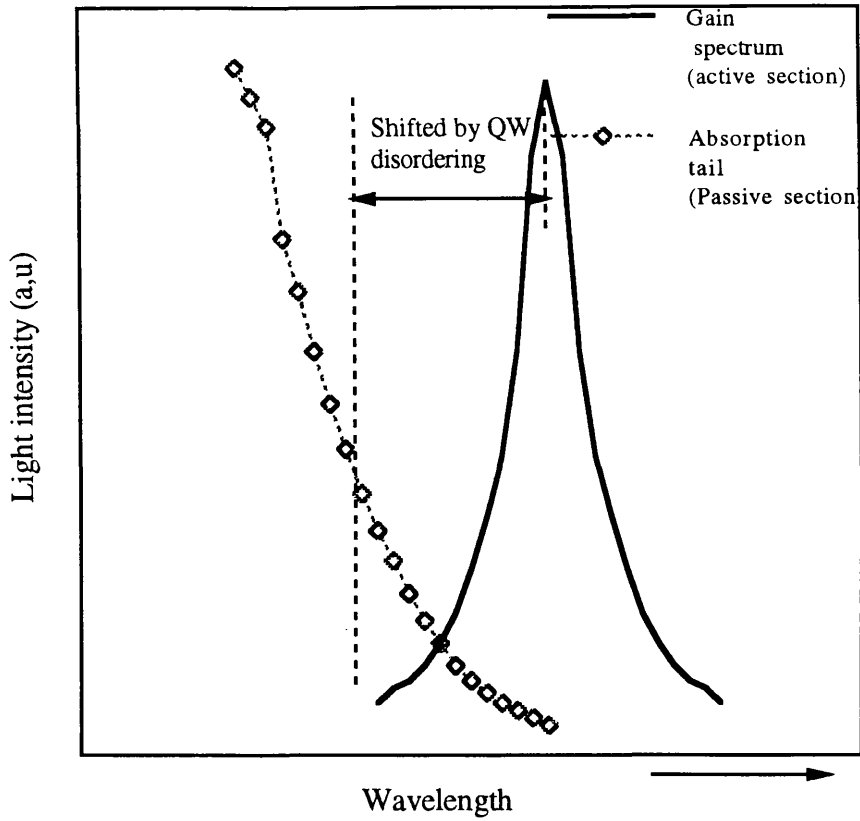


Fig.5-13. Schematic diagram of the gain-loss competition in an extended (or composite) cavity laser diode.

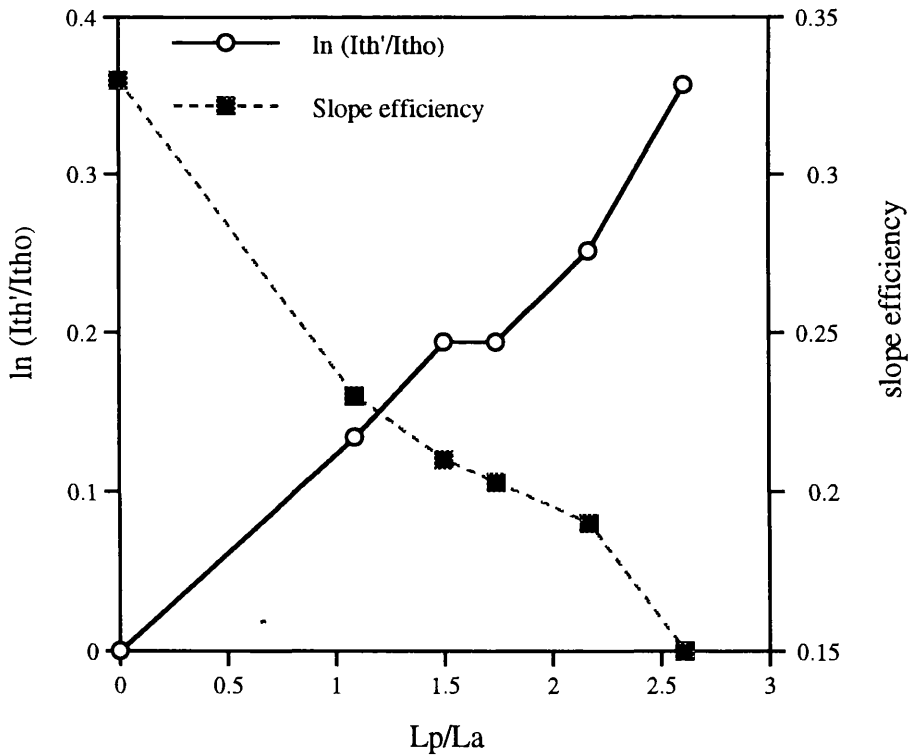


Fig.5-14. The slope efficiency and the threshold current variations of extended cavity lasers as a function of passive section lengths ( $L_a = 460 \mu\text{m}$ ).

bandgap narrowing and band-filling effects. For a composite laser structure, any red shift introduced by the gain-loss competition is very important for possible exploitation of such lasers in OEICs and PICs.

A detailed study of the emission wavelength detuning as a function of the passive waveguide length for extended cavity DQW lasers fabricated using dielectric cap disordering has been carried out. Fig.5-10(b) shows that only a 3 nm red shift was obtained for the composite structure with a 1.46 mm-long total cavity length, compared with some 7 nm for the nondisordered sample with the same cavity dimensions.

From Fig.5-13, with larger  $L_p$  the losses in the passive section form a higher fraction of total losses, and so the red shift is larger. If the absorption edge of the passive waveguide is shifted further away from the emission peak wavelength of the active section, the passive section absorption loss, which is determined to a significant extent by the overlap of the gain and absorption curves, will be lowered and the wavelength detuning, i.e.the red shift, is therefore smaller.

A detailed model of the material and device properties is required to predict the above red shift more precisely. Obviously, the variation of absorption losses between the active and passive sections, the gain-current and gain-wavelength relations of the active section and even the optical power reflection when the bandgap shift is large should be taken into account in the model.

The lasing wavelength red-shifts as threshold current is increased to overcome the additional losses of greater passive section lengths. Since increased current density would blue-shift the emission wavelength, the observation of red-shifting indicates that gain-loss competition principally determines the lasing wavelength (see Fig.5-10(b)).

Furthermore, for the DQW composite structure disordered by this technique, the bandgap was widened by some 40 meV. By using the well-known approximate relation of  $n \propto (1/E_g)$ , where  $n$  and  $E_g$  are the refractive index and bandgap energy respectively, the fractional power reflection is 0.0002, calculated under a plane-wave approximation. Experimentally, we obtained  $\kappa$  from Fig.5-10(a) as unity with an error of 0.001, confirming that the optical power reflection due to the bandgap jump at the boundary of the disordered and the nondisordered regions was negligible.

### *C. Slope efficiency*

Slope efficiency is defined as the ratio of the change in the emitted power per facet to the change in the injected current. Equation (3-5) indicates that  $\ln[I_{th}/I_{th0}]$  is proportional to the ratio  $(L_p/L_a)$  and this has been verified in Fig.5-10. As the cavity length increases through increases in the passive section length, the absorption loss makes an increasingly large contribution to the total loss. The slope efficiency undergoes a corresponding decrease, as shown in Fig. 5-14.

### 5-7-2 On extended-cavity oxide stripe lasers

For the sample disordered at 930 °C for 60 seconds, the differential PL shift is 11.5 nm, which is low probably simply because the SrF<sub>2</sub> layer was evaporated without removing the native oxide on the GaAs surface beforehand. The presence of native oxide did suppress the QW intermixing as detailedly depicted in section 4-6 [9].

The variation of propagation losses as a function of ( $L_p / L_a$ ) is very similar to that for ridge waveguide lasers. For the samples disordered with PL shift of 11.5 nm, the average propagation loss was reduced to 5.1 cm<sup>-1</sup> (21.9dB/cm), compared to 14.3 cm<sup>-1</sup> (61.5 dB/cm) for the nondisordered samples. In addition, the lasing wavelength was red-shifted by 5.7 nm for the disordered sample with 800- $\mu$ m passive section length, compared to 9.3 nm for the nondisordered sample with the same geometry size.

However, the lasing wavelength shifts due to carrier injection for these two lasers are different. Since the ridge waveguide lasers were operating in a strongly index-guiding regime, the carrier-induced wavelength shifts due to the change in current injection are relatively smaller than those from gain-loss competition ( see Fig 5-10). Conversely, for the gain-guided oxide stripe lasers with the same cavity length, heavier carrier injection induces a larger blue shift and makes the overall wavelength red-shift smaller. Tomita et al [17] computed the lasing wavelength as a function of the threshold current density for QW laser diodes, from which it was estimated that the threshold carrier density of this laser is around  $3.5 \times 10^{18} \text{ cm}^{-3}$  at wavelength of interest. With the carrier density of  $5.6 \times 10^{18} \text{ cm}^{-3}$  at 1.6 I<sub>th</sub>, it is believed [17] that the band-filling effect will be dominant over the bandgap narrowing effect (see section 3-2), and was responsible for this blue-shifting. However, considering all of the above mechanisms, the red-shifting of the lasing wavelength strongly indicates that the red shift from gain-loss competition in the composite structure still principally determines the lasing wavelength of an extended-cavity laser diode.

### 5-8 Summary

By using dielectric cap disordering and MCP reactive ion etching, DQW extended cavity ridge waveguide lasers with very smooth and low-damage sidewalls were successfully fabricated. The dielectric cap disordering process, i.e. IFVD, selectively widened the bandgap in the passive ridge waveguide section, and afforded a very low propagation loss of  $2.4 \pm 0.6 \text{ cm}^{-1}$  ( $10.3 \pm 2.6 \text{ dB/cm}$ ), compared to  $13 \pm 0.6 \text{ cm}^{-1}$  ( $55.9 \pm 2.6 \text{ dB/cm}$ ) or nondisordered samples at the lasing wavelength in the passive ridge waveguide section. In addition, the red shift arising from gain-loss competition in the composite structure was measured accurately. The lasing wavelength was red-shifted by 3 nm for the disordered sample with a 1-mm long passive section

length, compared to 7 nm for the nondisordered laser with the same geometry size. The requirements for making these lasers were analyzed in detail, and some important factors, e.g. native oxide effects, affecting the QW intermixing and device fabrication were described and taken into account.

For the gain-guided oxide stripe lasers with a differential PL shift of 11.5 nm, the average propagation loss for disordered samples was  $5.1 \pm 0.6 \text{ cm}^{-1}$  ( $21.9 \pm 2.6 \text{ dB/cm}$ ), compared to  $14.3 \pm 0.6 \text{ cm}^{-1}$  ( $61.5 \pm 2.6 \text{ dB/cm}$ ) for nondisordered samples at lasing wavelengths. As for the lasing wavelength shift, the lasing peak wavelength is significantly current-sensitive in addition to the influence from gain-loss competition in the composite structure. The lasing wavelength is red-shifted by 5.7 nm for the disordered sample with a passive-section length of 800  $\mu\text{m}$ , compared to 9.3 nm for the nondisordered sample with the same cavity dimensions at a drive current of 1.2  $I_{th}$ .

For both gain-guided and index-guided lasers, it was found that dielectric cap disordering not only greatly reduced the propagation losses, but also effectively decreased the red shift due to gain-loss competition. In particular, the disordered composite ridge waveguide lasers demonstrated here showed very small wavelength detuning of the red shift as the passive-section length was increased. All of these attributes confirm that these fabrication techniques can be employed to realise high performance DQW composite laser devices which could play an important role in PICs or OEICs.

## 5-9 References

- [1] Arakawa, Y. and Yariv, A., 'Theory of gain, modulation response, and spectral linewidth in AlGaAs quantum well laser diodes', pp.1666-1674, V-21, No.10, IEEE J Quantum Electron 1985
- [2] Mendez, E.E. and Klitzing, K V, '*Physics and applications of quantum wells and superlattices*', p.159, NATO ASI series, Plenum Press, New York, 1988.
- [3] Casey, H.C, and Panish, M.B, 'Influence of  $\text{Al}_x\text{Ga}_{1-x}\text{As}$  layer thickness on threshold current density and differential quantum efficiency for GaAs- $\text{Al}_x\text{Ga}_{1-x}\text{As}$  DH lasers ', V-46, No.3, pp.1393-1395, J Appl. Phys. 1975
- [4] Ooi, B.S. 'Fabrication of optoelectronic integrated circuits using quantum-well intermixing', PhD thesis, Glasgow University, 1994
- [5] Song, Y.P., Wang, P.D., Torres, S.C.M., and Wilkinson, C.D.W. 'Magnetically confined plasma reactive ion etching of GaAs/AlGaAs/AlAs quantum nanostructure', B.12(6), pp.1-5, J Vacuum Science Tech., 1994
- [6] Austin M.W. , 'GaAs / GaAlAs curved rib waveguides', pp.795-800, V.18, No.4, IEEE J Quantum Electron ,1982.

- [7] Ooi, B.S, Bryce, A.C., Wilkinson, C.D.W.and Marsh, J.H. 'Study of reactive ion etching-induced damage in GaAs/AlGaAs structures using a quantum well intermixing probe', 64(5), pp.598-600, Appl. Phys. Lett., 1994
- [8] Pang, S.W.and Ko, K.K,J Vac. Sci. Technol. B10, 2703, 1992
- [9] Yee, H.H, Ayling, S., De La Rue, R.M., Vögele, B., and Song, Y.P., 'Fabrication of high performance extended cavity double-quantum-well lasers with integrated passive sections', accepted for publication. IEE Proc.,Part J *Optoelectronics*, 1996.
- [10] Agrawal, G.P.: 'Lateral analysis of quasi-index-guided injection lasers: Transition from gain to index guiding', V.LT-2, No.4, pp.537-543, IEEE J.Quantum Electron., 1984
- [11] Casey, H.C., and Panish, M.B., '*Heterostructure Lasers*', Section 3.8, Part A, New York, Academic Press, 1978
- [12] Thompson, G.H.B.: '*Physics of Semiconductor Laser Devices* ', Section 5.2.1, P.247, New York, Wiley, 1980
- [13] Hunsperger, R.G.: '*Integrated Optics: Theory and Technology* ', Section 5.1, Springer-Verlag, Berlin, 1991
- [14] Gontijo, I., Krauss, T., De La Rue, R.M, Roberts, J.S, and Marsh, J.H.: 'Very low loss extended cavity GaAs/AlGaAs lasers made by impurity-free vacancy diffusion', V- 30, No.2, pp.145-146, Electron. Lett. 1994
- [15] O'Neill, M., Marsh, J.H., De La Rue, R.M., Roberts, J.S., Button, C. and Gwilliam, R.: 'Reduction of the propagation losses in impurity disordered quantum well waveguides', V.26, No.19, p.1613-1614, Electron. Lett. ,1990
- [16] Werner, J., Kapon, E., Stoffel, N.G., Colas, E., Schwarz, S.A, Schwartz, C.L., and Andreadakis, N.: 'Integrated external cavity GaAs/AlGaAs lasers using selective quantum well disordering', 55(6), pp.540-542, Applied Phys. Lett., 1989.
- [17] Tomita, A.and Suzuki, A.: 'Carrier-induced lasing wavelength shift for quantum well laser diodes', V-23, No.7, pp.1155-1159, IEEE J. Quantum Electron. 1987.

## Chapter 6 Deep surface gratings for distributed Bragg reflector laser diodes

### 6-1 Introduction

Gratings fabricated in an optical waveguide structure form one of the most important components for an optoelectronic integrated circuit. They can be used as passive components, such as couplers, deflectors, reflectors, wavelength filters and mode converters, providing various functional characteristics suitable for lightwave control.

In this chapter, the two-beam interference technique for fabricating gratings is described in section 6-2, followed by grating fabrication in section 6-3. The measurement of the grating periodicity is demonstrated in section 6-4.

The second part of this chapter deals with DBR lasers with deep-surface gratings. Modal analysis for the double-quantum-well material B564 is carried out in section 6-5. Section 6-6 describes the fabrication techniques for the DBR lasers. The measurements and fabrication results of the lasers are demonstrated in section 6-7, followed by the discussion in section 6-8.

### 6-2 The two-beam interference technique

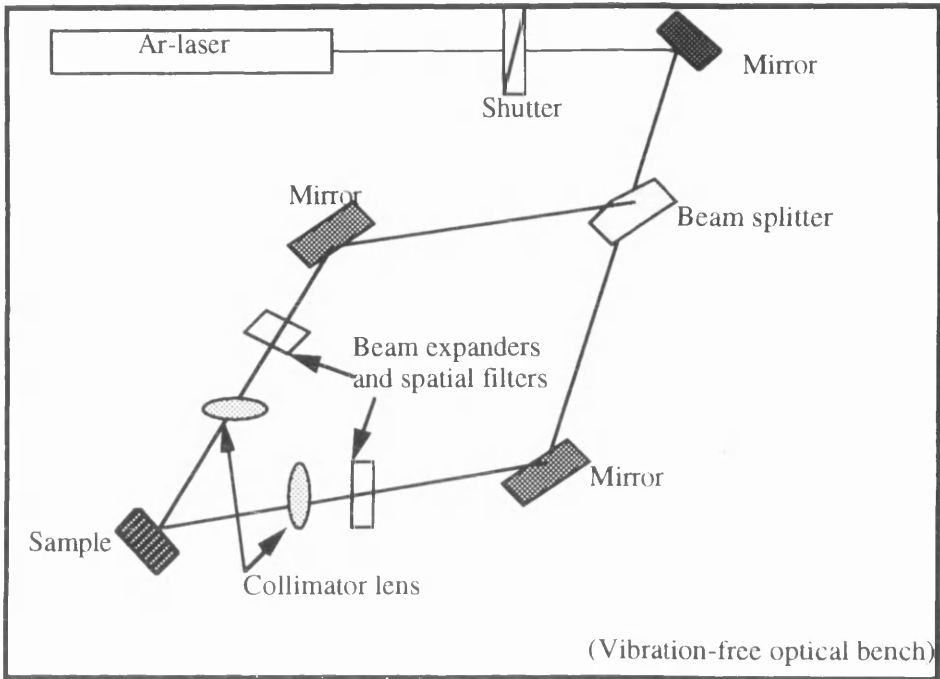
Two-beam interference (also called holographic ) lithography and electron beam lithography are the two most frequently used methods to generate grating patterns. Both have their advantages and drawbacks. The advantages of the two-beam interference technique are [1] :

1. Fabrication of small-period gratings is possible with relatively simple apparatus.
2. Fabrication of large-area gratings is relatively convenient.
3. Fabrication of variable-period, i.e. chirped, gratings is possible.
4. High uniformity in the periodicity is attainable by adjusting carefully the light paths and beam quality.

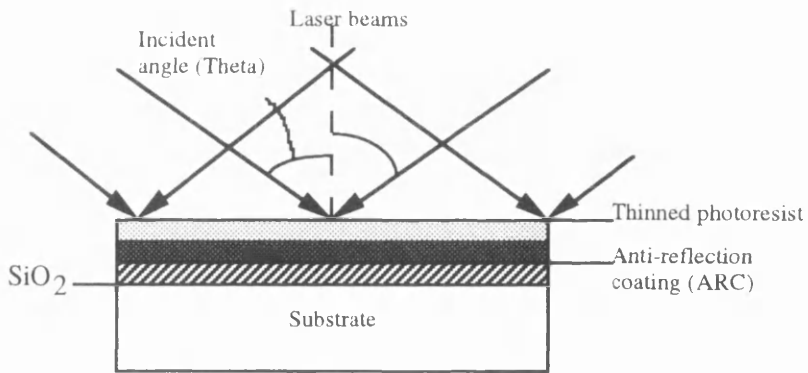
Fig.6-1 illustrates an optical arrangement used for interference lithography. If the two beams,  $I_1$  and  $I_2$ , have equal intensity and are carefully adjusted, the phase difference  $\delta$  and the lengths of the beam paths between the common source and the interference point of these two beams should be the same. In this case, the light intensity will be [2]

$$I = 4I_1 \cos^2(\delta / 2) \quad (6-1)$$

The period of the resultant interference fringe is given by [3]



(a)



(b)

Fig.6-1 (a) The set up of a two-beam interference technique .  
 (b)Two-beam pattern recording.

$$\Lambda = \frac{\lambda}{2 \sin \theta} \quad (6-2)$$

where  $\Lambda$  is the period of gratings,  $\lambda$  is the wavelength of the laser beams, and  $\theta$  is the incidence angle of the laser beam with respect to the normal of the grating plane. From Eq. (6-2), we know that shorter  $\Lambda$  can be obtained by choosing a larger incidence angle  $\theta$  or, alternatively, shorter-wavelength light source, such as a He-Cd laser, or by using a prism to reduce the wavelength incident upon the sample [1].

The symmetric interference setup has the advantage of easy re-arrangement of the angle of the incidence on the sample surface. By altering the distance between the sample and the mirrors, the grating period for device fabrication can easily be adjusted.

The laser source used for this purpose was an argon laser, labelled as Spectra Physics 165, capable of producing 4 watts CW power in all-line operation. However, the laser line chosen for this fabrication was at a wavelength of 457.9 nm with a maximum power output of approximately 200 mW.

### 6-3 Grating fabrication

The below is the details of fabricating the surface gratings for DBR lasers:

#### 1. System warm up and stabilization:

It should be noted that approximately one hour waiting time is required whenever the laser power is changed. This ensures that a stable power output (< 5% fluctuation) is produced.

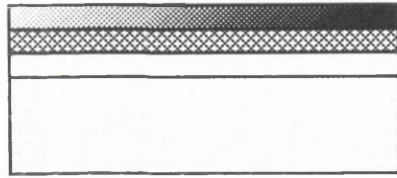
#### 2. System adjustment:

- (a) The setup should be tuned at a required wavelength for the pattern recording. The laser output has to be checked by a spectrum analyzer.
- (b) Determine the grating period and adjusting the incidence angle for the period by changing the distance between the sample and the mirror.
- (c) The two separated beams should be aligned precisely to the optical path drawn on the optical bench. If the angle of incidence is  $37.1^\circ$ , the resulting grating period is expected to be 380 nm for the exposure wavelength of 457.9 nm.

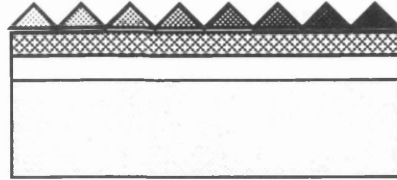
#### 3. Sample preparation (Fig.6-2(a)):

First, samples should be completely baked dry. Anti-reflection coating (ARC) was then spun on at 5000 rpm for 60 seconds. Samples should then be baked at  $130^\circ \text{C}$  for 30 minutes to dry up the moisture. A thinned resist (1part S1400-31: 2 parts Thinner) was spun-on at 4000 rpm for 30 seconds. Finally, samples were postbaked at  $90^\circ \text{C}$  and pre-exposed with a photomask for 7 seconds. Note that this preliminary lithography was used to select an area

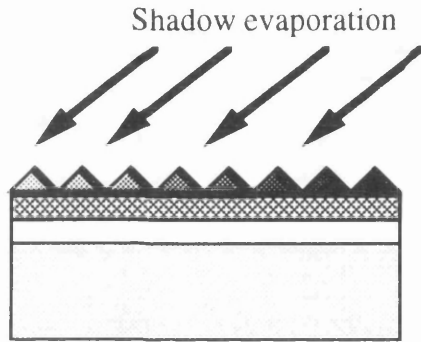
(a) After sample preparation



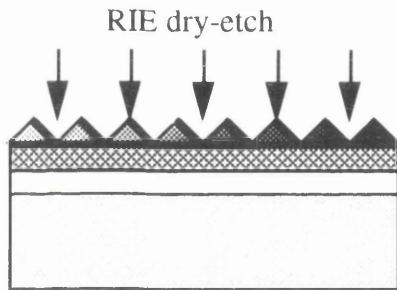
(b) The resist pattern after two-beam lithography



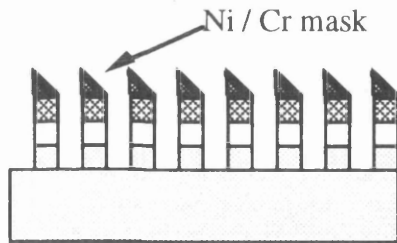
(c) Ni / Cr shadow masking



(d) Before dry-etching by  
1.  $O_2$ , 2.  $C_2F_6$ , and  
3.  $SiCl_4$  plasmas



(e) After RIE dry etching



(f) After removing the masking films

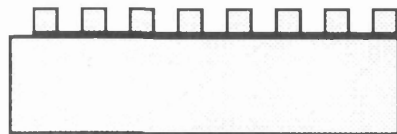


Fig.6-2 Grating fabrication processes by using two-beam interference method



for the subsequent holographic lithography.

#### 4. *Exposure test and pattern recording (Fig.6-2(b)) :*

(a) About 10 Si test samples should be prepared. They were used for an exposure test by adjusting either exposure or development time, or both. Uniform and strong reflection from an exposed sample is always required to confirm good-quality exposures for the subsequent processing.

(b) Check the resist contrast after developing a sample. It should be noted that a workable exposed pattern should have a thinned-resist with pattern of 0.4  $\mu\text{m}$  or higher. Otherwise, the exposure test should be repeated until it meets this criterion. If the resist contrast is too small, the subsequent shadow masking may fail, because the metallic film could mask all over the pattern .

(c) Real samples were then exposed, developed, rinsed and blown dry.

#### 5. *Shadow evaporation (Fig.6-2c)):*

To obtain a shadow mask for the subsequent grating etch, a shadow angle should be determined before evaporation. The shadow area was covered by Ni / Cr film ( 90% of Ni ) with thickness around 15 nm.

The shadow angle should be precisely determined and adjusted before evaporation in order to obtain an appropriate mark / space ratio. Streifer et al [4] showed that the coupling coefficient can be maximized if a 50 % duty cycle is achieved for third-order gratings. In other words, the width of the grating tooth must be equal to the width of the grating trench for this case.

#### 6. *Grating formation:*

$\text{O}_2$ ,  $\text{C}_2\text{F}_6$ , and  $\text{SiCl}_4/\text{SiF}_4$  plasmas were used to dry-etch ARC and resist, silicon dioxide, and GaAs respectively. The detailed recipes are shown in table 6-1. Since the silica was encapsulated by ARC and resist,  $\text{O}_2$  plasma was used to remove the covering organics. A little over-etching does no harm, but ensures a clear etch-window for the subsequent silica etch. After transferring the grating pattern to the silica, GaAs was then etched by a plasma with mixed gases of  $\text{SiCl}_4$ (8 SCCM) and  $\text{SiF}_4$  (1 SCCM). The grating etch step should be precisely controlled to gain a proper coupling coefficient for a Bragg reflector or a grating coupler.

#### 7. *Removal of covering films:*

Cleaning off the covering films on the gratings is time-consuming. The details are as follows:

##### (a) Removal of Ni / Cr film:

The sample was immersed into diluted acid 1part HCl (36.5%): 1 part RO water for 1-2 minutes. Check if the masking metallic film is fully gone.

Table 6-1. RIE recipes for a grating etch

Gas	Pressure (mTorr)	Bias (volts)	Forward rf power (W)	Etch time (min)	Gas flow (SCCM)
O <sub>2</sub>	12	440	75	3.5	13
C <sub>2</sub> F <sub>6</sub>	12	460	100	6	20
SiCl <sub>4</sub> / SiF <sub>4</sub> (*)	12	110	25	8	8/1

(\*) The etch rate is 50 nm/min for the grating with period of 380 nm.

(b) ARC and photoresist removal

Boil ARC and resist on samples with an N-MP solution in a reflux system in an electric oven. Turn the power off once the solution is boiling and let it cool down for about one hour.

(c) Completely clean samples by using a reflux unit. Change the organic solvent in the order of N-MP, methanol, acetone, and then rinse it in a RO water for at least 2 minutes.

(d) Removal of the SiO<sub>2</sub> layer:

Using diluted HF acid (4:1) to etch away the silica layer for 30 seconds. Rinse samples and bake dry.

**6-4 Grating-period measurement**

By using Littrow's mounting [5], as shown in Fig.6-3, a collimated beam from a slit source S is incident on the reflection gratings G, and the images of S formed by the diffracted rays are observed on the focal plane of the lens. A rotating angle-measurement unit indicates the diffracted angle  $\theta_m$  for the  $m^{\text{th}}$  order.

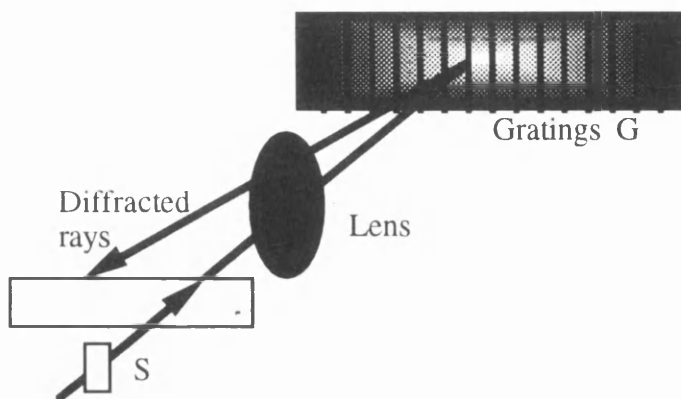


Fig.6-3 Schematic diagram of the Littrow's mounting

In the Littrow condition, the grating period  $\Lambda$  can be determined by Eq. (6-3) with an accuracy of  $(\delta\Lambda / \Lambda)$  [6]:

$$\Lambda = \frac{m\lambda_o}{2\sin\theta_m} \quad ; \quad \left| \frac{\delta\Lambda}{\Lambda} \right| = \frac{\partial\theta_m}{\tan\theta_m} \quad (6-3)$$

where  $m$  is the grating order.

Table 6-2 shows the results for these measurements. It was found that the accuracy of periodicity measurement ranged from  $\pm(0.014-0.041)$  nm. These results indicate that gratings with a high-precision periodicity can be made, if the angle of incidence is properly determined and aligned.

Table.6-2 Grating-period measurement by Littrow's mounting.

Wavelength (nm)	$\theta_{ref}$ (degrees)	$\theta_1$ (degrees)	$\theta_m = \theta_1 - \theta_{ref}$ (degrees)	Period $\Lambda$ (nm)	$\Delta \Lambda$ (nm)
488	275.5	314.38	38.88	389	0.041
457.9	275.5	311.50	36.00	389	0.014

## DEVICE IMPLEMENTATION

### (DBR laser diodes)

#### 6-5 Modal analysis of the waveguide structure

The asymmetric waveguide structure B564, designed by S.Ayling and grown by B.Vögele, is shown in Table 6-3. It is used to fabricate the DBR lasers for this work. It is well known that deep gratings give large coupling coefficient for the reflection gratings[4]. Practically, however, vertical and smooth gratings are not easily fabricated, if the gratings are deep. One of the solutions to the problem of obtaining the sufficient coupling is to confine the optical field so that most of the field presences well above the QW layers and within the ridge region - hence increasing the optical power reflection. The emitted light would then be perturbed significantly by the corrugations without the gratings needing to be etched very close to the waveguide core.

Fig.6-4 demonstrates the TE<sub>00</sub> modal contours of this structure, where the ridge is 0.6  $\mu\text{m}$  high and 0.2  $\mu\text{m}$  away from the QW layer. Compared to the symmetric field contours shown in Fig.5-1, more optical field was found to couple into the upper guiding layers and within the ridge waveguide region.

Fig.6-5 demonstrates the modal distributions for the above DQW structure [7].

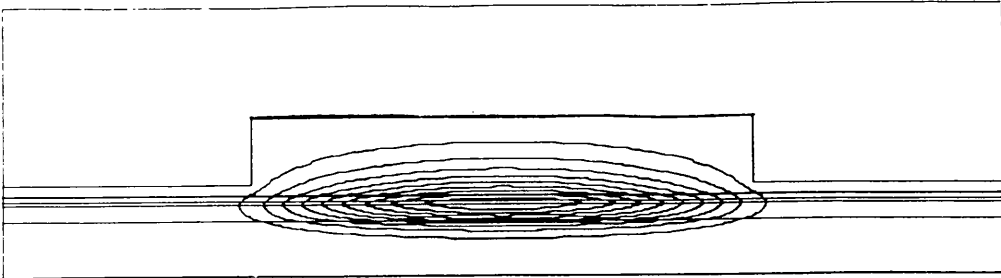


Fig.6-4 Electric field contours of  $TE_{00}$  mode of the asymmetric DQW B564. ( From the outermost contour inward: 1 %, 10 %, 20 %, 30 %, 40 %, ..... etc. )

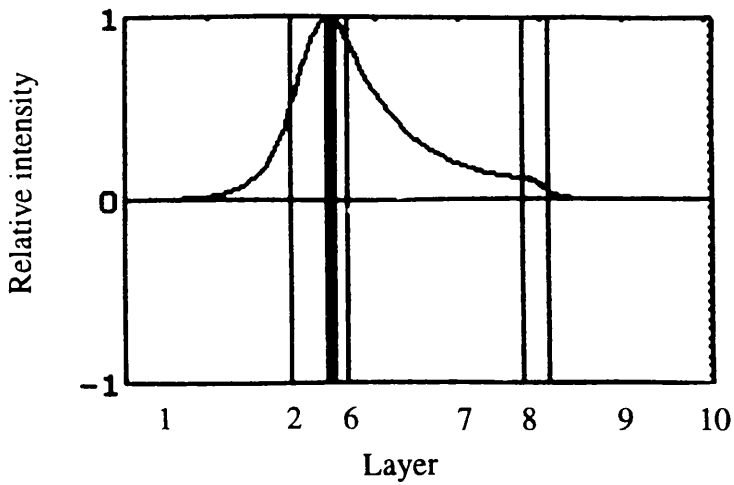


Fig. 6-5 The modal distribution of the  $TE_{00}$  mode of the above structure[7]. The rightmost layer is air and the leftmost layer is the lower cladding layer.

Fig.6-6(a) shows the refractive indice of each layer for this structure. From the simulation of this structure, the modal power fraction for each layer in this structure was computed. Fig.6-6(b) demonstrates the optical power fraction (to the total propagating power) of the fundamental mode distribution. It is found that 54% of the power fraction is in the upper guiding layers and 38 % is in the lower guiding layers. It is evident that more light is coupled into the surface gratings for this asymmetric structure, than for a similar but symmetric DQW structure.

Table 6-3.The asymmetric DQW structure B564

Layer	Thickness (nm)	Material / Al fraction	Concentration (cm <sup>-3</sup> )	Purpose of layers
Sub	-	GaAs	N <sup>++</sup> 5E18	Contact layer
0	500	GaAs	N <sup>+</sup> 2E18	Buffer
1	500	AlGaAs / 0.79	N 5.5E17	Lower cladding
2	142	AlGaAs / 0.20	Undoped	QW barrier
3	8	GaAs	Undoped	Q W
4	8	AlGaAs	Undoped	QW barrier
5	8	GaAs	Undoped	QW
6	52	AlGaAs / 0.20	Undoped	QW barrier
7	700	AlGaAs / 0.40	P <sup>+</sup> 1E18	Upper cladding
8	100	GaAs	P <sup>++</sup> 5E18	Contact layer

(Note): Excitonic peak= 791 nm ( at 77° K)

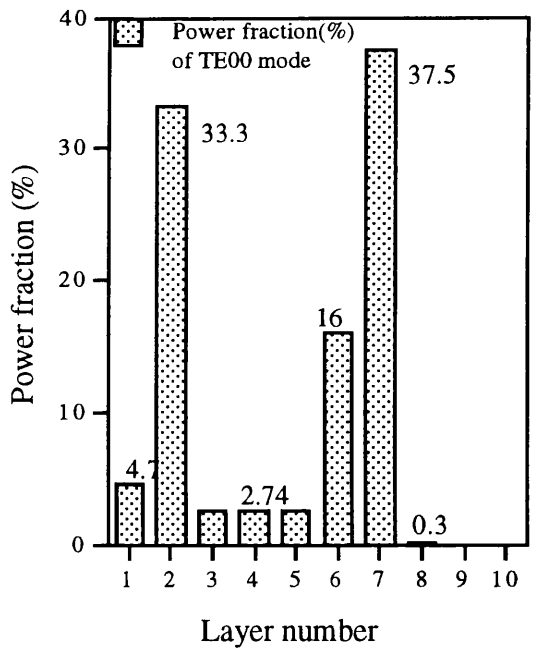
Fig.6-7 is the micrograph of the photoresist pattern generated by the two-beam interference technique. The grating profile after the GaAs RIE process is shown in Fig.6-8, in which the masking layers, including the SiO<sub>2</sub>, ARC and Ni / Cr films, were not removed.

## 6-6 Fabrication of the DBR lasers

In much of the previous work on this topic, e.g.[9], the ridge waveguide was etched first and the holographically-defined surface gratings were then formed on the passive ridge waveguide section. For the deep surface-grating fabrication of this work, the above process cannot yield the high-performance gratings required for DBR mode selection, mainly because the anti-reflection coating and photoresist film cannot sit homogeneously on the rib. In consequence the grating uniformity and etched profiles were very poor when this approach was tried. In order to solve the problem, an alternative technique was exploited, in which the grating pattern was first defined on the

Layer	1	2	3	4	5	6	7	8	9	10
n (Index)	3.08	3.45	3.66	3.45	3.66	3.45	3.32	3.65	1.0	
Thickness (nm)	500	140	8	8	8	52	700	100	(Air)	
			(QW)		(QW)					

(a)



(b)

Fig.6-6(a) The refractive indice [8] and the thicknesses of the asymmetric DQW structure B564.  
 (b) The optical power fraction of each layer for the mode TE<sub>00</sub>, in which the layer numbers are the same as those of Table 6-2.

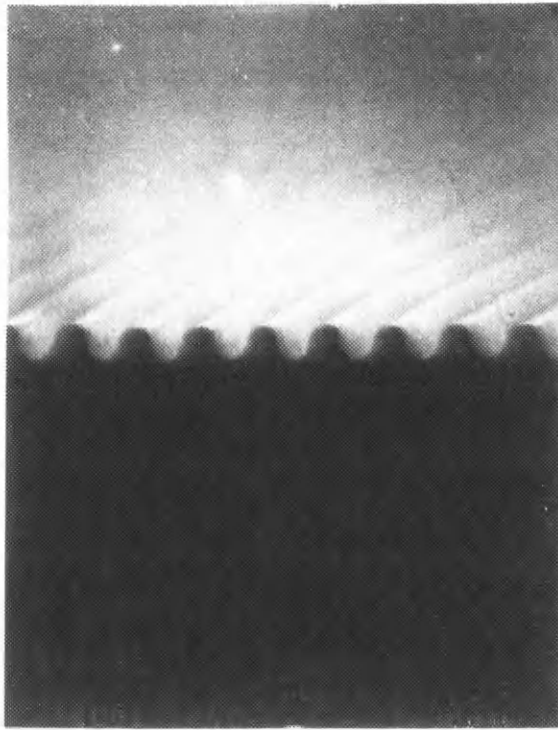


Fig. 6-7 SEM micrograph of the photoresist pattern with period 380 nm.

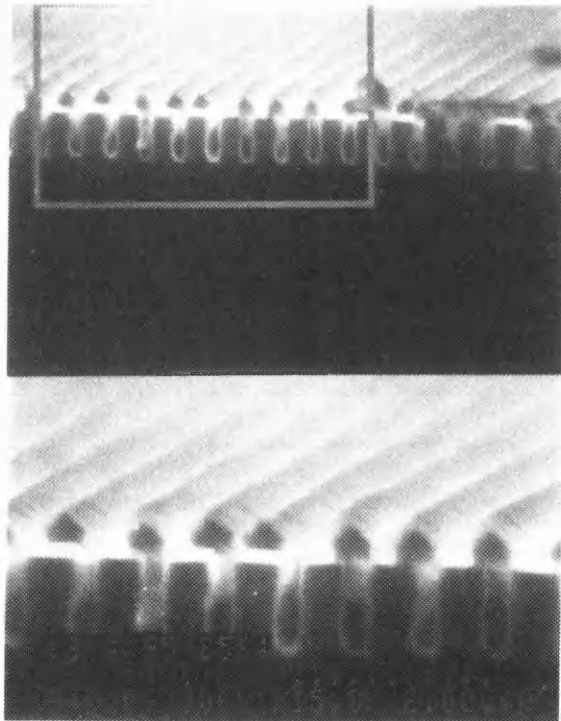


Fig.6-8 SEM micrographs of the pattern after GaAs etching (The masking layers were not removed)

sample (see below) and the ridge waveguide was then formed by a conventional RIE process. From the experimental results shown in section 6-7, it is clear that this fabrication technique is very effective, especially for fabricating deep surface gratings.

Fabrication of a DBR laser with deep surface gratings is, typically, a lengthy and complicated process. The fabrication processes are as follows:

1. Sample cleaning and QW disordering, if required, are the same as those in chapter 5.

2. Grating fabrication :

The grating pattern recording, the removals of photoresist, ARC and then the silica etch are the same as those in the previous section.

Before etching off the GaAs contact layer, two precise mask patterns must be made as the following:

- (a) Use photoresist S1400-17 to define and open the ridge region.

- (b) Use reversing photoresist AZ5214E to define and then open the passive section for the subsequent grating etch.

Carefully align the above patterns, and select the gratings in the passive region to be RIE-etched. After this, any encapsulating layer, including the silica, above the gratings should be fully cleaned off by the procedure stated in section 6-3.

3. Silica deposition (200 nm) by PECVD for the subsequent ridge etch.

4. Formation of the ridge:

The same as those of section 5-5.

5. Removal of the contact layer in the passive section:

Stripe off the silica mask and remove the P<sup>+</sup> contact layer as the steps in section 5-5.

6. Follow the same procedures as those in section 5-5 to finish the rest of the fabrication.

Fig.6-9 is the schematic diagram of a DBR laser with deep surface gratings. The ridge waveguide was etched by 4.5  $\mu\text{m}$  wide and 0.6  $\mu\text{m}$  high, which was 0.2  $\mu\text{m}$  away from the DQW region.

## 6-7 Measurements and fabrication results

### 1. *L-I curves and far-field pattern*

In order to display clearly the spontaneous emission spectrum, the current pulses were adjusted to be 5  $\mu\text{s}$  wide and the repetition rate was 3 KHz. The duty cycle was raised to (1/66) in order to increase the signal-to-noise ratio below threshold. The small noise fluctuation was further averaged out by increasing the number of averages from the spectrometer.

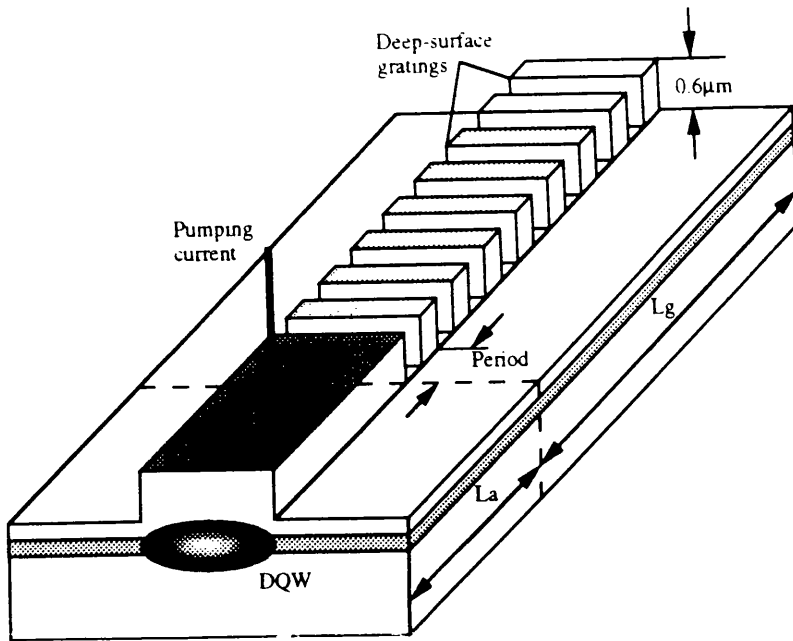


Fig.6-9 Schematic diagram of a DBR laser with surface gratings

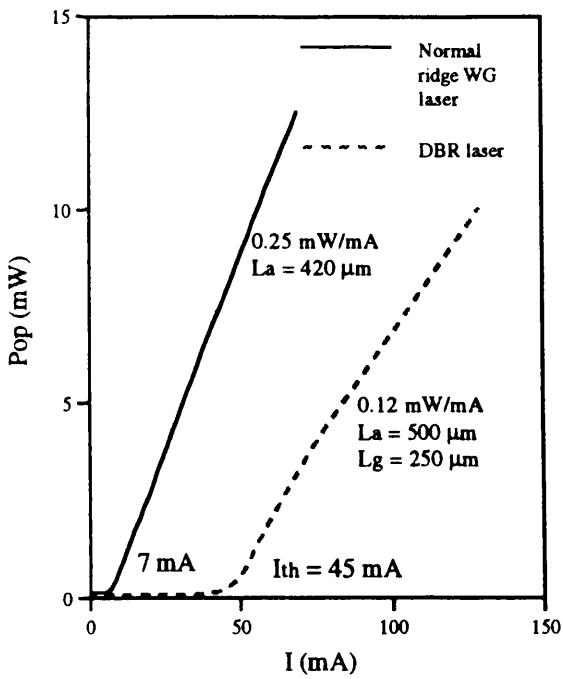


Fig.6-10 The L-I curves of a normal ridge waveguide laser and a DBR laser fabricated with the same material and processing.

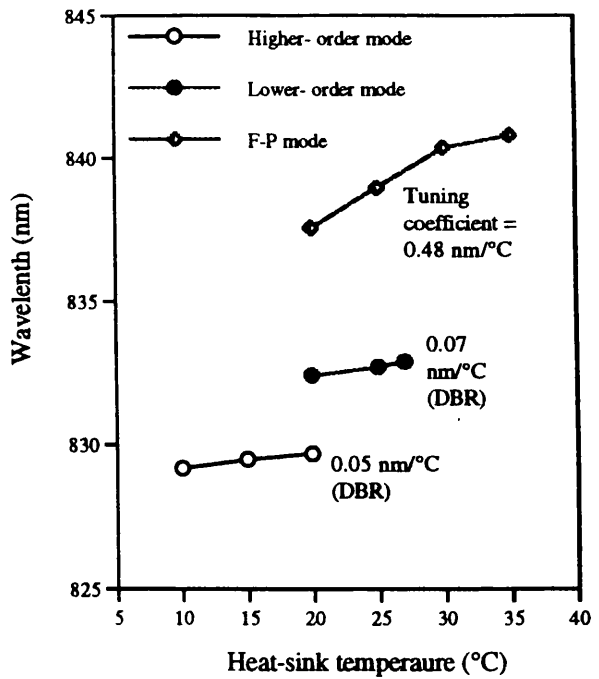


Fig.6-11 The temperature tuning characteristics of a DBR laser diode with  $L_a = 420 \mu\text{m}$  and  $L_g = 380 \mu\text{m}$

The DBR-mirror end of the laser was AR-coated with an  $\text{Al}_2\text{O}_3$  film 115 nm thick. Fig.6-10 shows the L-I curves of a DBR laser and of a normal laser made from the same material and with the same processing. For the normal ridge waveguide laser with  $L_a = 420 \mu\text{m}$ , the threshold current is 7 mA, compared to 45 mA for the DBR laser with  $L_a = 500 \mu\text{m}$  and  $L_g = 250 \mu\text{m}$ .

It should be noted that the normal laser with cavity length of 420  $\mu\text{m}$  lased at 840.6 nm, compared to 839.7 nm for the DBR laser with the geometry described as above. Both lasers were measured at the active end with drive current of  $1.05 I_{th}$  and at the heat-sink temperature of 25 °C.

From far-field measurements (not shown here), the single-lobe field patterns ensured that the single lateral-mode operation was maintained for the injection current of  $3 I_{th}$  or higher.

## 2. Temperature tuning coefficient

Fig.6-11 shows the temperature tuning coefficient of a DBR diode. The drive current was fixed at  $1.2 I_{th}$  with a 400-ns pulse width and a repetition rate of 1 KHz. The heat-sink temperature was controlled by a Peltier-effect cooler. It is known that the F-P lasing mode follows the temperature dependence of the bandgap, while the DFB lasing mode follows the smaller temperature dependence of the refractive index [10]. It was evident (Fig.6-11) that the DBR mode had a smaller temperature tuning coefficient of 0.07 nm/°C at 25°C, compared to 0.48 nm/°C for the Fabry-Perot (F-P) mode. In this case, the tuning coefficient of the F-P modes was measured on the same structure, but before AR coating of the DBR-mirror end.

## 3 Lasing characteristics

The lasing spectra of the DBR lasers, with  $L_a = 500 \mu\text{m}$  and  $L_g = 250 \mu\text{m}$ , are shown in Fig.6-12, in which the current levels range from 0.95 to  $3 I_{th}$  with a 5- $\mu\text{s}$  pulse width and a repetition rate of 3 KHz.

In addition, the side-mode suppression ratio (SMSR) is 31 dB for the laser with  $L_a = 420 \mu\text{m}$  and  $L_g = 380 \mu\text{m}$  and the range of maintaining the single longitudinal-mode operation can be up to  $3.1 I_{th}$  ( i.e. 150 mA).

## 4 Coupling coefficient and Bragg reflectivity

### A. Coupling coefficient

Fig.6-13 (a) shows the gain spectrum below threshold at 25 °C, from which it can be easily seen that the Bragg reflection was pronounced in the centre of the Bragg band and the mode spacing is smaller in the region well outside the Bragg band, since the gratings have no effect. So the finely spaced F-P mode structure resulting from the

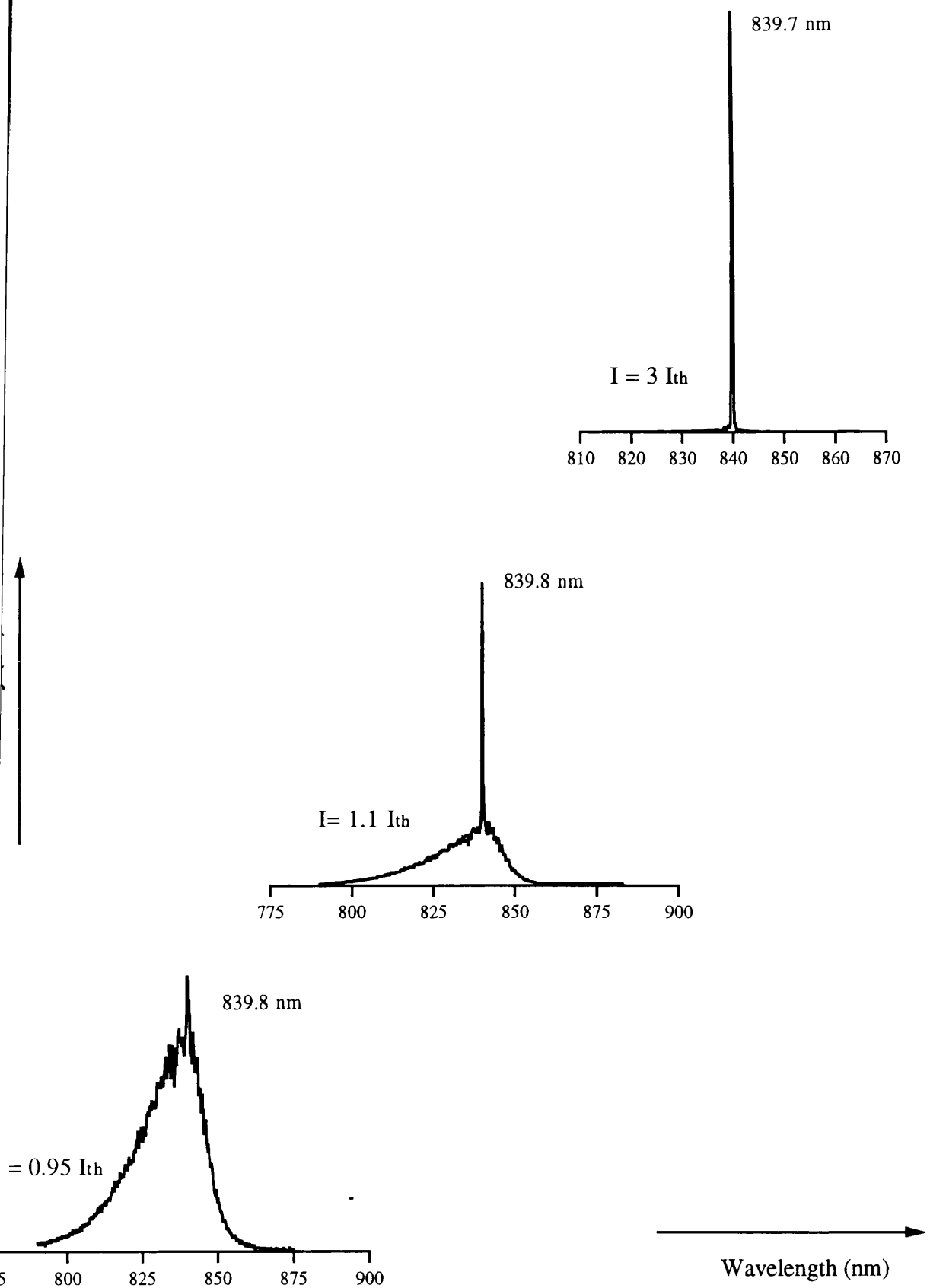
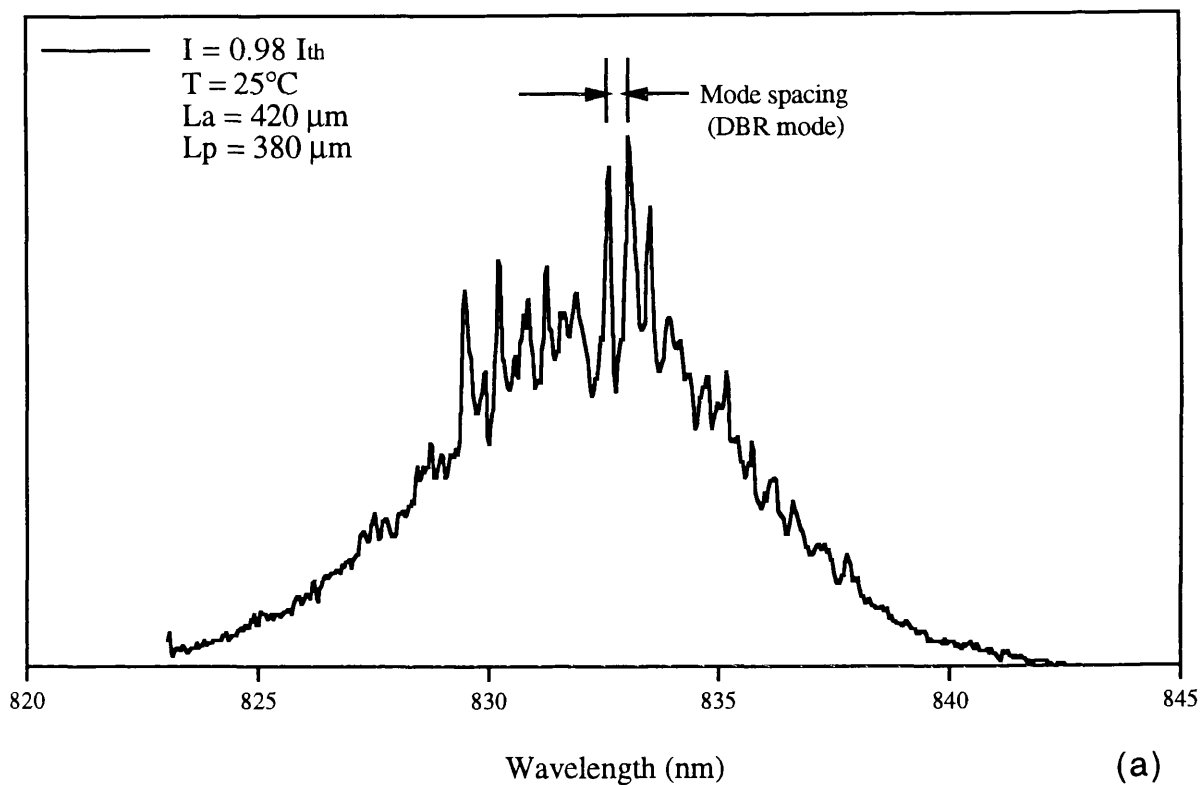
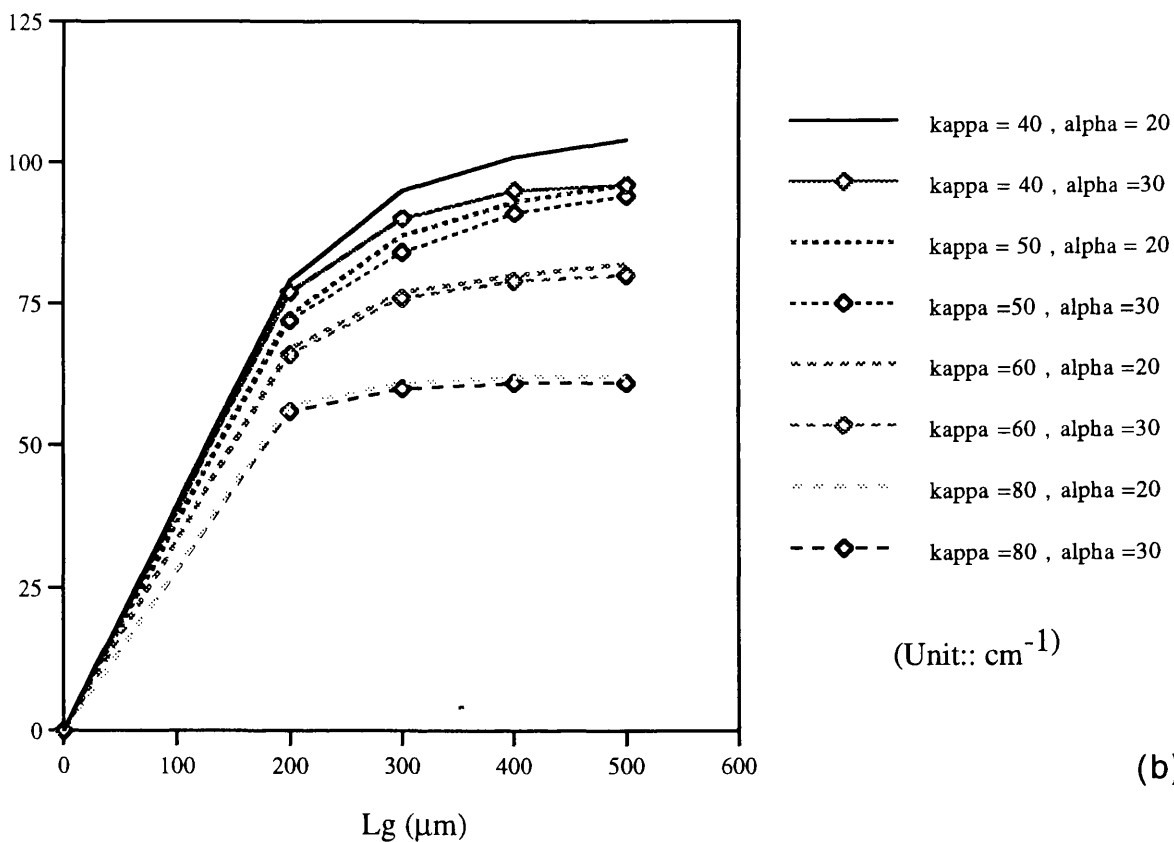


Fig.6-12 The lasing spectra of the DBR laser at different current levels (25 °C)

Intensity (a.u.)



(a)



(b)

Fig.6-13 (a) The spontaneous emission spectrum of a DBR laser for measuring the mode spacing near the Bragg peak.  
 (b) The dependence of the effective grating length on the actual grating length with coupling coefficient ( $\kappa$ ) and the grating loss ( $\alpha$ ) as parameters.

entire cavity length between two crystal facets can be observed.

The DBR mode spacing can be rewritten, as Eq.(3-18), at the Bragg peak according to Eq. (6-4):

$$\Delta\lambda_m = \frac{\lambda^2}{2n_{ge}L_t} \quad (6-4)$$

where  $L_t = L_a + L_{eff}$ .  $L_a$  is the active section length,  $L_{eff}$  is the effective grating length, and  $n_{ge}$  is the effective refractive index of the gratings, which can be obtained under the phase-matching condition, i.e.  $\Lambda = [3\lambda / 2n_{ge}]$ . At the heat-sink temperature of 25°C, the mode spacing at the Bragg peak is 0.21 nm for the laser with  $L_a = 420 \mu\text{m}$  and  $L_p = 380 \mu\text{m}$ .

The effective grating length  $L_{eff}$  can be expressed as [11]:

$$L_{eff} = \frac{1}{2} \frac{(\alpha_g/2)L_g \left\{ \left[ \frac{\tanh(qL_g)}{(qL_g) - 1 / \cosh^2(qL_g)} \right] + \tanh^2(qL_g) \right\}}{(\alpha_g/2) \tanh^2(qL_g) + q \tanh(qL_g)} \quad (6-5)$$

where  $q = [\kappa^2 + (\alpha_g/2)^2]^{1/2}$  at  $\lambda \cong \lambda_B$ . and  $\alpha_g$  represents the grating losses. When the grating period  $\Lambda = 389 \text{ nm}$  (see section 6-4), the mode-spacing observed (Fig.6.13(a)) was  $\Delta\lambda_m = 0.21 \text{ nm}$ , with  $L_g = 380 \mu\text{m}$ . The refractive index estimated from Eq. (6.4) was then  $n_{ge} = 3.212$  and the estimated loss of  $\alpha_g = 30 \text{ cm}^{-1}$  [see note], at a wavelength of  $\lambda = 833 \text{ nm}$ , gave an estimated value of  $L_{eff} \sim 95 \mu\text{m}$ . Referring to Fig.6-13(b), the estimated value of the coupling coefficient is  $\kappa \approx 45 - 50 \text{ cm}^{-1}$ .

(Note): The total grating losses include total absorption losses and the radiation coupling losses of the grating [12].

### B. Bragg reflectivity

Considering the effect from the grating losses, the Bragg amplitude reflectivity at zero detuning can be expressed by [11]

$$r_g = \frac{j \tanh(qL_g)}{(q/\kappa) + (1 + j/2)(\alpha_g/\kappa) \tanh(qL_g)} \quad (6-6)$$

The dependence of the *power* reflectivity,  $r_g^2$ , on the coupling strength  $\kappa L_g$  with  $(\alpha_g/\kappa)$  as parameters is shown in Fig.6-14, which was computed using Eq (6-6).

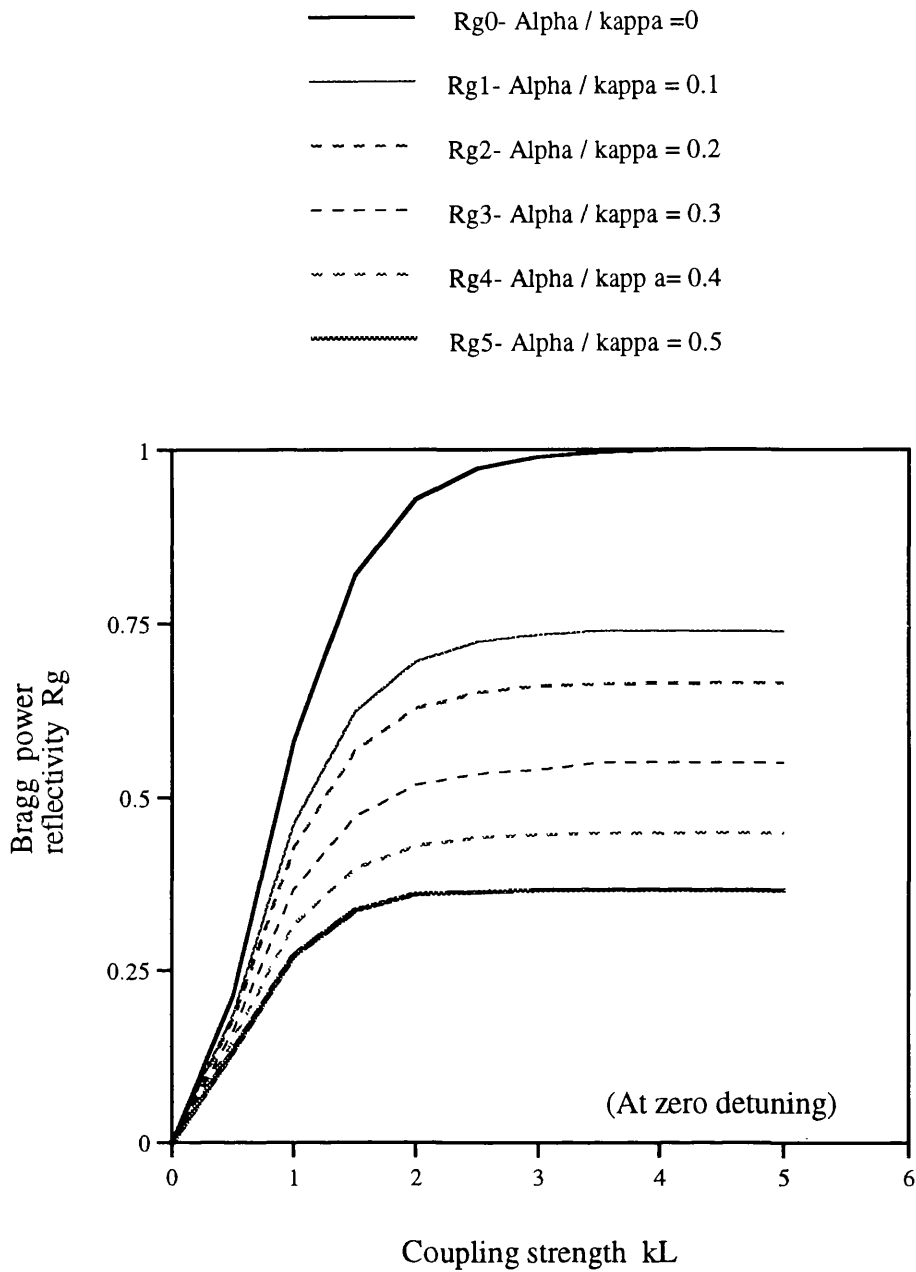


Fig.6-14 The calculated Bragg power reflectivity at zero detuning as a function of the coupling strength.

## 6-8 Discussion

### A. Side mode suppression ratio (SMSR)

In order to increase the mirror-loss difference between the main mode and side modes (i.e. to increase the mode discrimination), it is necessary to reduce the active section length [11,13]. On the other hand, the grating length should be sufficiently large to build up the mirror reflectivity at a specific selected wavelength .

If the DBR mode spacing is larger than the bandwidth of the net reflectivity and a sufficient mode discrimination is maintained [14], the single-mode operation with very high SMSR can be achieved. However, if the above bandwidth is too wide and can not meet the criterion, a further increase of the injection current is likely to support lasing in other longitudinal modes and limits the increase of the SMSR.

It should be noted that the net reflectivity bandwidth of the laser cavity is defined as the full width at half maximum (FWHM) of  $r_f r_g$ , where  $r_f$  and  $r_g$  are the crystal facet (i.e. active end) and the Bragg (field) reflectivities respectively [14].

### B. Power coupling factor

As defined in section 3-3, the effective Bragg power reflectivity  $R_g$  (eff) is :

$$R_g(\text{eff}) = C_o^2 R_g \quad \text{with } 0 < C_o < 1 \quad (6-7)$$

where  $C_o^2$  is the *power* coupling coefficient and the *field* coupling coefficient  $C_o$  is defined by [13]:

$$C_o \equiv \int_{-\infty}^{+\infty} E_a^{(o)}(x) \cdot E_p^{(o)}(x) dx$$

where  $E_a^{(o)}(x)$ ,  $E_p^{(o)}(x)$  are the lowest - order confined modes in the the active and the passive sections respectively.

It should be noted that the above overlap integral considers only the lowest-order confined mode coupling. In general, the following factors may cause  $C_o$  to be less than unity:

(1) Since the modal refractive indice in the active and grating sections are different, the modal distributions will be somewhat different as well. The coupling factor integrated from the above orthonormality should be less than unity [15].

(2) The guided-radiation mode coupling is large:

The condition for third-order Bragg scattering is given as follows [16]:

$$\sin \theta = \frac{2}{3} N - 1 \quad \text{with } N = 1, 2 \quad (6-8)$$

where  $\theta$  is the angle between the wavefront and the plane of PN junction. At these specific angles, the scattered waves will be in phase and satisfy the Bragg scattering condition.

- (3) The high-scattering nature of deep air surface gratings.
- (4) The reflections due to nonuniformity of the grating-etch profile.

### C. Bragg reflectivity

The following factors can affect the Bragg reflectivity :

#### (1) Grating losses

In addition to the propagation losses, the radiation coupling loss of the gratings [11] is also a crucial part contributed to the surface grating losses.

The effect of the grating losses on the reflectivity was shown in Fig 6-14.

#### (2) Wavelength detuning

When the operating wavelength is detuned from the Bragg wavelength, the power reflectivity would be lowered compared to that at zero detuning as discussed in section 3-3.

#### (3) Coupling strength $\kappa L_g$

Higher value of coupling strength  $\kappa L_g$  gives stronger Bragg reflection, and vice versa.

#### (4) Power coupling factor ( $C_0^2$ )

Smaller value of  $C_0^2$  means less effective coupling of the propagating power between the active and the grating sections, which in turn implies smaller value of the effective reflectivity.

It should be stressed that, from Fig.6-14, the Bragg reflectivity depends strongly on the ratio of the grating losses  $\alpha_g$  to the coupling coefficient  $\kappa$ .

## 6-9 Summary

Grating fabrication is a sophisticated task, especially when it performed on a semiconductor wafer. By using the two-beam interference method, the system should first be precisely aligned. A redundant exposure test is generally required for a successful pattern recording. Accurate control of the grating etch step, mark / space ratio, and the etch profile is extremely important. The gratings would have high performance if the final cleaning process was properly undertaken.

An asymmetric DQW structure B564, grown by Glasgow MBE group, was used to fabricate the DBR lasers with surface gratings of 0.6  $\mu\text{m}$  deep. For the lasers with estimated coupling strength  $\kappa L_g$  of 1.3, the lasing wavelength is 839.7 nm, the slope efficiency is 0.12 mW/mA and the threshold current was 45 mA at 25 °C

measured at the active (crystal facet) end. The temperature tuning coefficient is 0.07 nm/°C for the DBR mode, compared to 0.48 nm/°C for the F-P mode.

From the calculated and measured results, the Bragg reflectivity and the coupling coefficient have been estimated. The elements affecting the power coupling factor, which, in turn, influence the effective Bragg reflectivity were described. It is believed that the deep surface-gratings may experience significant radiation coupling losses. Accurate values of the coupling coefficient and the Bragg reflectivity can only be obtained from accurate measurements of all grating losses.

## 6-10 References

- [1] H. Nishihara, M. Haruna and T. Suhara, '*Optical Integrated Circuits*', p.209 McGraw-Hill Book Comp., New York, 1989.
- [2] M. Born and E. Wolf, '*Principles of Optics*', sixth edition, section 7.2, Pergamon Press, Maxwell House, New York, 1989.
- [3] R.G. Hunsperger, '*Integrated Optics: Theory and Technology*', 3rd edition, Springer-Verlag, Berlin, 1991.
- [4] W. Streifer, D. R. Scifres, and R.D. Burnham, 'Coupling coefficients for distributed feedback single- and double-heterostructure diode lasers', pp.867-873, V.11, No.11, IEEE J. Quantum Electron., 1975.
- [5] M. Born and E. Wolf, '*Principles of Optics*', sixth edition, section 8-6, Pergamon Press, Maxwell House, New York, 1989.
- [6] F. Vasey, J.M. Stauffer, Y. Oppliger and F.K. Reinhart, 'Characterization of an AlGaAs Rib Waveguide Using a Grating in a Fabry-Perot Etalon Configuration', V-30, No.27, pp.3897-3906, Applied Optics, 1991.
- [7] W.H. Tsai, 'Mode-matching method in optical corrugated waveguides with large rectangular groove depth', PhD Thesis, Glasgow University, 1995.
- [8] S. Adachi, 'Model dielectric constants of GaP, GaAs, InP, InAs, and InSb', R1-R29, V.35, No.14, Physical Review B, 1987.
- [9] D. Hofstetter, H.P. Zappe, J.E. Epler and J. Sochtig, 'Single-growth-step GaAs/AlGaAs distributed Bragg reflector lasers with holographically-defined recessed gratings', V.30, No.22, pp.1858-1859, Electron. Lett., 1994
- [10] H.C. Casey, Jr. and M.B. Panish, '*Heterostructure lasers*', p.266, Part B, Academic Press, New York, 1978.
- [11] W.T. Tsang, 'Dynamic Single-mode semiconductor lasers with a distributed reflector', '*Semiconductors and Semimetals*', Chapter 4, V.22, part B, Academic Press, New York, 1985.
- [12] W. Streifer, D. R. Scifres, and R.D. Burnham, 'Analysis of grating-coupled radiation in GaAs/ GaAlAs lasers and waveguides', pp.422-428, V.12,

No.7, IEEE J.Quantum Electron., 1976.

[13] T.P.Lee, C.A.Burrus, J.A.Copeland, A.G.Dentai, and D.Marcuse, 'Short-cavity InGaAsP injection lasers: Dependence of mode spectra and single-longitudinal-mode power on cavity length', pp.1101-1113, V.18, NO.7, IEEE J. Quantum Electron., 1982.

[14] H.M.Stoll, 'Optimally coupled, GaAs-distributed Bragg Reflection Lasers', pp.1065-1072, V-26, No.12, IEEE Transac. on Circuits and Systems, 1979.

[15] M.Koshiba, K.Ooishi, T.Miki, and M.Suzuki, 'Finite-element analysis of the discontinuities in a dielectric slab waveguide bounded by parallel plates', pp.33-34, V.18, No.1, Electron. Lett., 1982.

[16] R.H.Hunsperger, '*Integrated Optics: Theory and Technology*', 3 edi., Section 13-1, Springer-Verlag, Berlin, 1984.

## **Chapter 7 Conclusions and future work**

### **7-1 Summary of the thesis**

Before describing the device fabrication and characterisation, essential optical and electrical properties of the laser diodes were reviewed in chapter 2. To facilitate the observation on the wave guiding in the laser devices, simulations were done well in advance of the device fabrication.

A detailed derivation of the model for calculation of the waveguide losses of a QW diode was carried out in chapter 3. It was found that this model provided a good approximate estimate of the waveguide losses by the experimental data, if the lasing peak wavelength shift, due to the gain-loss competition in the composite structure, is much smaller than the full-width at half maximum of the laser gain spectrum. On the other hand, a systematic investigation on DBR laser diodes was carried out in the latter sections of chapter 3.

By using a qualitative model, the effect of native oxide on the QW intermixing process was described, and an effective way to obtain a controllable PL shift for the QW disordering was suggested. Detailed studies on the IFVD disordering technique were depicted in chapter 4. This QW intermixing technique was then implemented to fabricate gain-guided and index-guided extended-cavity lasers. Very low propagation losses in the passive section and small lasing wavelength shifts were found in index-guided extended-cavity lasers. IFVD process could effectively reduce the propagation losses in the passive section of an oxide stripe laser as well, but the lasing wavelength shift, due to gain-loss competition, is highly current-sensitive.

Detailed procedures of fabricating third-order gratings for DBR lasers were demonstrated in chapter 6. The technique was then implemented to fabricate the DBR lasers. Results from the fabrication and the calculation were used for analyzing the laser performance.

### **7-2 Conclusions**

One object of this thesis is to describe the technology for fabricating high performance extended-cavity lasers and to use an appropriate model for device characterisation. It was found that waveguide simulation is always beneficial for device fabrication and analysis. In this work, calculations of the field contours, modal analysis, and estimates of the effective refractive indices of the waveguide structures were all performed well before the device fabrication.

It is well known that extended-cavity laser diodes, with long passive waveguide

sections, exhibit narrow spectral linewidths. A convenient and effective QW disordering technique, IFVD, was adopted to reduce the propagation losses of the passive waveguide section and to decrease the lasing wavelength shift, due to the gain-loss competition in the composite structure, from that of the solitary laser.

It was found that many factors, such as the RTA process parameters, the preparation of the dielectric capping layers, and the presence of native oxide on GaAs surface, influenced the QW intermixing result. A special effort has been put to observe the native oxide effect on the QW disordering. A model was used to interpret its effect on the Al-Ga interdiffusion and a suggestion was given to eliminate the native oxide effect on the IFVD process.

It is known that plasma-assisted RIE processes induce etch damage. To reduce the ridge-sidewall scattering loss arising from this etch damage, a low-damage process, MCP RIE, was used. This RIE system provides a stable plasma by separating the extraction of the plasma for the etching purpose from the generation of the plasma. Under an optimum processing condition, it provided very smooth and vertical, sidewalls, and most importantly, reduced the etch damage to 3 nm, compared to 10 nm for a conventional RIE system.

By using the QW intermixing and the MCP RIE techniques, high performance ridge waveguide lasers with integrated passive sections were successfully fabricated and characterized. These techniques not only effectively reduced the waveguide losses in the passive section, but also greatly decreased the lasing wavelength shift arising from the gain-loss competition in the composite structure. A qualitative model was set up and used to interpret the effect of gain-loss competition on the lasing wavelength shift for the extended-cavity devices.

Laterally coupled DFB lasers with deep surface gratings have been well developed in our optoelectronics group, but the DBR laser with deep surface gratings has been a new attempt for just a few years. Third-order surface gratings were successfully fabricated on the passive ridge waveguide sections for DBR lasers. By carefully controlling the coupling strength and properly choosing the active section length, a DBR laser with high mode selectivity can be achieved.

DBR lasers were analyzed using a model in which the effective cavity length was first determined from experimental data and related to computed results. The DBR lasers could then be treated as Fabry-Perot lasers with a frequency-dependent mirror reflectivity at the selected wavelength.

The effects of the grating losses on the coupling coefficient and the Bragg reflectivity were analyzed. From this analysis, important parameters, such as the threshold current, the lasing wavelength, and the slope efficiency could be predicted.

### **7-3 Future work**

For the QW intermixing on the extended-cavity device, how to produce the nearly stress-free dielectric capping layers will be crucial for the yield and the reproducibility of the laser fabrication. A more accurate model to fit the gain-current relation for the composite structure deserves to be worked out in order to obtain the passive waveguide loss of a composite cavity laser.

The influence of the QW intermixing on the Bragg reflectivity and the coupling coefficient will be beneficial to characterize a DBR laser. The depth of surface gratings for DBR lasers will be a key factor to be investigated to achieve an optimum condition for obtaining sufficient coupling strength of the Bragg reflector and the adequate mode discrimination for the high side-mode suppression ratio.

and maintaining good power coupling between the active and passive sections.

The effect of the coupling strength and the nonlinear gain distribution on the spectral characteristics is very important. Additionally, how to obtain the grating losses with a reasonable accuracy is a meaningful subject to be carried out for computing the Bragg reflectivity and the coupling coefficient of DBR lasers.

## Appendix

The following wafers were used in the laser fabrication for this work:

**Table.A Details of the symmetric DQW MBE material B423**

Layer	Thickness (nm)	Material / Al fraction	Concentration (cm <sup>-3</sup> )	Purpose of layers
Sub	-	GaAs	N <sup>++</sup> 5E18	Contact layer
0	500	GaAs	N <sup>+</sup> 2E18	Buffer
1	1500	AlGaAs / 0.40	N 5.5E17	Lower cladding
2	100	AlGaAs / 0.20	Undoped	QW barrier
3	10	GaAs	Undoped	QW
4	10	AlGaAs / 0.20	Undoped	QW barrier
5	10	GaAs	Undoped	QW
6	100	AlGaAs / 0.20	Undoped	QW barrier
7	700	AlGaAs / 0.40	P <sup>+</sup> 1E18	Upper cladding
8	100	GaAs	P <sup>++</sup> 5E18	Contact layer

(Note: The wafer B336 has the same structure as B423, except the 0.8 μm-thick upper cladding layer).

**Table B.The asymmetric DQW structure B564**

Layer	Thickness (nm)	Material / Al fraction	Concentration (cm <sup>-3</sup> )	Purpose of layers
Sub	-	GaAs	N <sup>++</sup> 5E18	Contact layer
0	500	GaAs	N <sup>+</sup> 2E18	Buffer
1	500	AlGaAs / 0.79	N 5.5E17	Lower cladding
2	142	AlGaAs / 0.20	Undoped	QW barrier
3	8	GaAs	Undoped	QW
4	8	AlGaAs	Undoped	QW barrier
5	8	GaAs	Undoped	QW
6	52	AlGaAs / 0.20	Undoped	QW barrier
7	700	AlGaAs / 0.40	P <sup>+</sup> 1E18	Upper cladding
8	100	GaAs	P <sup>++</sup> 5E18	Contact layer

(Note): Excitonic peak= 791 nm ( at 77° K)

**Table C. The structure details of DQW QT632**

Layer	Thickness (nm)	Material / Al fraction	Concentration (cm <sup>-3</sup> )	Purpose of layers
Sub	-	GaAs	N <sup>++</sup> 2.6E18	Contact layer
0	500	GaAs	N <sup>+</sup> 1 E18	Buffer
1	1500	AlGaAs / 0.40	N 7.7E17	Lower cladding
2	100	AlGaAs / 0.20	Undoped	Graded barrier
3	10	GaAs	Undoped	QW
4	10	AlGaAs / 0.20	Undoped	QW barrier
5	10	GaAs	Undoped	QW
6	100	AlGaAs / 0.20	Undoped	Graded barrier
7	1500	AlGaAs / 0.40	P <sup>+</sup> 5.4E17	Upper cladding
8	100	GaAs	P <sup>++</sup> 1.8E19	Contact layer